AE3200 Design Synthesis 2012-2013

eGyro

Final Report

DSE Group 10
www.egyro.nl

Bergers, R.P.H.G.	4096517
Dewitte, F.H.V.	4111729
Harinarain, V.N.	4052544
Höppener, D.C.	4042387
Kortenhof, B.L. van	4112830
Moerland, R.G.	4015185
Mooi, K.	4006704
Ostaijen, T.H.T. van	4077512
Ullrich, C.	4048946
Urlings, A.P.C.	4085345

May 27, 2013

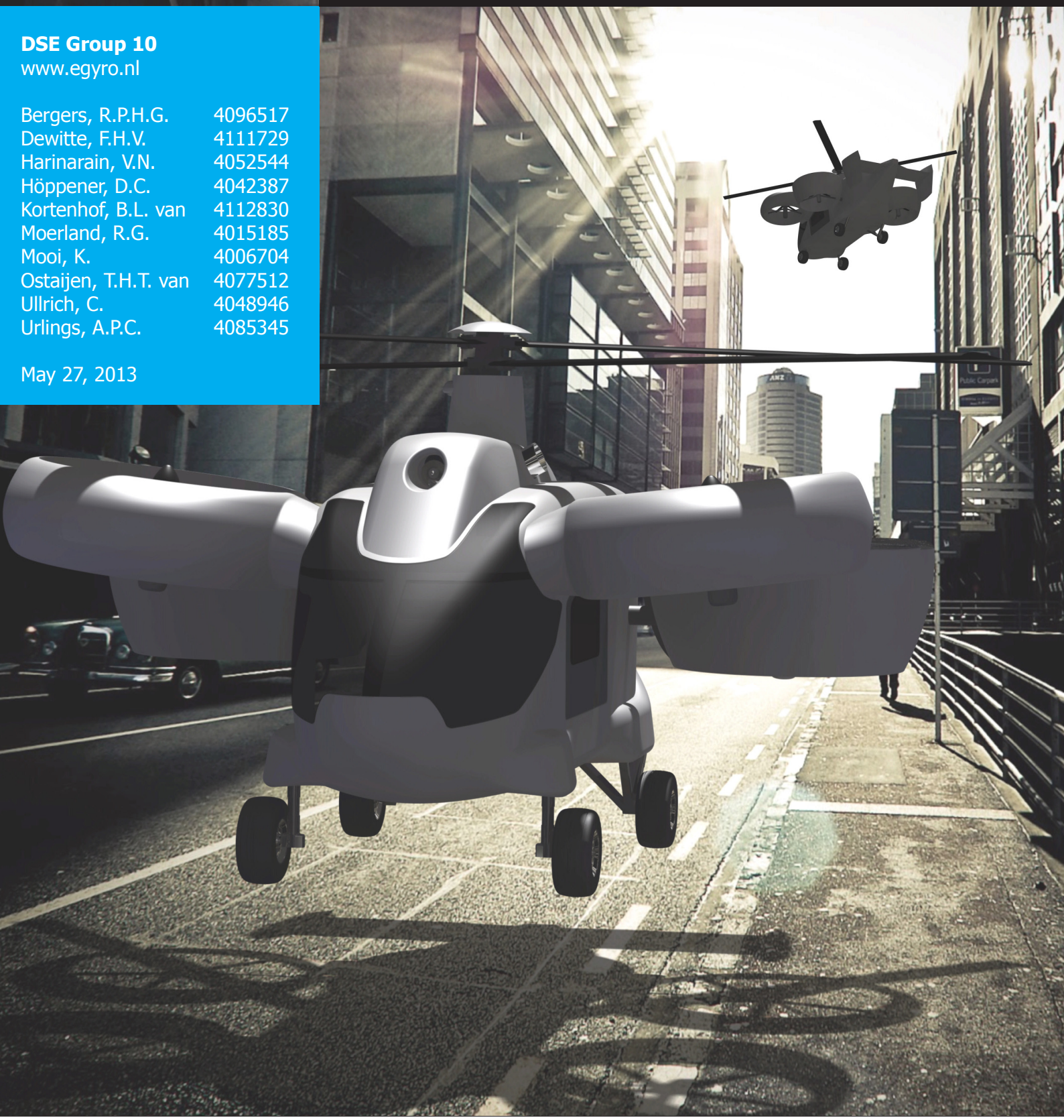

TU Delft Delft University of Technology

Challenge the future

Preface

This final report on the Emergency Medical Services (EMS) vehicle, called the eGyro, is written by ten students from the faculty of Aerospace Engineering at the TU Delft in 11 weeks time, according to the rules of the Design Synthesis Exercise (DSE) for third year students and serves as a final exercise to finish the Bachelor's Degree of Aerospace Engineering. During this design phase, the design team learned to work coherently in a group process and every group member contributed, according to his specialism, to the project. The purpose of writing this technical report is to describe the whole design process of the eGyro and shows which steps may need to be taken in order to finally produce the eGyro.

The exercise of the DSE has been performed in cooperation with the Red Cross and the Stichting Behoud Erfgoed De Vries-Robbé, as they are the major stakeholders of this project. During the design of the eGyro, assistance has been provided by supervisor Dr. M.D. Pavel and tutors ir. E. Gillebaart and H. Jara Orue MSc. Next to them, Prof. dr. ir. J.A.A.M. Stoop also provided a lot of information and tips for the marketing strategy, ir. H. Joore gave some new insights in gyro-plane flying and the EMS team in Rotterdam provided very useful information on modern EMS operations. The design team would like to thank everyone who has contributed to the project by supporting in any form.

All relevant sources that have been used are stated in the reference chapter in the back of this report. For the interested reader that wants to know more about a specific subject and the summary is not sufficient, please check the table of contents for the correct page of the subject that is of interest.

Source frontpage: http://ejosue-9.wix.com/honduras?_escaped_fragment_=__cctv

Summary

The DSE project about Future Air Transportation consists of a conceptual design for an environmentally friendly Vertical Take-off and Landing (VTOL) vehicle, capable of operating in highly populated areas. The goal is to design an EMS VTOL vehicle according to the following requirements: it should be able to transport three crewmembers, one patient and 225 [kg] medical equipment, it should have a cruise speed of 200 $\left[\frac{\text{km}}{\text{h}}\right]$, a range of 250 [km] and an endurance of 2 [h]. The maximum dimensions should be 6×6 [m] with a landing area of 12×12 [m] (for operation in the Netherlands). The designed vehicle, the so-called eGyro, is intended to replace current EMS vehicles. Currently, such vehicles are not designed primary to be environmentally friendly and are not able to operate in highly populated areas due to their dimensions. The eGyro is optimized to perform the following mission: take-off vertically from the base, fly to an emergency location within 30 minutes, land vertically at that location, transport a patient to a nearby hospital, return to the base and perform a new mission within 5 minutes.

The solution of DSE group 10, the eGyro, is a hybrid gyroplane with four ducted fans that can tilt, according to the mission profile, from a vertical to a horizontal position. Next to EMS operations, the vehicle can also be used as a personal air vehicle or for other purposes like law enforcement, military purposes or supply transport, providing a maximum payload of 485 [kg]. The eGyro VTOL operations are performed using four ducted fans with electric motors, powered by batteries to lower the noise and pollution during this initial phase of flight. The rate of climb for VTOL is 6.2 $\left[\frac{\text{m}}{\text{s}}\right]$. During cruise the vehicle operates like an auto-gyro with a cruise speed of 200 $\left[\frac{\text{km}}{\text{h}}\right]$. The maximum speed is 227 $\left[\frac{\text{km}}{\text{h}}\right]$. The aft ducted fans are tilted 90 [deg] to produce the thrust necessary for cruise. The front two ducted fans are turned off while cruising. During cruise, the power required for the electric motors is provided by a generator that is powered by an Arriel 2C2 turboshaft engine. The battery pack can be recharged at the same time. The vehicle structure consists mainly of Carbon-Fiber Reinforced Plastic (CFRP), which is expected to be used more often and more for aerospace applications in the future and which assures a relatively low Maximum Take-off Weight (MTOW) of 1850 [kg]. The eGyro has a small landing area of 12×12 [m] and is capable of driving on roads with a slope of 10 % with a maximum velocity of 30 $\left[\frac{\text{km}}{\text{h}}\right]$. Compared to the Eurocopter EC135 [1], the current EMS vehicle used in the Netherlands, the eGyro produces 2.5 times less noise and operates on less than $\frac{1}{4}$ of the landing area. The production cost of the eGyro is approximately € 676,000.

Currently the conceptual design of the eGyro is finished. The project started with a total of nine concepts, narrowed down to only three, and finally the eGyro concept is taken into the conceptual design phase. The next step of the design would be an extensive and even more detailed analysis of all subsystems of the eGyro. This would include extensive wind tunnel tests, Finite Element (FE) structural analyses and Computational Fluid Dynamics (CFD) computations on the vehicle. Also a more detailed control and stability analysis should be done, as currently only the cruise flight is analyzed. Including prototype tests and certification, the aim is to have the eGyro operational in 2024.

Table of Contents

List of Symbols

A	Area [m^2]
a	Speed of sound $\left[\frac{m}{s}\right]$
A_0	Inlet area [m]
A_2	Fan swept area [m^2]
A_4	Exit area [m^2]
A_a	Annulus area [m^2]
A_b	Blade plan form area [m^2]
$A_{element}$	Cross-sectional area of an element [m^2]
$A_{enclosed}$	Enclosed area of the rotor box cross-section [m^2]
$A_{frontal}$	Vehicle frontal area [m^2]
a_{hor}	Horizontal acceleration $\left[\frac{m}{s^2}\right]$
a_{radial}	Radial acceleration $\left[\frac{m}{s^2}\right]$
a_t	acceleration $\left[\frac{m}{s^2}\right]$
AR	Aspect ratio [-]
C	Costs []
c	Chord [m]
c_{box}	Chord of the rotor box [m]
C_d	Drag coefficient [-]
C_H	Horizontal blade force coefficient [-]
C_l	Lift coefficient [-]
C_m	Moment coefficient [-]
C_T	Thrust coefficient [-]
D	Total drag force on the vehicle [N]
d_{cg}	Distance to the center of gravity [m]
$d_{element}$	Moment arm element [m]
$D_{fuselage}$	Drag of the fuselage [N]
D_i	Induced drag [N]
D_p	Parasite drag [N]
$D_{profile}$	Profile drag [N]
D_{rotor}	Rotor drag force [N]
D_S	Shaft diameter [m]
DL	Disk loading $\left[\frac{kg}{m^2}\right]$
DoD	Depth of Discharge [-]
DR	Drag Ratio [-]
E	Endurance [h]
E_{bat}	Energy stored in batteries [J]
E_{mod}	Elasticity Modulus [Pa]
E_{req}	Required energy [J]
EPNL	Effective Perceived Noise Level [dB]
F	Force [N]
f	Frequency [Hz]
F_{air}	Vehicle drag force [N]
$F_{centrifugal}$	Centrifugal force [N]
$F_{element}$	Element total force [N]
f_f	Fundamental frequency [Hz]
f_{fine}	Fineness ratio [-]
F_{roll}	Roll resistance force [N]
$\sum F_x$	Sum of forces in x-direction [N]
$\sum F_z$	Sum of forces in z-direction [N]
g_0	Gravitational acceleration at sea level $\left[\frac{m}{s^2}\right]$
h	Altitude [m]
h_{box}	Height of the rotor box [m]
h_{fan}	Ducted fan duct height [m]
H_{force}	Horizontal blade force [N]
h_{motor}	Ducted fan motor height [m]
$\frac{\text{Hub gap}}{\text{Pylon width}}$	Hub gap to pylon width ratio [-]
i_d	Disk incidence angle [deg]
I_{rotor}	Rotor moment of inertia [$kg \cdot m^2$]
I_{xx}	Moment of inertia around x-axis [m^4]
I_{yy}	Moment of inertia around y-axis [m^4]
K	Swirl parameter $\left[\frac{m^2}{s}\right]$
KE	Kinetic energy [J]
L	Lift force [N]
L_b	Length of a beam [m]
$L_{element}$	Length of each element [m]
$L_{fuselage}$	Fuselage length [m]
L/D	Lift over drag ratio [-]
M	Mach number [-]
m	Mass [kg]
$M_{bending}$	Bending moment [Nm]
$\sum M_{cg}$	Sum of Moments around the cg [Nm]
$\dot{m}$	Mass flow $\left[\frac{kg}{s}\right]$
M_E	Effective rotational Mach number [-]
$M_{element}$	Element moment [Nm]
M_F	Flight Mach number [-]
M_{fan}	Moment due to the aft ducted fan [Nm]
M_{pitch}	Pitching moment [Nm]
MTOW	Maximum Take-off Weight [kg]
N	Noy value [-]
n	Engine revolutions [rpm],[min^{-1}]
n_{blades}	Number of blades [-]
$n_{element}$	Element number [-]
n_{fans}	Number of thrust providing ducted fans during cruise [-]
n_{rpm}	Number of revolutions per minute of the ducted fan [rpm],[min^{-1}]
$n_{sections,blade}$	Number of subsections on each blade [-]
p	Local pressure [Pa]
p_0	Static pressure at sea level [Pa]
p_2	Static pressure of the air going into the fan [Pa]

p_3	Pressure downstream of the fan [Pa]
P_a	Power available [W]
$P_\mathrm{acceleration}$	Power required for accelerating drive [W]
P_charge	Charging power [W]
P_climb	Required power to climb [kW]
P_crit	Critical force [N]
P_cruise	Cruise power [W]
P_drive	Power required for driving [W]
P_engine	Power delivered by the engine [W]
P_aft	Aft ducted fan available power [W]
P_front	Front ducted fan available power [W]
P_hill	Power required for uphill driving [W]
P_hover	Power required for hover [W]
P_i	Power due to induced drag on the rotor [W]
P_max	Maximum power [W]
P_p	Power required for pre-rotation [W]
P_par	Parasitic power [W]
P_pro	Profile power [W]
P_r	Power required [W]
P_range	Power required to reach a range [W]
P_swirl	Swirl power [W]
P_t	Thrust power [W]
P_total	Total power [W]
PNL	Perceived Noise Level [dB]
PWL	Overall sound power [dB]
$\dot{q}$	Pitch rate acceleration $\left[\frac{\mathrm{deg}}{\mathrm{s}^2}\right]$
q	Pitch angle [deg]
q_shear	Shear flow $\left[\frac{\mathrm{N}}{\mathrm{m}}\right]$
R	Specific gas constant $\left[\frac{\mathrm{J}}{\mathrm{kg \cdot K}}\right]$
r	Radius [m]
$r(i)$	Root radius of section i on a blade [m]
R_2	Ratio between fan radius and fan hub radius [-]
R_4	Ratio between exit radius and exit hub radius [-]
r_f	Tip radius of the fan [m]
r_h	Hub radius of the fan [m]
r_inlet	Ducted fan inlet area [m]
r_outlet	Ducted fan outlet area [m]
r_r	Rotor radius [m]
Re	Reynolds number [-]
RoC	Rate of Climb $\left[\frac{\mathrm{m}}{\mathrm{s}}\right]$
S	Wing area [m^2]
s	Interblade gap [m]
s_climb	Climb distance [m]
s_descend	Descend distance [m]
S_h	Horizontal tail surface area [m^2]
s_shock	Shock absorber deceleration distance [m]
SFC	Specific fuel consumption $\left[\frac{\mathrm{kg}}{\mathrm{W \cdot s}}\right]$
SPL	Sound Pressure Level [dB]
$\mathcal{T}$	Temperature [K]
T	Total thrust during cruise [N]
t	time [s]
$\mathcal{T}_0$	Temperature at sea level [K]
T_a	Thrust of the aft ducted fans [N]
t_acc	Acceleration time while driving [s]
t_charge	Charge time [s]
t_cruise	Cruise time [s]
t_{end}	Time length [s]
T_f	Thrust of the front ducted fan [N]
T_max	Maximum thrust [N]
t_mission	Mission time [s]
T_q	Torque [Nm]
$T_\mathrm{q,engine}$	Engine torque [Nm]
T_rotor	Rotor thrust [N]
t_skin	Skin thickness of the rotor box [m]
T_static	Static thrust [N]
t_step	Time of an interval [s]
T_vertical	Vertical thrust [N]
TOW	Take-off Weight [kg]
$\dot{u}$	Acceleration parallel to vehicle frame $\left[\frac{\mathrm{m}}{\mathrm{s}^2}\right]$
u	Velocity parallel to vehicle frame $\left[\frac{\mathrm{m}}{\mathrm{s}}\right]$
U_p	Perpendicular inflow velocity $\left[\frac{\mathrm{m}}{\mathrm{s}}\right]$
U_t	Tangential inflow velocity $\left[\frac{\mathrm{m}}{\mathrm{s}}\right]$
V	Speed $\left[\frac{\mathrm{m}}{\mathrm{s}}\right]$
$v(i)$	Total velocity in blade section i $\left[\frac{\mathrm{m}}{\mathrm{s}}\right]$
v_0	Cruise speed $\left[\frac{\mathrm{m}}{\mathrm{s}}\right]$
v_2	Fan flow speed $\left[\frac{\mathrm{m}}{\mathrm{s}}\right]$
v_4	Flow exit speed $\left[\frac{\mathrm{m}}{\mathrm{s}}\right]$
v_climb	Climb speed $\left[\frac{\mathrm{m}}{\mathrm{s}}\right]$
V_hor	Horizontal Speed $\left[\frac{\mathrm{m}}{\mathrm{s}}\right]$
v_i	Velocity at interval i $\left[\frac{\mathrm{m}}{\mathrm{s}}\right]$
v_ind	Induced velocity $\left[\frac{\mathrm{m}}{\mathrm{s}}\right]$
v_inf	Free stream velocity $\left[\frac{\mathrm{m}}{\mathrm{s}}\right]$
v_r	Radial velocity of the rotor tip $\left[\frac{\mathrm{m}}{\mathrm{s}}\right]$
V_res	Resultant rotor velocity $\left[\frac{\mathrm{m}}{\mathrm{s}}\right]$
v_t	Tangential velocity of the fan tip $\left[\frac{\mathrm{m}}{\mathrm{s}}\right]$
$v_\mathrm{t}(i)$	Velocity tangential to the fan in blade section i $\left[\frac{\mathrm{m}}{\mathrm{s}}\right]$
v_tip	Net velocity of the fan tip $\left[\frac{\mathrm{m}}{\mathrm{s}}\right]$
$\dot{w}$	Acceleration perpendicular to vehicle frame $\left[\frac{\mathrm{m}}{\mathrm{s}^2}\right]$
w	Velocity perpendicular to vehicle frame $\left[\frac{\mathrm{m}}{\mathrm{s}}\right]$
W_crew	Crew weight [kg]
W_F	Fuel weight [kg]
w_fuselage	Width of the fuselage [m]
W_PL	Payload weight [kg]
W_PL	Payload mass [kg]
W_tank	Fuel tank weight [kg]
X	Axial force [N]
x_a	Horizontal location of aft ducted fan [m]
x_cg	Horizontal location of center of gravity [m]
x_f	Horizontal location of front ducted fan [m]

x_r	Horizontal location of the rotor [m]
τ	Shear stress [Pa]
Y	Tangential force [N]
y	Distance from boom to centroid [m]
y_cg	Vertical location of center of gravity [m]
Y_Mises	Von Mises total stress [Pa]
y_r	Vertical location of the rotor [m]
α	Angle of attack [deg]
α_b	Blade angle [deg]
α_c	Control angle of attack [deg]
α_d	Rotor disk angle [deg]
α_f	Fuselage angle of attack [deg]
α_flapping	Flapping angle [deg]
α_r	Clearance angle of the rotor [deg]
α_rotor	Angular acceleration of the rotor [s^{-2}]
α_trim	Trim angle [deg]
β_r	Thrust angle of the rotor [deg]
γ	Flight path angle [deg]
$\delta_\mathrm{r}(i)$	Radial thickness of the annulus or average radius in section i [m]
$\eta(i)$	Swirl coefficient at blade section i [-]
η_average	Average swirl coefficient [-]
η_hover	Hover efficiency [-]
$\eta_{\dot{m}}$	Mass flow efficiency [-]
θ	Angle between rotor plane and line that connects to the ground point [deg]
θ^p	Angle between flight direction and line that connects to the ground point [deg]
θ_c	Control plane pitch angle (cyclic pitch) [deg]
$\dot{\theta}_\mathrm{f}$	Pitch rate of the vehicle $\left[\frac{\mathrm{deg}}{\mathrm{s}}\right]$
θ_f	Pitch angle of the vehicle [deg]
θ_p	Pitch angle [deg]
λ	Temperature gradient $\left[\frac{\mathrm{K}}{\mathrm{m}}\right]$
$\lambda(i)$	Flow coefficient of section i on a blade [-]
μ	Friction coefficient [-]
μ_a	Advance ratio [-]
$\phi(i)$	Inflow angle of the airstream in blade section i [deg]
φ	Ducted fan tilt angle [deg]
ρ	Air density $\left[\frac{\mathrm{kg}}{\mathrm{m}^3}\right]$
σ	Solidity factor [-]
σ_yield	Material yield stress [Pa]
σ_z	Stress [Pa]
ω_r	Rotor rotational speed [rpm],[s^{-1}]

List of Abbreviations

AC	Alternating Current
BLDC	Brushless permanent magnet DC motor
CFD	Computational Fluid Dynamics
CFRP	Carbon-Fiber Reinforced Plastic
DC	Direct Current
DSE	Design Synthesis Exercise
EMS	Emergency Medical Services
EPNL	Effective Perceived Noise Level
FBD	Functional Breakdown Diagram
FFD	Functional Flow Diagram
MMT	Mobile Medical Team
MTOW	Maximum Take-off Weight
OEW	Operational Empty Weight
PNL	Perceived Noise Level
RAMS	Reliability, Availability, Maintainability and Security
RoC	Rate of Climb
SPL	Sound Pressure Level
SWOT	Strength, Weakness, Opportunities, Threats
VTO	Vertical Take-off
VTOL	Vertical Take-off and Landing

1 Introduction

In case of a medical emergency, it is desirable to have a fast medical emergency response system. To accommodate for this desire, an EMS system is currently in use. This system works by reporting the medical emergency, after which EMS vehicle(s) react to the report. Currently several vehicles are used in this system in the Netherlands, such as cars and emergency helicopters for Mobile Medical Team (MMT). However, there is need for a new vehicle which will improve the services provided by the current vehicles. This DSE is originated from this need. This vehicle will also be used in disaster stricken areas where it can be used to evacuate people in case of medical emergencies. This mission is conducted in combination with the Flying Hospital Project [2], which will be designed by a similar design group.

In order to come up with a solution for above problem, a Baseline Report [3] and a Mid-Term Report [4] already have been written. In the Baseline Report, an extensive literature study has been performed in order to come up with several concepts and engineering theories. During the Mid-Term Report, several concepts were already eliminated and one final concept has been selected for further investigation. This compound vehicle is using four ducted fans during this initial phase of flight. During cruise the vehicle operates like an auto-gyro with a cruise speed of 200 $\left[\frac{\text{km}}{\text{h}}\right]$. The aft ducted fans are tilted 90 [deg] to produce the cruise thrust. The front two ducted fans are turned off while cruising and do no rotate to have a clear field of view for the pilot. The vehicle will be called the eGyro. The eGyro serves as a solution to the original DSE problem and has outstanding performance characteristics compared to current EMS vehicles. The goal of this final concept report is to give an overview of the final conceptual design of the DSE assignment. The final concept design phase is used to elaborate extensively on the final concept in terms of aerodynamic, structural, landing gear, power train, stability and performance design.

In chapter two the requirements and market analysis are discussed, along with the expected development time of the eGyro. Chapter three describes the general lay-out of the vehicle, including the EMS specific lay-out. Next, chapter four explains the propulsion system in detail. Chapter five describes the aerodynamics of the rotor in detail. Chapter six handles the stability and controllability of the vehicle, including a tail size estimation and a motion analysis. The actual performance of the vehicle is discussed in chapter seven. Chapter eight describes all structural analyses that have been done on the vehicle, as well as the material selection for it. The cost and weight analysis of the vehicle is discussed in chapter nine. In chapter ten the final vehicle design is provided including renderings. Chapter eleven discusses several development characteristics, such as the Reliability, Availability, Maintainability and Security (RAMS) criteria and the risk analysis. Diagrams such as the hardware/software diagrams and the Functional Flow Diagram (FFD) diagrams are provided in chapter twelve. At last, chapter thirteen gives recommendations on the further development of the vehicle and chapter fourteen provides the conclusion of the project.

2 Requirements and Market Analysis

In this chapter, first the requirements derived in [3] will be presented and re-evaluated for this phase of the design. Next, the development time and several market possibilities for the eGyro will be discussed. Finally, a market analysis on the eGyro will be performed.

2.1 Requirements Analysis

The requirements obtained from [3] are stated below. However, during the design process some requirements have changed and are therefore stated in this section.

Since it is preferred to also penetrate other market segments than EMS, the passenger configuration is variable. For EMS, three crew members and one patient have to fit in the vehicle. For personal use, this changes to one pilot and at least three passengers, which may increase depending on the payload.

Requirement EMS-CONS-P7 below has become more strict since for VTOL it is aimed to use electric propulsion. This is in order to reduce noise and air pollution, which increases the amount of landing spots that can be used, since a lot of landing areas are restricted by noise pollution.

Next to this, the driving requirement was initially a secondary requirement, but it has become a primary technical requirement to be able to penetrate highly populated areas better than conventional vehicles.

Below, the primary and secondary constraints are given. Also, the primary and secondary technical requirements are stated. The design of the eGyro is based on these requirements and therefore these lists are very important for the design of the eGyro.

Primary Constraints

- EMS-CONS-P1: Speed

  The EMS vehicle shall have a cruise speed of at least 200 $\left[\frac{\text{km}}{\text{h}}\right]$.

- EMS-CONS-P2: Range

  The EMS vehicle shall have a range of at least 250 [km].

- EMS-CONS-P3: Cost

  The cost of the design shall be kept as low as possible.

- EMS-CONS-P4: Number of passengers

  The vehicle shall be able to transport three crew members and one patient. For other missions than EMS, one pilot and three passengers should be transported, which may increase depending on the payload.

- EMS-CONS-P5: Landing area

  The vehicle shall be able to land on a landing area of 12×12 [m].

- EMS-CONS-P6: Response time

  The response time of the vehicle shall not be more than 30 minutes to the outer boundaries of the operational area [5].

- EMS-CONS-P7: Sustainability

  It is tried to achieve low emission rates and use electric motors for VTOL.

- EMS-CONS-P8: Endurance

  The vehicle shall achieve an endurance of two hours.

- EMS-CONS-P9: Noise emission

  The vehicle shall not produce more than 80 [dB] at 300 [m] altitude.

- EMS-CONS-P10: Certification

  The vehicle shall comply to all FAA regulations concerning the vehicle.

- EMS-CONS-P11: Night operations

  The vehicle shall be able to operate at any time of day, also during night.

- EMS-CONS-P12: Wind speed

  The vehicle shall be able to fly at wind speeds up to 20.7 $\left[\frac{\mathrm{m}}{\mathrm{s}}\right]$ during daytime and at winds speeds up to 13.8 $\left[\frac{\mathrm{m}}{\mathrm{s}}\right]$ during nighttime, according to FAA CS-27 [6].

- EMS-CONS-P13: Fog, rain and snow

  The vehicle shall be able to operate at foggy, rainy or snowy conditions if the visibility is at least 100 [m] at daytime and 150 [m] at nighttime.

Secondary Constraints

- EMS-CONS-S1: MTOW

  The MTOW shall not exceed 3175 [kg].

- EMS-CONS-S2: Cabin area

  The cabin area shall be at least 1.5 $\times$ 2.5 [m].

- EMS-CONS-S3: Vehicle dimensions

  The vehicle dimensions shall be maximum 6 $\times$ 6 [m].

- EMS-CONS-S4: Turn-around time

  The vehicle shall have a turn-around time of 5 minutes.

- EMS-CONS-S5: Type of landing area

  The vehicle shall at least be able to land on asphalt, grass and sand.

- EMS-CONS-S6: Team

  The vehicle shall be designed by ten people

- EMS-CONS-S7: Time

  The vehicle shall be designed within 11 weeks.

Primary Technical Requirements

- EMS-TECH-P1: Maneuverability

  The vehicle shall be easily maneuverable in highly urbanized areas in order to optimize its performance during EMS operations.

- EMS-TECH-P2: Accessibility

  The vehicle shall be easily accessible, including access to on board systems.

- EMS-TECH-P3: Stability/control handling

  The vehicle shall be easily controllable for the pilot and shall be stable during operation.

- EMS-TECH-P4: Communication

  The vehicle shall be equipped with communication systems according to the FAA CS-27 book 1 part F [6] regulations and Dutch EMS (C2000).

- EMS-TECH-P5: Power

  The vehicle shall provide sufficient power for all on board equipment.

- EMS-TECH-P6: Drive

  The vehicle shall be able to drive for at least 1 [km] on all types of roads, from asphalt to dirt roads.

Secondary Technical Requirements

- EMS-TECH-S1: Hovering
  Within the FAA rules [6], the aircraft shall be able to hover.

2.2 Development Time

This section describes the necessary development time needed for the eGyro before entering the market. After the final conceptual design, the development of the eGyro will take several other steps before the production of the vehicle starts. Firstly, the desired component development time for the eGyro will be discussed in this chapter. Secondly, the desired production time will be elaborated in Section 2.2.2.

The desired development time, as stated by the design team, equals ten years after the final conceptual design. However, these ten years hold when the development is started directly after the final conceptual design. The most important components that need to be developed and take a lot of time are the batteries and the optimization of the aerodynamic frame. This is discussed further in Section 2.2.1. Note that the ten years are defined as a time frame for the production of the eGyro. Five years after the final conceptual design report, all desired techniques should be present for use in the eGyro.

2.2.1 Desired Component Development Time

In this section, the development time for certain eGyro components is stated. Note that these development times are estimates, since the technological development can not exactly be defined by the design team.

Batteries

The most critical component in terms of development time is the battery package of the eGyro. The final conceptual design of the batteries shown in Section 4.2.2 states that the batteries will need a specific energy of 0.5 $\left[\frac{\text{kWh}}{\text{kg}}\right]$. When looking at batteries that are currently on the market, the highest specific energy for lithium-ion batteries equals 0.4 $\left[\frac{\text{kWh}}{\text{kg}}\right]$, produced by Envia Systems [7]. However, when looking at the development of lithium-ion batteries over the last ten years, it is expected that within five years from now batteries will exist with a specific energy of 0.5 $\left[\frac{\text{kWh}}{\text{kg}}\right]$. When these batteries are available, the battery package for the eGyro can be developed and can be used for the production of it.

Generator

The chosen generator for the final conceptual design as shown in Section 4.2.3, has a specific energy of 0.1 $\left[\frac{\text{kg}}{\text{kW}}\right]$. Although this value that is currently only obtained experimentally [8], it is expected by the design team that the chosen generator will be produceable and usable within five years after the final conceptual design. Therefore, it is expected by the design team that the chosen generator has a representative specific energy value.

Aerodynamics Optimization

The optimization of the aerodynamic frame will need a lot of time and can not be completed during the final conceptual design. After the final conceptual design, windtunnel tests of the model are necessary in order to present a reliable aerodynamic analysis of the eGyro. Throughout these windtunnel tests, weak points in the aerodynamic performance of the vehicle will be determined. These weak points can be improved, but it will take a lot of time and some iterations before the final optimized configuration is found. Therefore, it is expected that the aerodynamic optimization will take about four years.

Material Weight Optimization

During the design of the eGyro, existing material properties are used. In order to optimize the vehicle weight, use can be made of new materials which are not present at the moment. Since new materials are constantly developed in aerospace engineering, there is a chance that within five years after the final conceptual design, new materials will be available for use in the eGyro. Use of these materials can lead

to a large weight reduction of the vehicle. For example, the weight of the inner frame, the landing gear, the rotor and the tail are sensitive to the material selection. Therefore, approximately five years after the final conceptual design, an analysis of the present materials needs to be performed in order to lower the weight of the eGyro as much as possible. However, if the weight of the eGyro would be reduced, the fuel calculations will have to be redone in order to optimize the vehicle.

Structural Optimization

Next to the material weight optimization, also the structure of the vehicle might be adapted in order to lower the weight of the eGyro. The main structural component that needs to be further developed and tested is the fuselage. The current fuselage design mainly consists of a tube-like structure with a skin next to this. The design team is convinced that this structural component can be improved, such that weight can be reduced. In order to optimize the structure of the eGyro, more detailed design methods are necessary like the finite element theory. It is estimated that the necessary time for structural optimization for the eGyro equals three years.

Transition Phase

At this moment, the transition phase of the vehicle is only theoretically explained by the design team. Therefore, in order to optimize the transition phase, it will need needs to be tested extensively. This testing in real life would require a model of the eGyro and will take some time in terms of programming the vehicle. It is estimated that the optimization of the transition phase, including the programming of the vehicle, would take about three years.

Air Traffic Regulations

In order to certify the vehicle, the eGyro should comply to present air traffic regulations. The testing of the eGyro and the checks for air traffic regulations will be a long process, as can be seen during the design of other civilian aircraft, this process will take approximately two years. However, most problems for the air traffic regulations are expected regarding the transition phase of the eGyro. No specific regulations are stated in the present regulations about the designed transition phase and therefore the air traffic regulations will need to be adapted in order to certify the eGyro.

2.2.2 Desired Production Time

In this section, the desired production time of the eGyro is described. The desired production time of the eGyro is estimated to equal five years. Within these five years, funds will have to be present, a production team will have to be present and a production facility is necessary. In the next subsections, the time estimates for each production part will be stated.

Recruiting Production Team

In order to build the eGyro, a properly selected production team will be necessary. The necessary time to recruit the right people is expected to be one year. This time frame seems to be a bit large, but when time elapses more people are necessary as the production process gets in a more advanced stage. Next to this, care should be taken regarding unexpected circumstances of production team members like illness and unwillingness of production team members. Therefore, the recruiting of the production team will be an on-going process, but a solid base for the team should be established after one year.

Production Facility

The production facility should be established approximately six years after the final conceptual design. This production facility should have enough machines and production facilities to produce the necessary parts and assemble the vehicle. However, certain components of the vehicle can be ordered from external market parties. For example, the tires, the motor and the batteries can be directly ordered. When looking at the PAL-V [9] production facility, the production facility does not need to be very large and extensive and most of the machines present are relatively simple.

Fund Raising

The most important factor to produce the eGyro will definitely be fund raising. Since the estimated production costs will be relatively high, sponsors for the project will have to be found. Note that fund raising starts directly after the final conceptual design, but that it is mostly important for the production process. Fund raising will therefore be an ongoing process and it is expected that the necessary funds will be present approximately eight years after the final conceptual design. The production time, however, will need another two years after the necessary funds are reached in order to produce the first eGyro for the market.

2.3 Market Possibilities

In this section the possibilities for the market of the design are discussed. Several market options are considered next to the EMS market: supply distribution, military, police and personal air travel. To make sure that the vehicle can perform the mission for these markets, small adaptations are discussed in the following sections. The first section explains the EMS configuration. The main adaptation that is made for other markets is the removal of the medical equipment and a reduction in necessary crew. Only one crew member still needs to be designed for: the pilot. This total reduction of around 485 [kg] in payload and crew weight can then be used for simple adaptations to the vehicle. If, however, a co-pilot is flying along with the pilot, the maximum payload is 400 [kg].

2.4 Base Lay-out

For the base lay-out, which can be seen in Figure 2.1(a), it is chosen to place two basic seats for the pilot and a possible co-pilot in the cockpit of the vehicle. The seats have a dimension of 0.45 $\times$ 0.4 [m] and are placed almost in the middle of the front doors, which have a length of 1 [m]. More in the back of the vehicle, rails of 2.5 [m] in length enable the mounting of several components for different market possibilities. The main cabin doors are placed directly behind the cockpit doors because of structural reasons. These doors are 1.3 [m] in width, which is 0.1 [m] wider compared to the main cabin door of the EC135 [1]. To increase the accessibility of the payload, doors are placed at the back of the eGyro with a width of 0.7 [m]. The spacious dimensions of the doors eventually result in an increase of the accessibility of the vehicle and an improved turn-around performance.

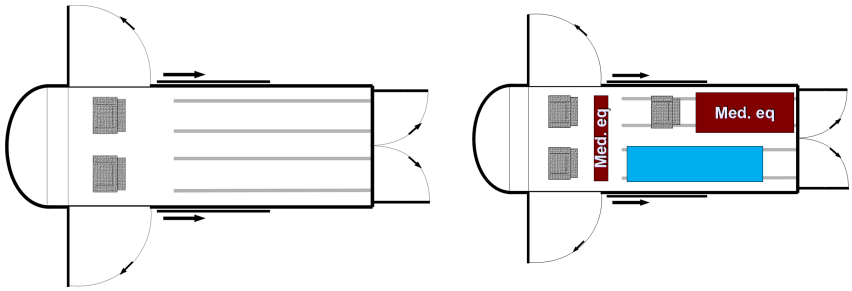

(a) Base cabin lay-out (b) EMS cabin lay-out

Figure 2.1: Cabin layouts

2.5 EMS Lay-out

The EMS configuration should provide enough space for a stretcher, medical equipment and working space for the doctors. The lay-out for the EMS configuration can be seen in Figure 2.1(b).

One basic seat is placed at the right side of the cabin, such that the doctor is facing to the front of the vehicle. However, the seats can turn to the back in order to take care of the patient. The seat has the same dimension as the cockpit seat and it has a footwell of 0.42 [m]. The seat can easily be accessed by the main cabin door. The stretcher that can be seen on the left of the picture is given a length of 1.9 [m]

and width of 0.5 [m] here. It can be loaded and unloaded through the main cabin door using a slide and turn mechanism and more easily through the backdoor by just sliding it outwards. In the back on the right of the eGyro there is space for the necessary medical equipment and potentially there is also some space available for medical equipment behind the cockpit. In total, 1 [m^2] is available for the storage of medical equipment.

2.5.1 Supply Transport

The first possibility next to EMS is that the vehicle could be used for supply transport. Supply transport is a large market as transport can be done in a lot of market sectors. The first possible sector is close to EMS services and is a possible cooperation possibility with the Flying Hospital DSE group [2]. This possibility is supply transport to disaster areas, which can either be food and water or other necessary equipment. It can also be used to transport military equipment from point A to point B, since it is more silent than the current helicopters used by the military. Another possibility is to use the vehicle for mail delivery purposes: for example deliver mail or other packages to remote areas which are not easily accessible using 'normal' transfer methods. Finally it can be used in construction and mining to transfer equipment from one place to another on the site. This can be done by either putting the equipment inside the cabin or by suspending it below the helicopter using cables. The latter option is not the preferred option since further adjustments would need to be made to attach the cables to the vehicle.

Some adaptations are necessary for the vehicle to be able to transport supplies. Since 485 [kg] is removed from the vehicle, the supplies that need to be carried can be up to 480 [kg] to make sure that the performance of the vehicle is not compromised. Another thing that is important for supply distribution is the volume that can be used for storage. Since the crew and the medical supplies are no longer necessary, the seat, stretcher and other equipment can now be removed from the cabin area. The cabin is now empty, which gives a storage volume of 5 [m^3]. In the general vehicle the seat and stretcher are already mounted on rails for easy removal. These rails can now be used to simply slide the supply container in the vehicle. A representation of this rail system can be seen in Figure 2.2(a).

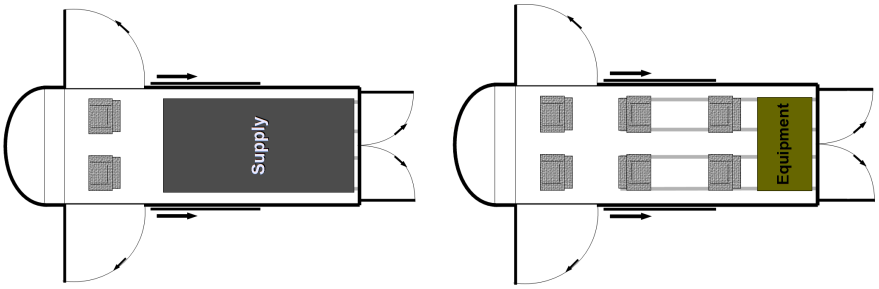

(a) Supply distribution configuration (b) Military configuration

Figure 2.2: Cabin layouts

2.5.2 Military

Another market possibility is military use. The military is looking for vehicles that have a VTOL capability and can be used for transportation of passengers or supplies. The recommended adaptations for supply transport can be found in the previous section. The eGyro has another advantage, because it is a silent vehicle compared to currently used VTOL vehicles. For military passenger transport a different adaptation of the vehicle would be necessary.

The 480 [kg] reduction in this case can be used for passengers and to install simple seats on the rails of the cabin. To make sure that the military personal with all the gear that needs to be carried can simply enter and exit the vehicle, the cabin lay-out is adapted. The adaptation is mainly done by rearranging the seats in such a way that someone can exit the vehicle as fast as possible. This configuration can be seen in Figure 2.2(b).

2.5.3 Police

The police uses airborne vehicles for the monitoring of areas of interest. This eye in the sky is useful to assist the ground team with locating problems or suspects. The eGyro could perform this mission without any adaptations. This is already used sometimes with for example news helicopters, when they are already in the area. However, when the helicopter is only used for this purpose, the cabin lay-out can be adapted for this mission. An option is to put one or two seats in the cabin to transfer passengers. An additional fuel tank can then be mounted in the back of the cabin to increase the endurance and range of the vehicle. This recommended configuration can be seen in Figure 2.3(a).

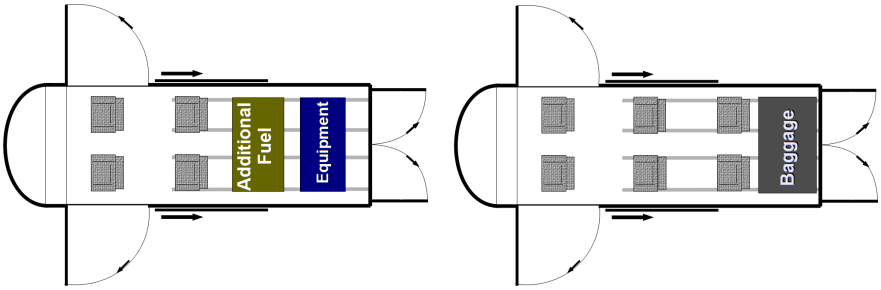

(a) Law enforcement configuration (b) Economy class configuration

Figure 2.3: Cabin layouts

2.5.4 Personal Air Travel

Another market possibility is personal air travel, where the main emphasis is on transporting small amount of passengers from one point to another. For personal air travel it is convenient to have a small, silent vehicle which has VTOL capabilities. The personal air travel market can be divided into two different categories: economy and business class. The main difference between the two is the amount of passengers that can be carried and the comfort of the vehicle.

Economy Class

To adapt the vehicle to an economy level of passenger transport, the lay-out of the cabin is changed. This change in lay-out can be seen in Figure 2.3(b). A total of four passengers can be transported, where all passengers look forward. This is due to the preference of people to look in the direction in which they are traveling.

Business Class

For the business level of transportation the cabin lay-out is different due to the size of the seats that are incorporated in the cabin. The seats that are in this configuration are different as well: they can be compared with the seats that are placed in the business class seats in air travel. The lay-out of the cabin can be found in Figure 2.4. One seat is placed in the front and oriented backwards. This is done to make sure that the passengers can easily communicate. A fourth passenger is unfortunately not an option without a more detailed change in the design. This is caused by the fact that the more comfortable seats have a higher weight compared to the regular seats.

2.6 Market Analysis

2.6.1 SWOT Analysis

In this section, a so called Strength, Weakness, Opportunities, Threats (SWOT) analysis is provided. From this analysis, the strategic approaches for the vehicle to penetrate the market can be determined.

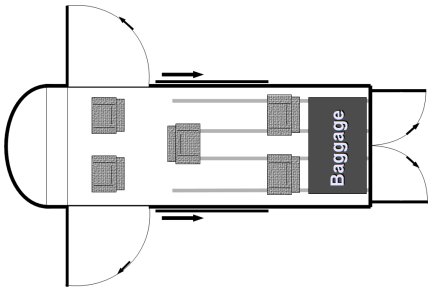

Figure 2.4: Business class configuration

Strengths

The strengths of the vehicle can be found in both the performance as well as the environmental impact. Starting with performance, the vehicle is able to land and take-off in a very dense area. This ability can not be achieved by any other competitive vehicle and is therefore a very strong asset of the designed vehicle. Next to this ability, the vehicle can perform a VTOL operation. This operation is very rare for helicopters, which are usually vehicles with a short take-off and landing operation.

Next to the performance qualities of the eGyro, the environmental impact of the vehicle is minimal. By using batteries to perform the VTOL operation, the emissions of the vehicle are reduced to a minimum. Next to that, the emissions of the Turbomeca engine are also very low, as will be shown in Section 7.6.

Weaknesses

It is very important that the weaknesses of the eGyro are not underestimated. These weaknesses have to be counteracted with valid arguments. First of all, considering the environment, it is not possible to cruise using the battery package. Therefore the vehicle is not capable of operating fully electrical. Next to this, another weakness of the vehicle is the relatively high development cost of the vehicle. However, this holds for every new vehicle that enters a market. When mass production of the vehicle starts, the total vehicle costs will drop quickly.

Opportunities

The opportunities for the eGyro are very large. The applications can range from law enforcement to a personal air vehicle. The initial vehicle is designed for EMS operations, but the payload can be varied in many options. The configuration of the vehicle can be changed continuously and several set-ups can be used.

Opportunities for market parties are present as well. Examples of involved market parties are:

- Damen Shipyards [10], which is investigating a floating helicopter platform. Designing a multi-purpose personal air vehicle would result in a big opportunity for Damen to expand their number of clients.
- Red Cross [11], which is one of the main customers for the eGyro. Initially, the eGyro is designed for emergency medical services and to provide first aid in disaster areas. The eGyro is designed to land in difficult to reach areas and is able to provide first aid at these areas.
- Government operations like law enforcement. The eGyro can for example operate as a police vehicle due to its wide utility opportunities by interchanging payload.

Threats

The biggest threat for the eGyro is the required money that has to be gathered from sponsors. The production cost of the vehicle is low, but the research costs, in turn, are much higher. In order to account for this, the network of market interested companies needs to be extended.

Next to this, for personal air travel, the speed of the eGyro might not be high enough. Investors who want to use the eGyro as a personal vehicle desire a quick vehicle as well. To counteract this argument, one can state that the eGyro has very good handling qualities and is able to land in very dense areas, whereas a helicopter is not able to.

3 eGyro Design Renderings

In this chapter the 3D renderings of the eGyro are presented as well as an explanation of the chosen lay-out and shapes. A good overview from the general vehicle lay-out can be seen in Figure 3.1.

3.1 General Lay-out

The lay-out represented in Figure 3.1 has a large front window such that the pilot has a good visibility. This is especially important to be able to land on small landing areas. Between the ducted fans at the side there is a sliding door for easy entrance. At the tail there is also a back door which makes it easy to carry the patient and medical equipment into the fuselage. The hole on top of the cockpit is the air inlet for the engine.

3.2 Ducted Fans

The horizontal location of the ducted fans determine the stability of the vehicle during VTOL operations. This is discussed in Chapter 6. However, the vertical location of the ducted fans is not depending on any stability or controllability. Therefore the vertical locations of the ducted fans are chosen in a way that is just most practical in use. To be able to access the cockpit, the front ducted fan should be located at the roof of the vehicle, such that the pilot can walk underneath it while entering the cockpit. The second advantage of locating them on the roof is that the pilots visibility during flight is not obstructed by the duct. Now the pilot can look around the vehicle and to the ground without any obstructions. The aft ducted fan is located halfway the fuselage height. Since the aft ducts have to be able to rotate, they can not be lowered further than halfway the fuselage, to assure sufficient ground clearance. Locating them at the roof, like the front two ducted fans, obstructs the rotor when the duct is tilted during cruise. Besides this, locating them at the roof also means that the aft ducted fans are placed in the wake of the front ducted fans during cruise. This is of course not desirable. Combining these reasons, only one ducted fan set-up is practically applicable. The front ducted fans are located at the roof, while the aft ducted fans are located halfway the fuselage height.

The front ducted fans have an airfoil like shape to reduce the drag during cruise. This because they are not tilted during cruise and they are turned off. So actually they are just increasing the frontal area which will increase the drag without having any benefits.

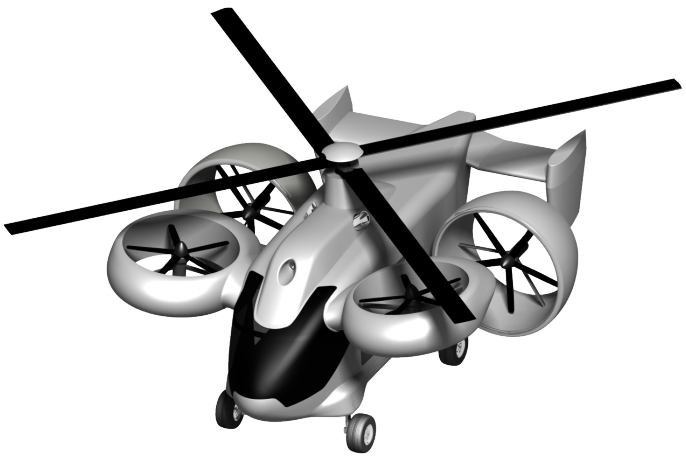

Figure 3.1: Render of the eGyro

3.3 Tail

As can be seen in Figure 3.2(b), the tail bends down towards the end. This is done such that the rotor can have a flapping angle of 8.72 [deg] and a disk angle of attack of 9.27 [deg]. In total the rotor has to be able to deflect 18 [deg] downwards at the side of the tail to reach the required minimum speed. The tail exists of a horizontal and vertical part designed according to the stability requirements. At the back of the vehicle there is a door to improve the accessibility.

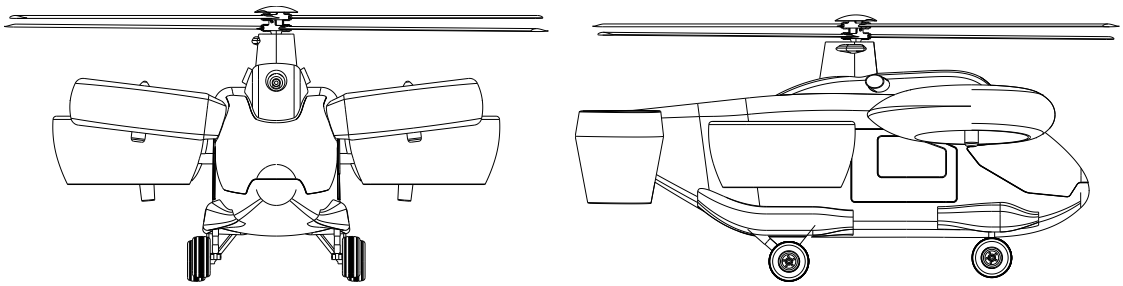

Figure 3.2: Front and side view of the eGyro

3.4 Rotor

The rotor is kept small for the landing area requirements, this can be seen in Figure 3.2(a). The rotor has almost the same width and length as the fuselage and ducted fans itself. However, because of this, four blades have to be used as can be seen in Figure 3.1

3.5 Landing Gear

The landing gear has four wheels to be able to drive and its not retractable. There is chosen for four wheels to ensure stability during driving.

4 Propulsion

In this chapter the propulsion system of the eGyro is discussed. First the ducted fan design will be discussed, which will provide an insight in the sizing of the ducts and fans. Then the powertrain will be designed and the results for an electric propulsion are stated. The chapter will be concluded with an electric block diagram and the description of redundancy in the power train when a system fails. It has to be noted that this iterative process can not be seen as separate design phases.

4.1 Ducted Fan Design

Since the vehicle will make use of ducted fans it is important to design them in very detail. The method used for the design of specific ducted fans is taken from [12]. In this section the design method for ducted fans is given step-by-step. First, the methodology for the process will be defined and after that the final values will be discussed in a separate section.

Phase I: Basic Parameters

The design of a ducted fan depends highly on the purpose of the ducted fan. For propulsion during cruise other design methods apply than for VTOL performance. Also, the cruise speed and vehicle mass are important for the design. The requirements for the mission state that the vehicle should be able to operate at 200 $\left[\frac{\text{km}}{\text{h}}\right]$, which is equal to 56 $\left[\frac{\text{m}}{\text{s}}\right]$. The MTOW, in combination with a lift to drag ratio of 4.5, provides the drag during cruise, using Equation (4.1).

$$D = \frac{MTOW \cdot g_0}{L/D} \tag{4.1}$$

g_0 is the gravitational acceleration, which is equal to 9.81 $\left[\frac{\text{m}}{\text{s}^2}\right]$. The amount of fans used for cruise performance determines the thrust per fan T with Equation (4.2). For the eGyro two ducted fans are used for cruise.

$$T = \frac{D}{n_{\text{fans}}} \tag{4.2}$$

When the thrust per fan and the cruise speed v_0 are known, the thrust power P_{t} can be calculated by multiplying both values as stated in Equation (4.3).

$$P_{\text{t}} = T \cdot v_0 \tag{4.3}$$

Next, an estimate is made for the power the engine will actually have. This value is of course higher than the thrust power calculated before. At this moment, it is assumed that the power available P_{a} will be 30% higher than the thrust power, using Equation (4.4). The 30 % increase is obtained from power available versus thrust power ranges retrieved from [12].

$$P_{\text{a}} = 1.3 \cdot P_{\text{t}} \tag{4.4}$$

After this, the radius of the actual fan inside the duct is chosen, based on a disk loading of 140 $\left[\frac{\text{kg}}{\text{m}^2}\right]$ and Equation (4.5).

$$r_{\text{f}} = \sqrt{\frac{T}{g_0 \cdot \pi \cdot \text{DL}}} \tag{4.5}$$

r_{f} is the fan tip radius and DL is the disk loading.

At last, it is necessary to calculate the density and pressure at the cruise altitude. These values are used in the calculations of phase II. It is assumed that the ceiling altitude is 2000 [m]. Using Equation (4.6), (4.7) and (4.8), the pressure and density at 2000 [m] are calculated.

$$p = p_0 \left(1 + \frac{\lambda \cdot h}{\mathcal{T}_0}\right)^{-\frac{g_0}{\lambda \cdot R}} \tag{4.6}$$

In this equation, p_0 is the static pressure at sea level, equal to 101325 [Pa], λ is the temperature gradient, equal to -0.0065 $\left[\frac{\mathrm{K}}{\mathrm{m}}\right]$, $\mathcal{T}_0$ is the standard temperature at sea level, equal to 288.15 [K] and R is the specific gas constant, equal to 287.058 $\left[\frac{\mathrm{J}}{\mathrm{kg \cdot K}}\right]$.

$$\mathcal{T} = \lambda \cdot h + \mathcal{T}_0 \tag{4.7}$$

$$\rho = \frac{p}{R \cdot \mathcal{T}} \tag{4.8}$$

Phase II: Duct Sizing

Using the thrust, power available, thrust power and cruise speed, the mass flow $\dot{m}$ through the ducted fan can be calculated using Equation (4.9).

$$\dot{m} = \frac{T^2}{2(P_\mathrm{a} - P_\mathrm{t})} \tag{4.9}$$

Since this mass flow has to be equal throughout the duct, it is used together with the cruise speed and density to calculate the inlet area A_0 with Equation (4.10).

$$A_0 = \frac{\dot{m}}{\rho \cdot v_0} \tag{4.10}$$

The fan swept area A_2 is the area of the fan where air can pass through. The center of the fan is not an open area. The electric motor is blocking some of the area. Therefore the area is calculated using Equation (4.11). r_h is called the fan hub radius by Wright, but in this case it will be equal to the motor radius, which is known from Chapter 4.

$$A_2 = \pi({r_\mathrm{f}}^2 - {r_\mathrm{h}}^2) \tag{4.11}$$

Next, the flow speed v_2 at the fan is calculated with the mass flow, the fan area from the fan diameter and the density with Equation (4.12).

$$v_2 = \frac{\dot{m}}{\rho A_2} \tag{4.12}$$

Using Bernoulli, the static pressure p_2 at the fan is calculated with the speed difference between the inlet and the fan, see Equation (4.13).

$$p_2 = p_0 + \frac{\rho}{2}({v_0}^2 - {v_2}^2) \tag{4.13}$$

Equation (4.14) calculates the exit velocity using the thrust, mass flow and inlet speed. From this exit speed, the exit area is calculated in the same way as the inlet area with Equation (4.15).

$$v_4 = \frac{T}{\dot{m}} + v_0 \tag{4.14}$$

$$A_4 = \frac{\dot{m}}{\rho \cdot v_4} \tag{4.15}$$

Now the dimensions are known, the power required P_r is calculated. An extra amount of power should be available due to swirls in the duct around the fan. Using the so-called swirl parameter K, the swirl power P_swirl can be calculated. K is dependent on the engine torque, which can be calculated using Equation (4.16).

The swirl parameter is also used to calculate the pressure p_3 behind the fan in the duct. The pressure difference front and aft of the fan is at last multiplied with the fan area and fan speed and the swirl

power is added. This will finally give the power required. The equations concerned with this swirl power are Equation (4.16) to (4.20).

$$T_{\text{q,engine}} = \frac{22.127 \cdot P_{\text{a}}}{\pi \cdot n} \tag{4.16}$$

Here, n is the value for the engine rpm and τ is the torque acting on the blade.

$$K = \frac{T_{\text{q,engine}}}{\dot{m}} \tag{4.17}$$

$$P_{\text{swirl}} = \pi \cdot \rho \cdot K^2 \cdot v_2 \cdot \ln \frac{r_{\text{f}}}{r_{\text{h}}} \tag{4.18}$$

$$p_3 = p_0 + \frac{\rho}{2}({v_4}^2 - {v_2}^2) + \pi \cdot \rho \cdot K^2 \left(\frac{\ln R_4}{A_4} - \frac{\ln R_2}{A_2} \right) \tag{4.19}$$

In Equation (4.19) the parameter R_4 and R_2 can be seen. R_2 is the ratio of r_{f} over r_{h}. R_4 is the ratio between the exit radius and an exit hub radius.

$$P_{\text{r}} = A_2 \cdot v_2 \cdot (p_3 - p_2) + P_{\text{swirl}} \tag{4.20}$$

Phase III: Iteration of the Process

It seems that the calculations are straightforward and provide the duct size and power required without any problems. This is not the case, since the calculations show that the power required appears to be higher than the power available, which was chosen based on the thrust power. This is due to the fact that the thrust power and mass flow in the beginning could not take the swirl into account. The solution to this problem is simple. The calculations are redone with an increased value of the mass flow, and redone from the point where the inlet area is calculated. Redoing all calculations after this results in a lower value for the power required and larger duct areas. This process is iterated until the power required is lower than the power available.

Since this iteration might take several attempts, a script is written to automatically perform the calculations until the power available and required power match. The mass flow increase per iteration is chosen to be 1 $\left[\frac{\text{kg}}{\text{s}}\right]$.

It is also necessary that the total speed v_{tip} of the fan tips does not exceed 70% of the speed of sound. The speed of the fan tips is a combination of the rotational speed and the flow speed. The tangential velocity v_{t} can be calculated using Equation (4.21).

$$v_{\text{t}} = \frac{n \cdot \pi \cdot r_{\text{f}}}{30} \tag{4.21}$$

Next, the speed of the fan tips is equal to:

$$v_{\text{tip}} = \sqrt{{v_{\text{t}}}^2 + {v_2}^2} \tag{4.22}$$

The speed of sound at the cruise altitude can be found using Equation (4.23).

$$a = \sqrt{1.4 \cdot \frac{p}{\rho}} \tag{4.23}$$

Eventually, the Mach number of the tips is calculated using Equation (4.24).

$$M = \frac{v_{\text{tip}}}{a} \tag{4.24}$$

Phase IV: VTOL Capabilities

Based on the cruise performance of the ducted fan, the static performance can also be determined. For the static thrust of the ducted fan, Equation (4.25) is used. The mass flow for this equation is chosen to be 95% of the mass flow during cruise.

$$T_{\text{static}} = \sqrt{2 \cdot \dot{m} \cdot P_{\text{a}}} \tag{4.25}$$

Ducted Fan Dimensions and Parameters

When using the above design methodology, final duct dimensions will come out for both the front and the aft ducted fan. In this subsection, the final values will be displayed as well as all other output parameters as described above. Of course, not all parameters are given in Tables 4.1 and 4.2. For more detailed parameters and values, the MATLAB [13] iterative program has to be consulted. Note that the values provided in Tables 4.1 and 4.2 correspond to the dimensions shown in Figure 4.1.

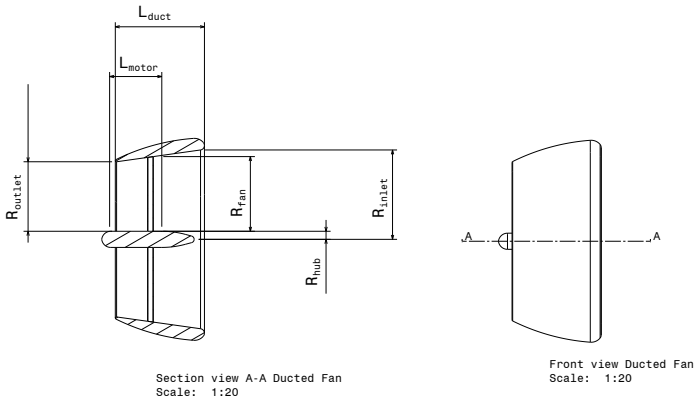

Figure 4.1: Cross section drawing of a ducted fan for the eGyro

Front Ducted Fan Using an iterative MATLAB [13] program, the desired ducted fan dimensions will come out in which the fan and motor can be placed for optimal performance. Since the process is iterative, certain input parameters need to be given. Table 4.1 shows the input and output parameters of the front ducted fan design

Table 4.1: Front ducted fan design parameters

Input			Output		
Parameter	**Value**		**Parameter**	**Value**	
MTOW	1850	[kg]	r_{inlet}	0.641	[m]
r_{f}	0.65	[m]	r_{outlet}	0.676	[m]
n_{blades}	5	[-]	h_{fan}	0.53	[m]
			r_{h}	0.1524	[m]
			h_{motor}	0.33	[m]
			P_{front}	260	[kW]

Aft Ducted Fan Using the same iterative MATLAB [13] program as used for the front ducted fans, the desired ducted fan dimensions will come out in which the fan and motor can be placed for optimal performance. Since the process is iterative, certain input parameters need to be given. Table 4.2 shows the input and output parameters for the aft ducted fan.

Phase V: Ducted Fan Blade Design

In this section, the blades for the ducted fan will be designed according to the blade design method described in [12]. The blade design method is elaborated in the same manner as for the duct design method. Note that the subscript front is used, since this example holds for the front ducted fan. The same method can be used for the aft ducted fan, by replacing the subscript front by the subscript aft.

First of all, the blade inside the duct is divided into several subsections. Of course, more subsections will yield a more exact solution. However, in this case a number of 10 subsections per blade is chosen for simplicity. Next to this, the number of blades in the duct has to be chosen. In order to avoid resonance in the duct, an odd number of blades has to be chosen. Using reference ducted fan vehicles, a number of five blades is chosen for the ducted fan.

Table 4.2: Aft ducted fan design parameters

Input			Output		
Parameter	**Value**		**Parameter**	**Value**	
MTOW	1850	[kg]	r_{inlet}	0.788	[m]
r_{f}	0.74	[m]	r_{outlet}	0.684	[m]
n_{blades}	5	[-]	h_{fan}	0.74	[m]
			r_{h}	0.1524	[m]
			h_{motor}	0.45	[m]
			P_{aft}	356	[kW]

The radius of the blade can be determined using Equation (4.26). In this equation, A_2 stands for the fan area and $n_{\text{sections,blade}}$ equals the number of subsections in which the blade is divided. Note that also r_1 has to be defined in order to get a valid equation. Therefore, r_1 is defined as the radius which is equal to the core radius (r_{h}). This core radius is based on and equal to the fan motor radius.

$$r(i) = \sqrt{\frac{A_{2,\text{front}}}{\pi \cdot n_{\text{sections,blade}}} + r(i-1)^2} \tag{4.26}$$

Next, the flow coefficient $\lambda(i)$ has to be calculated, using Equation (4.27). In this equation, v_2 equals the airflow velocity at the fan and n_{rpm} stands for the number of revolutions per minute of the fan.

$$\lambda(i) = 30 \cdot \frac{v_{2,\text{front}}}{\pi \cdot r(i) \cdot n_{\text{rpm}}} \tag{4.27}$$

When the flow coefficient is computed, Equation (4.28) provides the swirl coefficient $\eta(i)$ of the blade. The only unknown in this equation is the swirl parameter K. This parameter, however, has already been computed in the duct design. Therefore, K is already known in advance, before filling in the equation.

$$\eta(i) = \frac{K_{\text{front}}}{v_{2,\text{front}}} \cdot r(i) \tag{4.28}$$

The velocity tangential to the fan is computed using Equation (4.29). All parameters for this equation are known, such that this velocity is computed straightforward.

$$v_{\text{t}}(i) = \frac{\pi \cdot n_{\text{rpm}} \cdot r(i)}{\frac{30 - K_{\text{front}}}{2 \cdot r(i)}} \tag{4.29}$$

Using the tangential velocity and the velocity normal to the fan surface, the total velocity can be calculated with Equation (4.30).

$$v(i) = \sqrt{v_{\text{t}}(i)^2 + {v_{2,\text{front}}}^2} \tag{4.30}$$

The inflow angle of the airstream is dependent on both the tangential velocity as well as the velocity normal to the fan. The relationship between these velocities is defined by Equation (4.31).

$$\phi(i) = \arctan\left(\frac{v_{2,\text{front}}}{v_{\text{t}}(i)}\right) \tag{4.31}$$

The spacing between the rotor blades at each station is defined as the interblade gap. The interblade gap can be found using simple trigonometry, the number of blades and the radius of the blades. Equation (4.32) shows this trigonometry equation and the average interblade gap is shown by Equation (4.33):

$$s(i) = \frac{2 \cdot \pi \cdot r(i)}{n_{\text{blades}}} \tag{4.32}$$

$$s_{\text{average}} = \frac{s(i) + s(i-1)}{2} \tag{4.33}$$

When the interblade gap is known, the solidity factor for the blade can be determined. The solidity factor is defined as the ratio of blade chord to the interblade gap. Hence, Equation (4.34) shows this ratio:

$$\sigma(i) = \frac{c(i)}{s(i)} \tag{4.34}$$

Of course, also the average swirl coefficient can be computed, using Equation (4.35).

$$\eta_{\text{average}} = \frac{\eta(i) + \eta(i-1)}{2} \tag{4.35}$$

The radial thickness of the annulus, or average radius, is calculated using Equation (4.36).

$$\delta_{\text{r}}(i) = r(i) - r(i-1) \tag{4.36}$$

Using Equations (4.33) - (4.38), the axial and tangential forces acting on the blade are calculated:

$$X(i) = \rho_{\text{VTOL}} \cdot {v_{2,\text{front}}}^2 \cdot s_{\text{average}} \cdot \eta_{\text{average}} \cdot D_{\text{r}}(i) \tag{4.37}$$

$$Y(i) = s_{\text{average}} \cdot D_{\text{p}} \cdot D_{\text{r}}(i) \tag{4.38}$$

The axial and tangential force components can be translated to a blade lift and drag force using trigonometry equations. These trigonometry equations are displayed in Equations (4.39) and (4.40).

$$L_{\text{front}}(i) = X(i) \cdot \sin\phi(i) + Y(i) \cdot \cos\phi(i) \tag{4.39}$$

$$D_{\text{front}}(i) = X(i) \cdot \cos\phi(i) - Y(i) \cdot \sin\phi(i) \tag{4.40}$$

Using the lift and drag force of the the blade, the lift and drag coefficients can be computed using simple lift and drag formulas. These lift and drag coefficients are shown in Equations (4.41) and (4.42):

$$C_{d,\text{front}}(i) = \frac{2 \cdot D_{\text{front}}(i)}{\rho_{\text{VTOL}} \cdot v(i)^2 \cdot \sigma(i) \cdot s(i) \cdot D_r(i)} \tag{4.41}$$

$$C_{l,\text{front}}(i) = \frac{2 \cdot \eta(i) \cdot \sin\phi(i)}{\sigma(i)} - \frac{\sigma(i) \cdot C_{d,\text{front}}(i)}{\tan\phi(i)} \tag{4.42}$$

After the computation of the lift coefficient and the drag coefficient for the blade, the airfoil selection has to be made. In order to select a proper airfoil, first the maximum lift coefficient has to be determined. This maximum lift coefficient of the blade should be $\frac{3}{4}$ of the maximum lift coefficient which the selected airfoil can provide. The maximum lift coefficient for specific airfoils can be found in Figure 4.2.

When the airfoil for the blade is selected, the angle of attack of each radial blade station needs to be determined, according to Figure 4.2. A trendline can be made in order to find the angle of attack at the root: α_0.

With this final α_0, the blade design for the ducted fan has ended and a final configuration is found.

4.1.1 Duct Rotation Mechanism

As the aft ducted fans have to rotate, a proper mechanism for this should be thought over. The system is not worked out in detail due to the time available, nor any calculations have been done, but a simple example mechanism that could be a solution is depicted in Figure 4.3.

The duct is connected to an axis which is able to rotate in a ball bearing. The ball bearing transfers the forces to the fuselage of the eGyro. A servo motor rotates the axis to any desired angle using a gearing with a ratio of 4 to 1, to reduce the torque necessary for the movement. It has to be noted that the control forces for this mechanism are difficult to estimate since it is beneficial to attach this mechanism in the line of action of the thrust and only friction has to be overcome.

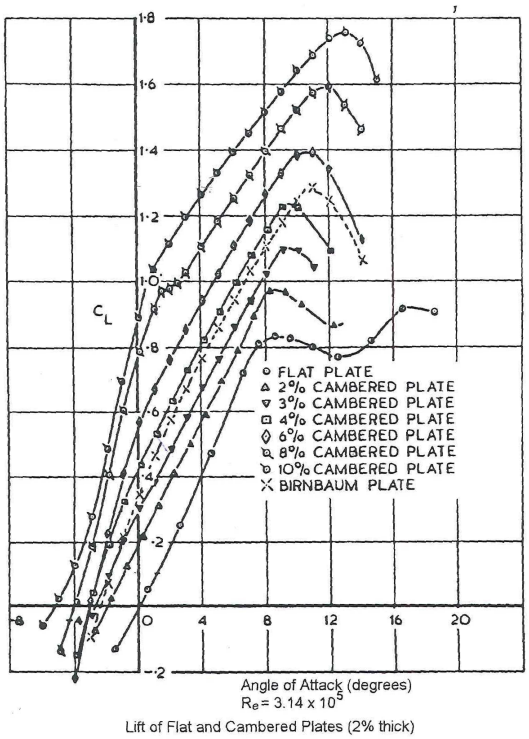

Figure 4.2: $C_L - \alpha$ curve for different types of blades [12]

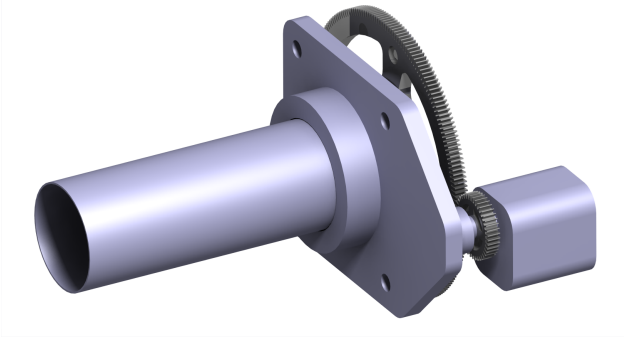

Figure 4.3: Duct rotation mechanism

4.2 Installed Power Analysis

In this section the power train will be designed for the eGyro. To have a unique market placement the feasibility of hybrid electric propulsion, which is used by the eGyro, will be investigated. This way the noise emission will be very low. In this configuration the possibility will be discussed to take-off and land using batteries and use an engine and a generator for cruise flight to power electric motors inside the ducted fan core. By using those electric motors the ducted fans can be controlled very precisely and a lot of mechanical subsystems can be dropped out of the design. At the end of this section an overview of the power train components will be given.

To design the propulsion subsystem properly it is important to know the required installed power on board, which is dependent on the performance. This depends mainly on the weight of the vehicle, but also influences the weight considerably. The initial weight estimation shows that the vehicle weight without any fuel, engines, batteries or other propulsion subsystems is equal to 1000 [kg] [4].

For the feasibility of the hybrid propulsion system, the weight of this system is important, a MATLAB script is created to iterate until the MTOW-input corresponds to the MTOW-output, where the MTOW-output uses the component weights. The component weights will be estimated below to calculate this

MTOW. To come up with the MTOW, the weights of all parts of the powertrain and the payload are added to the Operational Empty Weight (OEW). The power train weight consists of the fuel weight, battery weight, engine weight, generator weight, the motor weights in each ducted fan and an extra weight for cables and unforeseen parts of 10 [kg]. All weights of these parts are based on the power required. However, the power required is based on the ducted fan design method [12] and Section 4.1, which depends on the same vehicle MTOW. To overcome this problem, MATLAB is used to calculate the power required based on a range of MTOW inputs from 1400 to 2000 [kg]. Next, the weights of the aforementioned parts are calculated with the power required. At last, the two values for the MTOW are compared to each other. The iteration process terminates if the result of the weight calculation is within 1% of the estimated MTOW value. Using this method, the MTOW equals 1850 [kg].

Electric propulsion results in a lot of redundancy within the power train. Current helicopters used for EMS-purposes require two engines for redundancy reasons. Since two engines are not required in this configurations to comply with regulations [6] in this vehicle, this will save weight, which is replaced by i.e. batteries and motors. The engine and motor are a system which can be placed in the vehicle with a lot of freedom, since no mechanical connections have to be made to other systems if the electric powertrain is used. Eventually it is chosen to be on the top of the fuselage, since this is easier for exhausting the gasses and makes it possible to have large doors.

4.2.1 Engine Selection

The power required during cruise, which is equal to 357 [kW], as described in Subsection 4.1, which has to be provided by the aft ducted fans and for which an efficiency rate of 70% is taken into account to accommodate for losses at altitude [14]. Taking this into account, the engine should be designed for $357/0.7 = 510$ [kW] to provide enough power at height. This value is the output of the MATLAB [13] iteration.

The power required for the VTOL operation equals 617 [kW], as described in Subsection 4.1, which is provided by all four ducted fans. After a few iterations, the selected engine for the required powers and weight is therefore the Turbomeca Arriel 2C2 engine [15], where it has to be noted that the batteries will be charged during cruise flight. This will be explained later in the battery selection, since in this iterative process it is hard to see this as separate systems. An extensive research process is performed and that the Turbomeca Arriel 2C2 engine came out as the best choice for the eGyro.

The Arriel 2C2 engine provides a maximum continuous power of 612 [kW], which is more then enough for the cruise phase. Next to this, the engine has a maximum power output of 713 [kW] for two minutes, which therefore serves as a backup for battery failure during VTOL operations. Note that the 713 [kW] is enough for VTOL operations for a climb rate of at least 5 $\left[\frac{\text{m}}{\text{s}}\right]$, such that a safe landing can be performed using this power. Hence, the overboost function is not required. Also, by making use of MATLAB, it is calculated that the engine can perform a maximal VTOL operation using a Rate of Climb (RoC) of 10.57 $\left[\frac{\text{m}}{\text{s}}\right]$, since the engine is selected for cruise flight including charging of the batteries. However, since the electric motors are not designed for this rate of climb, the rate of climb is limited at 5 $\left[\frac{\text{m}}{\text{s}}\right]$, which is almost entirely covered by the continuous power of the engine. Next to these characteristics, the engine has a relatively low weight compared to other engines with the same power output. In Table 4.3 the most important parameters of the chosen engine can be found. More specifications of the engine can be found in [15].

Table 4.3: Parameters Turbomeca Arriel 2C2 engine [15]

Parameter	**Value**
Continuously speed [rpm]	52,764
Mass [kg]	132
Size ($l \times w \times h$) [m]	$1.015 \times 0.498 \times 0.576$
Power continuous [kW]	612
Power 2 min. overboost [kW]	713

In order to calculate the total fuel consumption for this engine, use can be made of Equation (4.43).

$$W_{\text{F}} = \text{SFC} \cdot P_{\text{cruise}} \cdot 1.15 \cdot t_{\text{cruise}} + \text{SFC} \cdot P_{\text{charge}} \cdot t_{\text{charge}} = 311.5\ [kg] \tag{4.43}$$

In above formula, the SFC equals 0.274 $\left[\frac{\text{kg}}{\text{kWh}}\right]$ and the 1.15 factor is used for reserve fuel.

4.2.2 Battery Weight and Cost Calculation

In order to reduce noise and emissions of the designed vehicle, batteries are used during the VTOL operations of the vehicle. For ten minutes of VTOL, 617 [kW] is required from the battery package, as described in Subsection 4.1, provided by the front and aft ducted fans. The capacity of the batteries is designed such that the eGyro is capable of a 10 [min] ascend, which will cover three times 2 [min] ascend and 2 [min] descend. These two minutes are determined from the RoC 5 $\left[\frac{\text{m}}{\text{s}}\right]$ characteristics, empirical data in current EMS vehicle and the transition to the cruise phase from the VTOL phase – and the other way around – and will be a fixed parameter in further design of the eGyro. This 617 [kW] for ten minutes therefore equals 103 [kWh]. Assuming that the necessary amount of energy equals 105 [kWh] and using a specific energy of 0.4 $\left[\frac{\text{kWh}}{\text{kg}}\right]$, the total battery weight equals 257.1 [kg]. This specific energy is based on the development of lithium-ion batteries, with a degradation of 80% at the end of life, for cells with a specific energy of 0.5 $\left[\frac{\text{kWh}}{\text{kg}}\right]$ in 5 year. This estimation is done using references from current state of the art batteries [16], batteries used in the past and expected development for lithium-ion cells in the future, estimated for cells in 2018 using the expertise of a professional at the Nuon Solar Team [17]. This estimation is not based on development within 10 years since the cells have to be reliable and certified for aerospace applications.

With a price of €95.40 per [kWh] for the battery [7], the total price for the battery package therefore can be seen in Equation (4.44).

$$C_{\text{battery,total}} = C_{\text{battery per kWh}} \cdot E_{\text{kWh}} = 95.40 \cdot 105 = e\ 10017 \tag{4.44}$$

The cost for the charging of the battery can also be calculated, when using a price of €0.21 per [kWh] [7] on general electricity, as seen in Equation (4.45).

$$C_{\text{battery,charging}} = \frac{C_{\text{energy per kWh}} \cdot E_{\text{kWh}}}{\text{DoD}} = \frac{0.21 \cdot 105}{0.8} = e\ 27.56 \tag{4.45}$$

Note that the 0.8 correction factor is accounting for the depth of discharge of the batteries, since the energy charged are not fully getting out of the battery package. Hence, to charge the batteries after a mission, the price equals €27.56. This price is not very high when comparing to the fuel costs when using a regular engine instead of batteries, as seen in Equation (4.46).

Since the battery package is required to be as weight efficient as possible, degradation of cells is critical. The used cells have a very high specific power and will still be useful in other applications, like the automotive industry, when the cells will not be efficient enough for the eGyro. This increases the usability of the cells and makes it possible to have a more sustainable vehicle without disposing the batteries often, since not only lifetime but also temperature will have a lot of influence on the cell performances. Charging and discharging is heavily depending on the circuit of the separate cells, which is not defined in more detail and should be looked into. Basic experience and knowledge about batteries is used to check the feasibility, although this has to be investigated in later design.

$$W_{\text{F,VTOL}} = \text{SFC} \cdot P_{\text{a}} \cdot t_{\text{mission}} = 0.304 \cdot 617 \cdot 0.17 = 32\ [\text{kg}] \tag{4.46}$$

This value of 32 [kg] of fuel yields a price of €21.41, when assuming the Jet A fuel price to be approximately €2.08 per gallon [18]. Hence, the 32 [kg] equals 70.55 [lb] and the specific density of Jet A fuel equals 6.84 $\left[\frac{\text{lb}}{\text{US gallon}}\right]$. The price of €21.41 for the fuel price can be calculated using Equation (4.47).

$$C_{\text{fuel,engine}} = \frac{W_{\text{F}}}{\rho} \cdot C_{\text{fuel}} \tag{4.47}$$

Note that for the fuel price the current market price is obtained, whereas for the electricity price the general price for households is used. Therefore, the price difference between fuel costs and battery charging cost will be negligible. It has to be noted that fuel prices fluctuate a lot. In the Netherlands most trauma helicopters are based on airports or army bases where a lot of open space is available. This makes it possible to charge batteries using solar cells and thus charge in a sustainable way with less loses

due to converting Alternating Current (AC) to Direct Current (DC). The feasibility of this needs to be investigated in later development.

Considering the charging of the batteries, it is important that the selected engine provides enough power to charge a part of the batteries in mid-air. Using the extra power of the Arriel 2C2 engine and maximally an hour cruise of the vehicle, the engine is capable of charging the battery for an extra VTOL ascend and descend operation, which can be seen in Equations (4.48) to (4.51).

As can be seen in the equations, the required energy is necessary for four VTOL operations: four ascends and four descents. Next, the required charging energy is calculated by subtracting the full battery energy from the required energy. In order to obtain the required time, the energy required can just be divided by the excess power of the engine. Note that due to the depth of discharge of the batteries, the required charging energy has to be divided by 0.8. The final charging time to obtain an extra VTOL operation is found to be 52 [min] cruise time, based on a charging power of 71.4 [kW]. In this charging power, the 30% loss of the engine performances at height is taken into account.

$$E_{\text{req,total}} = 3 \cdot E_{\text{req,VTOL}} + 1 \cdot E_{\text{req,VTOL}} \tag{4.48}$$

$$E_{\text{req,charge}} = E_{\text{req,total}} - E_{\text{bat,full}} \tag{4.49}$$

$$t_{\text{charge}} = \frac{E_{\text{req,charge}}}{\text{DoD} \cdot P_{\text{charge}}} \tag{4.50}$$

$$P_{\text{charge}} = P_{\text{engine}} - P_{\text{cruise}} \tag{4.51}$$

Note that the batteries can also be charged on the ground. Hence, the batteries are charged using the electricity network and the battery in the eGyro can be replaced by another, charged, battery after a mission.

Also note that during the VTOL operation, the engine is on a standby mode in order to account for unforeseen circumstances where the use of the engine is necessary.

The total volume of the batteries calculated in this subsection equals 143 [L], divided over the floor area with an assumed thickness of 25 [cm] and therefore a surface area of 0.715 [m^2]. For the calculation of the battery size, use can be made of the battery size as stated in [7].

4.2.3 Generator Weight Calculation

When using the report of high power density generator concepts for aerospace electric power [8], use has been made of a generator with a specific energy of 0.1 $\left[\frac{\text{kg}}{\text{kW}}\right]$. Therefore, the generator weight equals 71.3 [kg] in order to provide all the necessary power for the vehicle to perform all the operations. This sizing is based on the maximum engine output power, including overboost. The implemented generator is able to operate at the required rpm rate (3,000 to 100,000 [rpm]) and power (10 to 1000 [kW]) in combination with the engine, which delivers approximately 713 [kW] at 53,000 [rpm] [15]. The size of the generator is based on an upscaled existing generator design [8] and is estimated to be 0.40 [m] in diameter and 0.42 [m] in length based on the power density and the engine size [8] and verified for feasibility.

4.2.4 Electric Motor Weight Calculation

In order to calculate the electric motor weight, the electric motors for both the front and the aft ducted fan have to be selected. The distinction can be made between brushed and brushless motors (Brushless permanent magnet DC motor (BLDC)). For powering the ducted fans the motor will be brushless, since this will include more torque per weight and more torque per Watt, which will result in an increased efficiency and a lower motor weight. Other advantages are that BLDC make less noise, have a longer lifetime and have a higher reliability due to no rotating contact points with respect to brushed motors. Since the motors will be placed in the center of the ducted fan, the motor should not only be light, but should also be small. For this reason a high-end electric motor is chosen, which can be seen in Figure 4.4. This motor is specially designed for ducted fans, so this will be a reliable motor and its performances is unrivaled [19].

A single electric motor will not be powerfull enough, but this will be solved by stacking motors, which can be seen in Figure 4.5. The efficiency of the motor will be 95% and this motor will be developed

for applications using different rpm's. This lower rpm is needed to have the fan tips not moving faster than the speed of sound. It is assumed that the power density of the models with lower rpm's, but higher diameters, will be equal to the developed model, which is 8.22 $\left[\frac{\text{kW}}{\text{kg}}\right]$. The corresponding power density is then 22,000 $\left[\frac{\text{kW}}{\text{m}^3}\right]$. This assumption is validated by contacting the developing company [19]. The diameter is increased to decrease the height of the stacked motor configuration. The diameter of the current motor is roughly 15 [cm], but will be increased as explained before. The maximum diameter of the fan core and the coherent length will be a leading parameter in designing the fan. Using the stated values it is possible to estimate a weight for the front motors and aft motors using a MATLAB [13] script to iterate towards the total weight of the power train. The front motors will weigh 31.7 [kg] and the aft motors will have a weight of 43.4 [kg] The motor size is determined with the calculated powers and sizes of the motor [19]. Using the power density with a motor of 15,24 [cm] (6 inches) the height of the cylindrical motor will be 0.33 [m] and at the aft ducted fans, both will be 0.45 [m] high. These sizes are possible since the height of the ducted fans is approximately 70 [cm].

Figure 4.4: Electric motor [19]

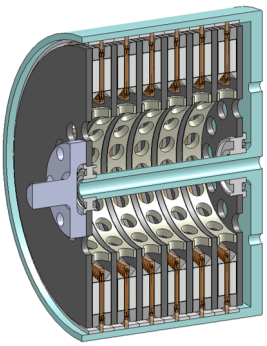

Figure 4.5: Electric motor configuration with more motors (cut-out) [19]

4.2.5 Results Power Train

In Table 4.4, the weights for the power train are given to give an overview of all components, getting to the conclusion that a hybrid powered aircraft is feasible and this will be used in the further design. With this result it is beneficial if all moving mechanisms can be outfitted electrically. In Table 4.5 an overview is given of all powers of the power train.

4.3 Electric Block Diagram

In this section, the electric subsystem of the vehicle is discussed. The complete electric subsystem is shown in Figure 4.6. Note that this is just a schematic overview of the electric subsystem, which does not result in a closed electric circuit.

As can be seen in the figure, the generator is connected to the battery package. This combination will deliver the necessary power for:

Table 4.4: Component weight of the power train

Component	Mass [kg]
Engine	132
Generator	71.3
Battery	257.1
Motors front	31.7
Motors aft	43.4
Fuel	311.5
Extra	10
Total	857

Table 4.5: Component powers of the power train

Component	Power [kW]
Engine	612
Generator	617
Motors front	260
Motors aft	357
Ascend	617
Descend/hover	527
Charging	71.5

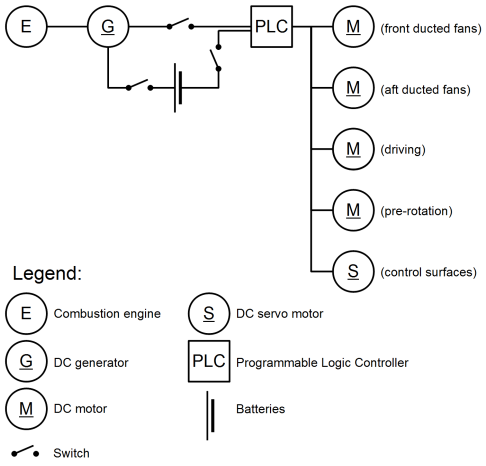

Figure 4.6: Electric Block Diagram for the eGyro

- Four electric motors for the ducted fans
- Two electric motors for the driving capability of the vehicle
- Medical equipment
- Avionics
- Communication
- Control Surfaces
- Pre-rotation of the rotor

Note that during cruise, the engine is used to power the systems that require electric power. Of course, the most power requiring parts are the electric motors of the ducted fans. The eGyro uses the full electric flying principle, such that there are no pneumatic systems or hydraulic systems to control the control surfaces.

4.4 Redundancy in Propulsion

In this section the redundancy in every phase of the mission will be elaborated. Failure in propulsion can occur by a failure in the hybrid (engine/generator) configuration, in the batteries and in the electric motors. The consequences of those failures will be explained for every mission phase, starting with the cruise phase. Next, the VTOL phases will be explained and at last, a failure in the transition will be explained. These risks are at the end of this chapter displayed in a risk map. The numbers in the subsections correspond to the numbers in the risk map, which can be found later in Section 10.4.

4.4.1 Cruise

During cruise, the engine is used to power a generator which will provide electric power to the motors in the aft ducted fans. The power required in this phase of flight is 510 [kW]. It has to be noted that during cruise the rotor is in auto-rotation, such that it will be possible to land in case of full power failure.

Failure of Engine or Generator (1)

In case of engine failure, it is assumed that the generator does not provide any power. In this phase of the flight the batteries will power the aft ducted fans to be able to fly to a safe landing spot. The batteries are designed for 10 minutes vertical flight. In the worst case scenario the engine fails when the second cruise phase is started and the cruise phase between the initial take-off and landing at the crash site is not enough to charge the batteries fully. This means that the vehicle has taken off, landed and took off again, which can be seen in Figure 4.7. It has to be noted that in this phase of the design the transition phase is not worked out accurately which results in a simplified mission profile. The assumptions are checked to be reasonably accurate. When the first cruise phase in between is infinitely small, the battery will only have a small amount of energy left. In case of a full battery at the end of the cruise phase, the first take-off can be eliminated in the calculation, which will be the case if the first cruise phase takes longer than 13 minutes. Of course, the situation will be the same if this cruise phase is longer as the batteries can not be charged any more then. The remaining energy in the batteries for the cruise to a crash landing spot can be calculated by subtracting the energy for three vertical maneuvers and the required crash maneuver from the full battery energy and adding the energy added to the battery during the charging in the first cruise phase. With this energy, the power for cruise flight, the cruise speed and the maximum cruise distance to a crash landing spot can be calculated easily. In case of no cruise flight, this will result in a distance of 10.4 [km]. For a cruise flight longer than approximately 15 minutes, this range is extended to 18.5 [km].

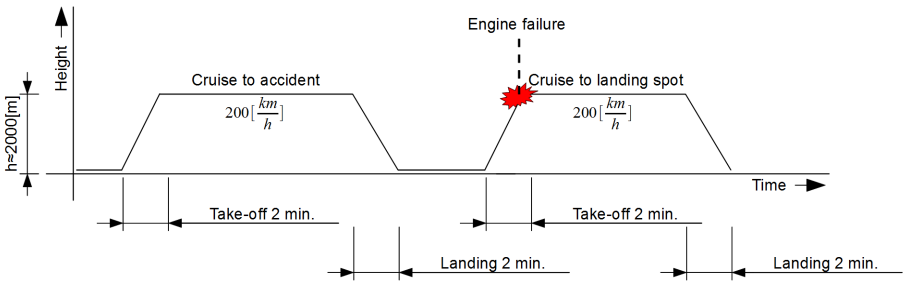

Figure 4.7: Simplified mission profile in case of engine failure

Failure of Batteries (2)

Since the batteries are only used for VTOL flight and the transition, failure of batteries is not a big problem for the cruise phase. The only thing that has to be noted here is that redundancy is lost here, but landing on auto-rotation is still possible.

Failure of Electric Motors (3)

Since the ducted fans are driven by a stack of electric motors it is probably not fatal if one motor fails. Since the amount of motors is not exactly known because only the prototype specifications are given, the

power loss in case of motor failure is not known. This will hold for all flight configurations, but of course in cruise, a failing motor in the front ducted fans results in no difference for the cruise phase where the vehicle is currently in.

4.4.2 VTOL

During take-off and landing, the vehicle will be lifted by the ducted fans. For take-off, the power required is higher than for descend, to be able to achieve a climb rate. The power for take-off is estimated at 617 [kW] and for the landing phase 527 [kW], which means 90 [kW] extra power is used during ascending at a RoC of 5 $\left[\frac{\text{m}}{\text{s}}\right]$, which can be calculated using Equation (4.52).

$$P_{\text{climb}} = \text{RoC} \cdot \text{MTOW} \cdot g_0 \tag{4.52}$$

Failure of Engine or Generator (4)

An engine failure during VTOL does not harm this phase of the flight itself, to not increase the danger incorporated. During normal conditions, in this phase the engine is running in stand-by modus. The mission will directly be aborted since no cruise is possible for a reasonable time period using only battery power.

Failure of Batteries (5)

In case of battery failure the chosen engine can use its overboost function. This means that the engine will be able to produce more power, but will not be able to do this continuously. This overboost function for the chosen engine equals 713 [kW] for a maximum time of 2 minutes [15]. Since the power required for descend equals 527 [kW], which will be covered by the engine easily, ascending is also possible without using the overboost function of the engine, but the maximum RoC without overboost will be 4.7 $\left[\frac{\text{m}}{\text{s}}\right]$, as seen in Equation 4.52. Using the overboost it is possible to reach the desired RoC since the nominal duration for this maneuver is covered in the overboost time span of 2 minutes. This process can be started within a few seconds, since the motor is running idle in this situation.

4.4.3 Transition

During the transition phase the RoC will be zero. This means there is a power excess since the 5 $\left[\frac{\text{m}}{\text{s}}\right]$ RoC increases the power required for the take-off. This excess power will be used to keep the vertical component of the thrust constant, while the aft ducted fans will be tilted to start producing forward thrust.

Failure of Engine or Generator (6)

In the transition period the engine will start providing power. In case of failure, the transition will be stopped and the same consequences will be involved as with an engine failure during VTOL maneuvers. The mission will be aborted immediately.

Failure of Batteries (7)

If during the transition phase the batteries will fail, the mission will also be aborted, but there will still be a safe powered landing possibility. The engine can provide enough power to fly the whole mission by only lowering the RoC by a small amount. Since there are no back-up options besides landing on auto-rotation, the mission will be ended.

5 Aerodynamics

The rotor is one of the most important parts of the vehicle, providing the lift during cruise without the need for shaft power. The sizing and dimensioning of the rotor is outlined in this chapter along with the aerodynamic characteristics. The aerodynamics of the fuselage and other parts of the vehicle are also influencing the performance of the aircraft and should therefore be taken into account as well.

5.1 Rotor Sizing

For the preliminary sizing of the rotor, the disk loading is based on statistics. The method is obtained from [20] and [21]. For the MTOW a minimum and maximum disk loading can be found. From this range of disk loading, the radius can be obtained with Equation (5.1). Here DL is the disk loading and r the radius.

$$r = \sqrt{\frac{\text{MTOW}}{\text{DL} \cdot \pi}} \tag{5.1}$$

In this case a small landing area is required, to obtain this, the disk loading that results into the smallest radius is chosen. This value is then used as the minimum rotor radius. After that, it needs to be checked whether the tip speed exceeds the sound barrier. The tip speed depends on the rotational speed necessary for auto-rotation. This is further discussed in the auto-rotation section later on. The tip speed has to be lower than 0.95 Mach to have a safe margin, which prevents shock waves from occuring on the blades [21]. On top of that, the forward velocity has to be taken into account. This results in Equation (5.2).

$$\omega_\text{r} = a \cdot 0.95 - V_\text{hor} \tag{5.2}$$

Here a is the speed of sound, V_hor the horizontal speed and ω_r the tip speed. Next, the solidity ratio can be determined from Equation (5.3).

$$\sigma = \frac{n_\text{blades} \cdot c}{\pi \cdot r} \tag{5.3}$$

Where n_blades is the number of blades, c is the chord and σ is the solidity factor. Basically the solidity factor is the area of the blades divided by the rotor disk area. However, the chord and radius are not known yet. The $\frac{C_\text{T}}{\sigma}$ ratio versus the advance ratio, in which C_T is the thrust coefficient, is obtained from [21]. The advance ratio is the forward speed divided by the tip speed. For the forward speed the cruise speed is used. The tip speed is known from the auto-rotation conditions, which will be explained in Section 5.2. The graph differs for level flight, steady turns and turbulence. This means that for each of these conditions the C_T has to be calculated. The equation is given by Equation (5.4).

$$C_\text{T} = \frac{T_\text{rotor}}{\rho \cdot \pi \cdot r^2 \cdot {\omega_\text{r}}^2} \tag{5.4}$$

The thrust is different for each of the three conditions. For the level flight the thrust equals the weight. For the steady turn a load factor of $\frac{1}{\cos(30)}$ is used and for the turbulence 3.5 [22]. For the structural analysis a load factor of 3 and a safety factor of 1.5 is used to make sure that the turbulence and the steady turn load factor are within the limits. This yields a load factor of 4.5 and thus the load factor for turbulence is not exceeding this value. Now the thrust coefficient can be calculated from the known thrust, the radius obtained from the disk loading and the tip speed from auto-rotation conditions. Using these thrust coefficients and the advance ratio, the solidity ratio can be obtained. Then the highest solidity ratio of the three cases is taken to calculate the chord with Equation (5.5) [21].

$$c = \frac{\sigma \cdot \pi \cdot r}{n_\text{blades}} \tag{5.5}$$

When the chord is known the aspect ratio can be calculated with Equation (5.6). The aspect ratio needs to be between 14 and 20. The closer towards 20, the better the aerodynamic properties [23]. Since for auto-rotation, good aerodynamic properties are needed, such that a high aspect ratio is aimed for.

$$AR = \frac{r}{c} \tag{5.6}$$

To get to a decent aspect ratio and maximum speed, the chord, radius and number of blades are varied. The radius must be higher than the radius for the minimum disk loading. Two blades are tried first because this is the simplest solution for the hub design.

Table 5.1: Iteration of rotor parameters for two blades

Number of blades [-]	Radius [m]	Chord [m]	Aspect ratio [-]	Solidity ratio [-]	Max velocity $\left[\frac{\text{km}}{\text{h}}\right]$
2	6	0.3	20	0.0318	144
2	6	0.4	15	0.04242	162
2	4	0.3	13.33	0.0477	172
2	8	0.3	26	0.0239	122
2	8	0.5	16	0.0398	158
2	3	0.2	15	0.0424	162

However from Table 5.1 it can be seen that it is not possible to achieve the 200 $\left[\frac{\text{km}}{\text{h}}\right]$ cruise speed, let alone a decent maximum speed, and a reasonable aspect ratio and radius at the same time. Therefore the iteration process is done again with four and even six blades.

Table 5.2: Iteration of rotor parameters for 4 and 6 blades

Number of blades [-]	Radius [m]	Chord [m]	Aspect ratio [-]	Solidity ratio [-]	Max velocity $\left[\frac{\text{km}}{\text{h}}\right]$
4	3.16	0.2	15.8	0.0806	220
4	3.16	0.16	19.75	0.0645	198
4	3.5	0.25	14	0.0909	223.2
4	3.5	0.18	19.44	0.0655	198
4	4.24	0.2	21.2	0.0601	194
4	4.24	0.28	15.1429	0.0841	227
4	6	0.4	15	0.0849	227
6	3.12	0.16	19.5	0.0979	241

In table 5.2 the most relevant values are displayed. It can be seen that six blades give the best result. But this will make the hub mechanism very complex and expensive. Therefore, a rotor with four blades is chosen. The aspect ratio improvement for a radius of six compared to 4.24 [m] is negligible. Hence a radius of 4.24 [m] is chosen. This configuration would just fit in a 6 by 6 [m] square if the rotor blades are positioned in a diagonal way. The required landing area, is based on the vehicle dimensions with a 50 percent margin on each side of the surface. Adding the 50 percent of the space on each side of the rectangular surface yields a landing area of 12 [m] by 12 [m], which was a requirement specified in the Baseline Report. With this radius, the most feasible chord is 0.28 [m]. This gives an aspect ratio of 15.1429, a solidity ratio of 0.0841 and a maximum speed of 227 $\left[\frac{\text{km}}{\text{h}}\right]$.

5.2 Auto-rotation

The auto-rotation of rotors is a property that requires numerical calculations in order to arrive at the characteristics that are associated to auto-rotation. Obtaining the proper values for the characteristics is an iterative process. The auto-rotation mainly depends on the angular velocity and the induced velocity. From those parameters the forces on the rotor can be obtained by first calculating the thrust and drag. Finally, the lift and relevant angles can be calculated. When the parameters are such that the torque is zero, the state of auto-rotation is reached. When this happens the parameters should be used in the design. When the state of zero torque is not reached for example, the number of blades and rotor diameter has to be changed.

5.2.1 Airfoil Selection

In order to design a rotor the most suitable airfoil needs to be selected. Different airfoils have been in use in helicopter and auto-gyro design over time. When choosing airfoils to function as rotor blades the most important factors to take into account are the pitching moment, the drag and the lift. The pitching moment should be as close to zero as possible and the drag should be as low as possible while the lift characteristics are still sufficient, so that the lift to drag ratio is as high as possible. Different airfoils have been used over time for rotor design, among which are for example the SG6042, the NACA 0012 and NACA 23012. The latter two are classic configurations for aircraft wings but have also been used for rotor blades. The NACA 0012 has decent lift characteristics for rotor blades. However it has no camber and is one of the older airfoils that are not optimal for rotating wings. More recently the NACA-H series have been in use. The NACA 7-H-12, NACA 8-H-12, NACA 9-H-12 and NACA 10-H-12 are designed for helicopter and auto-gyro use, as indicated by the 'H' in the name. The first number in the name indicates the series and the last number is a measure of the thickness to chord ratio, similar as in other NACA airfoils. The NACA H-series have proven to be more suitable than other NACA airfoils, mainly because they are designed for minimal pitching moment and optimal lift. Therefore one of these airfoils is chosen for the design of the rotor.

From a test carried out by NACA on the four NACA H-series, as described in [24], it appeared that the 8-H and 9-H have near zero pitching moments while the 9-H and 10-H have small negative pitching moments. Also the maximum lift of the H-airfoils are lower than those of the NACA 0012 and NACA 23012 but are able to maintain lift over a wider range of angles of attack. The drag of the NACA 7-H-12 is higher than those of the 8-H-12, 9-H-12 and 10-H-12, but still lower than the NACA 0012 and NACA 23012. The drag also increases fast with increasing lift for all H airfoils. The general characteristics and profile drag losses for different flight conditions are outlined in Figures 5.1 and 5.2, respectively.

It can be concluded that the NACA-8-H-12 and 9-H-12 have the least profile drag losses and while the NACA-8-H-12 has the smallest pitching moment coefficients. Because all of this, the NACA-8-H-12 airfoil is chosen for the design of the rotor.

The $C_l - \alpha_\mathrm{b}$, $C_d - \alpha_\mathrm{b}$, $C_l - C_d$ and $C_\mathrm{m} - \alpha_\mathrm{b}$ curve for a Reynolds Number of 10^6 for the NACA 8-H-12 are outlined below in Figures 5.3, 5.4, 5.5 and 5.6, respectively taken from [25].

5.2.2 Rotor torque

The most important characteristic of auto-rotation is that the net torque on the rotor shaft has to be equal to zero. The rotor is driven by the airflow that passes through the rotor [26]. To be able to start the auto-rotation phase, the rotor needs pre-rotation. This is further discussed in the performance chapter.

For the calculation of the auto-rotation conditions, a MATLAB script is written. The outline of this script is given in Figure 5.7. This script is mainly based on the Glauert method which is most applicable to the auto-gyro [27]. This method combines the equation of the torque and the thrust. This then yields a combination of the induced velocity with the tip speed [27].

The inputs are the weight of the vehicle $MTOW$, the air density ρ, the lift curve slope a, and the flight path angle γ. The radius r, number of blades n_blades, and the chord c are also inputs, although they have to be iterated as explained in the section preliminary sizing. They have to be iterated so that the maximum speed can be achieved, the aspect ratio remains between 14 and 20 and the radius is within the landing area requirements.

In the next block, the forward velocity v_0 is increased step wise to calculate the auto-rotation conditions for multiple speeds. Then, the basic rotor parameters listed below are calculated. The angle of attack

TABLE V.- AIRFOIL SECTION CHARACTERISTICS

$[R = 2.6 \times 10^6]$

Section characteristics \ NACA airfoil section		7-H-12	8-H-12	9-H-12	10-H-12	3-H-13.5 (reference 1)
$(c_l/c_d)_{max}$		106	135	152	149	163
$c_{m_{a.c.}}$		------	0.005	-0.012	-0.022	0.003
$c_{d_{min}}$		0.0055	0.0046	0.0046	0.0043	0.0050
Low-drag range		------	0.25 to 0.91	0.39 to 0.93	0.30 to 0.76	0.38 to 0.88
$c_{l_{max}}$	Smooth	1.34	1.26	1.26	1.30	1.20
	Rough	1.10	1.13	1.12	1.14	--------
M_{cr} at c_{l_1}		0.601	0.569	0.569	0.619	0.56
c_{l_1} (approx.)		0.42	0.57	0.60	0.46	0.60
t/c at 0.25c		0.119	0.117	0.117	0.108	0.1208
a.c. position	x/c	0.250	0.278	0.267	0.261	0.250
	y/c	0.021	0.020	0.025	0.021	--------

Figure 5.1: Airfoil section characteristics of the NACA H series

TABLE VII.- COMPARISON OF ROTOR-BLADE PROFILE-DRAG LOSS FOR VARIOUS FLIGHT CONDITIONS OF THE SAMPLE HELICOPTER

	Conditions (see table VI)			Rotor-blade profile-drag loss, hp										Remarks
				NACA airfoil section										
				7-H-12		8-H-12		9-H-12		10-H-12		23012		
				Smooth	Rough	Smooth	Rough	Smooth	Rough	Smooth	Rough	Smooth		
1	W/S = 1.55	μ = 0		17.2	30.7	14.4	32.3	17.3	30.1	13.4	31.9	20.1	}	Effect of loading (hovering flight)
2	3.33	0		25.9	33.7	18.5	39.0	17.2	38.2	17.8	41.5	24.1		
3	5.42	0		42.6	116.2	56.8	112.1	57.9	132.2	114.3	-----	42.6		
4	μ = 0	W/S = 2.5		22.0	31.9	16.3	35.3	15.4	33.8	14.0	35.9	21.7	}	Effect of tip-speed ratio
5	.2	2.5		24.8	37.4	21.2	41.4	20.0	39.3	23.6	41.7	25.7		
6	.3	2.5		42.3	73.4	36.7	65.7	37.9	66.1	40.3	52.0	31.0		
7	W/S = 1.9	μ = 0.2		22.0	34.8	17.5	37.7	19.4	35.5	17.6	37.9	23.5	}	Effect of loading (forward flight)
5	2.5	.2		24.8	37.4	21.2	41.4	20.0	39.3	23.6	41.7	25.7		
8	3.1	.2		30.6	58.0	28.6	57.3	28.8	59.4	39.5	45.9	29.2		

NACA RB No. L5R02

NATIONAL ADVISORY COMMITTEE FOR AERONAUTICS

Figure 5.2: Comparison of the profile-drag loss for different NACA airfoils

of the blade is obtained from statistics with Equation (5.7) obtained from [27]. The result is shown in Figure 5.10.

$$\alpha_b = \frac{15 \cdot \pi}{180 \cdot e^{0.008 \cdot v_0}} \tag{5.7}$$

Furthermore, the parasite drag is calculated as obtained in the section about drag. From this, the flight path angle γ and the weight $MTOW$, the angle of the disk plane α_d can be obtained with Equation (5.8). The result obtained for the eGyro is displayed in Figure 5.8.

$$\alpha_d = \sin^{-1}\left(\frac{D_p}{MTOW}\right) + \gamma \tag{5.8}$$

To be able to start the auto-rotation calculations itself, an initial value for the advance ratio μ_a and the tip speed ω_r is taken. The auto-rotation calculations are then iterated and the newly obtained values for μ_a and the tip speed are implemented. As stated before, the net torque has to be zero for the

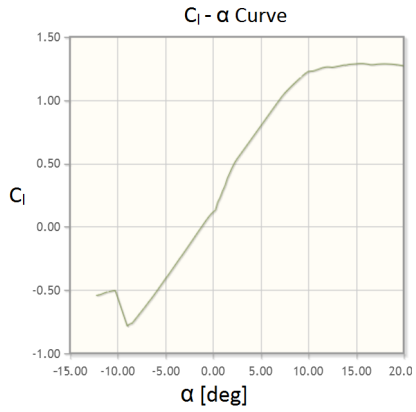

Figure 5.3: $C_l - \alpha_\mathrm{b}$ curve for the NACA 8-H-12

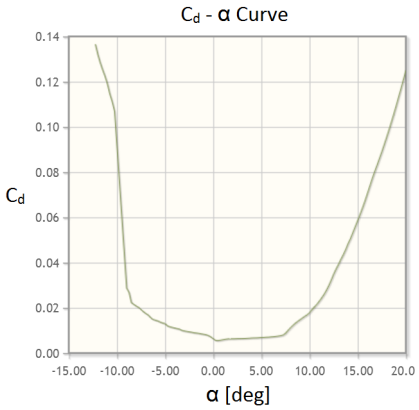

Figure 5.4: $C_d - \alpha_\mathrm{b}$ curve for the NACA 8-H-12

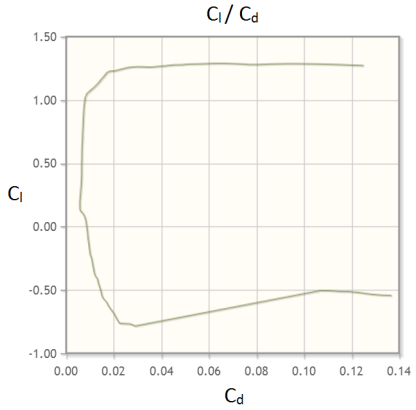

Figure 5.5: $C_l - C_d$ curve for the NACA 8-H-12

auto-rotation. From this, Equation (5.9) holds.

$$Q = 0 = \frac{\frac{\sigma^2 \cdot {C_d}^2}{64}}{{v_i}^2 \cdot (v_0 \cdot \sin(\alpha_\mathrm{d}) - v_i)^2} \cdot (\omega_\mathrm{r})^6 - {v_0}^2 \cdot \cos(\alpha_\mathrm{d})^2 - (v_0 \cdot \sin(\alpha_\mathrm{d} - v_i)^2) \tag{5.9}$$

In Equation (5.9) obtained from [27], basically the tip speed is varied until the equation is equal to zero, so autorotation exists. However, the induced velocity, v_i is also in this formula. But, the tip speed is also a variable for the induced velocity. This is the reason why the tip speed needs to be updated and the auto-rotation calculations need to be iterated. The equation for the induced velocity is given

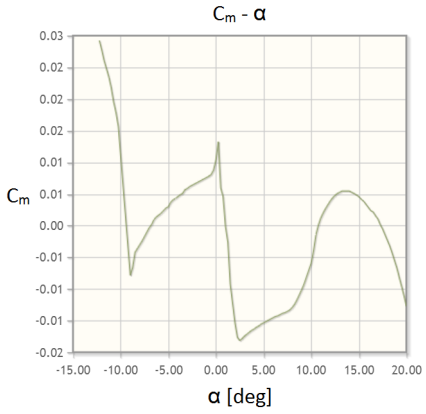

Figure 5.6: $C_{\mathrm{m}} - \alpha_{\mathrm{b}}$ curve for the NACA 8-H-12

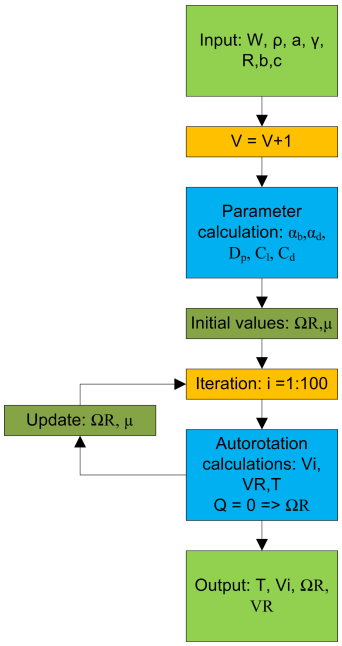

Figure 5.7: The outline of the auto-rotation calculations

in Equation (5.10). The iteration is done until the value for the tip speed and induced velocity remains constant for the same horizontal velocity.

$$v_i = v_0 \cdot \sin(\alpha_{\mathrm{d}}) - \frac{3}{4} \cdot \omega_{\mathrm{r}} \cdot \frac{C_d}{C_l}(1 + {\mu_{\mathrm{a}}}^2) \tag{5.10}$$

Equation (5.10) is also obtained from the condition that the net torque needs to be zero for autorotation. It is derived from Equation (5.11).

$$Q = 0 = \rho \cdot n_{\mathrm{blades}} \cdot c \cdot C_d \cdot {\omega_{\mathrm{r}}}^2 \cdot r^4 \frac{(1 + {\mu_{\mathrm{a}}}^2)}{8} - \rho \cdot {\omega_{\mathrm{r}}}^3 \cdot C_l \cdot \frac{n_{\mathrm{blades}} \cdot c}{6}(v_0 \cdot \sin(\alpha_{\mathrm{d}}) - v_i) \tag{5.11}$$

The advance ratio μ_{a}, which is also in the equation for the induced velocity is updated, because it is also depended on the tip speed. It is given in Equation (5.12)

$$\mu_{\mathrm{a}} = \frac{v_0 \cdot \cos(\alpha_{\mathrm{d}})}{\omega_{\mathrm{r}}} \tag{5.12}$$

The lift coefficient of the profile is calculated with the angle of attack of the blade, times the lift curve slope. This is only valid for a blade angle of attack from -8 to 10 [deg]. For the drag coefficient a seventh

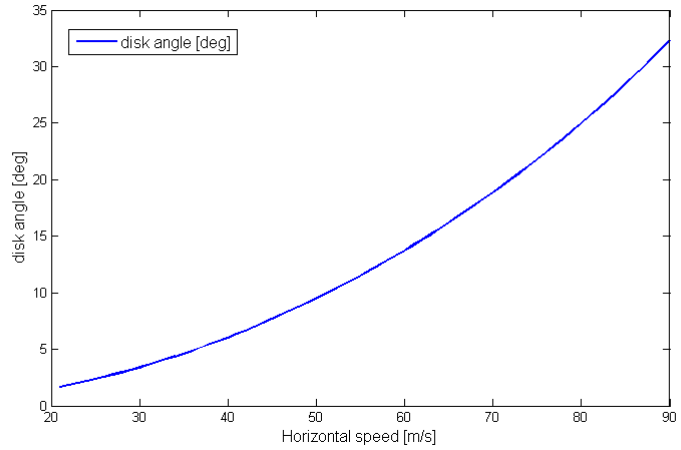

Figure 5.8: Disk angle versus horizontal speed

order polynomial is made which represents the $C_d - \alpha_b$ curve of the profile. From this the drag coefficient for the angle of attack of the blade is obtained. More information about the blade can be found in the section blade profile. From the induced velocity, the resultant velocity, V_{res} and the thrust, T_{rotor} can be calculated with Equations (5.13) and (5.14) respectively. The result for the thrust for the eGyro is given in Figure 5.11. There the thrust is given for a varying horizontal speed.

$$V_{res} = \sqrt{{v_0}^2 \cos(\alpha_d)^2 + (v_0 \sin(\alpha_d) - v_i)^2} \tag{5.13}$$

$$T_{rotor} = 2 \cdot \rho \cdot \pi \cdot r^2 \cdot V_{res} \cdot v_i \tag{5.14}$$

The most important output for the auto-rotation is the rotational speed for zero torque. The result of the tip speed for the eGyro is given in Figure 5.9. The tip speed is given for a varying horizontal speed. Also the maximum tip speed, as given in Equation (5.2), is displayed here. When the two lines cross, the maximum speed is reached. For the eGyro this is 227 [km/h]. For each horizontal speed, the required tip speed for auto-rotation is given.

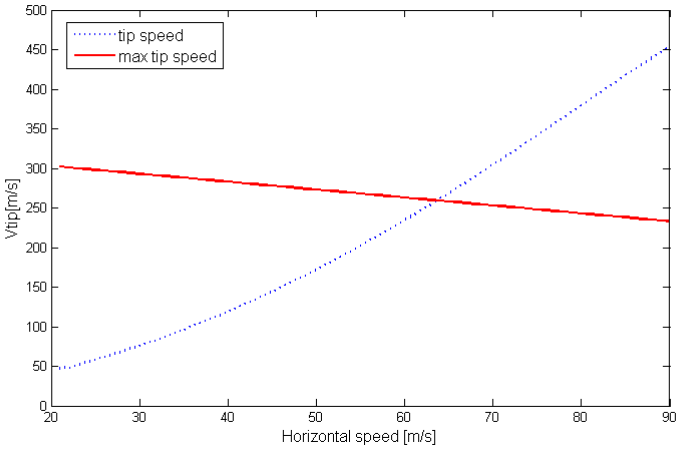

Figure 5.9: Tip speed for auto-rotation versus horizontal speed

5.3 Rotor Parameters

Now that the tip speed is known for the auto-rotation conditions, all other needed parameters which will also fulfill the auto-rotation conditions as well, since they are derived from the tip speed needed for auto-rotation.

5.3.1 Blade Angles

The inflow angle at the blade is the angle between the tangential and perpendicular inflow velocities on the blade. In this case, the tangential velocity equals the tip speed. The perpendicular velocity equals the induced velocity. Now the inflow angle is given in Equation (5.15).

$$\phi(i) = \arctan\left(\frac{U_\mathrm{p}}{U_\mathrm{t}}\right) \tag{5.15}$$

Where $\phi(i)$ is the inflow angle, U_p is the perpendicular inflow velocity and U_t the tangential inflow velocity. The method to determine the blade angles is obtained from [28].

As discussed before, the angle of attack is obtained from statistics. The only angle left is the pitch angle, θ_p. This angle is calculated with Equation (5.16).

$$\theta_\mathrm{p} = \alpha_\mathrm{b} - \phi(i) \tag{5.16}$$

The results obtained for this concept are shown in Figure 5.10. It can be noted that the angle of attack decreases when the horizontal speed increases and the inflow angle decreases. This is logical because those two angles depend on each other.

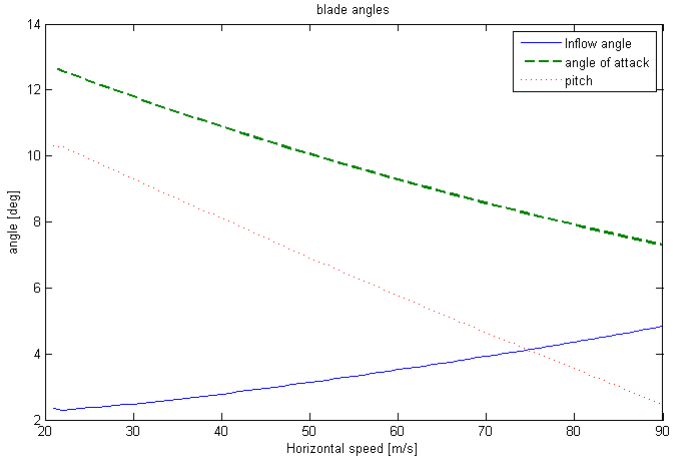

Figure 5.10: Blade angles versus horizontal speed

Flapping Angle

The flapping angle is calculated at trim conditions and for initial values. With the initial values it is meant that the thrust equals the weight and the vehicle is flying forward with a flight path angle equal to zero. The method to calculate the flight path angle is obtained from [29]. For the initial conditions, v_i is iterated making use of Equation (5.17). This equation is also obtained from Glauerts theory [30].

$$v_i = \frac{T_\mathrm{rotor}}{2 \cdot \rho \cdot r^2 \cdot V_\mathrm{res}} \tag{5.17}$$

The system of matrices given in Equation (5.18) gives the flapping angle and the pitch angle of attack of the blade.

$$\begin{pmatrix} 1 + \frac{3}{2}{\mu_\mathrm{a}}^2 & -\frac{8}{3}\mu_\mathrm{a} \\ -\mu_\mathrm{a} & \frac{2}{3} + {\mu_\mathrm{a}}^2 \end{pmatrix} \cdot \begin{pmatrix} \alpha_\mathrm{flapping1} \\ \theta_\mathrm{p0} \end{pmatrix} = \begin{pmatrix} -2{\mu_\mathrm{a}}^2 \frac{D}{MTOW} - 2\mu\lambda_i \\ \frac{4C_T}{\sigma C l_\alpha} + \mu\frac{D}{W} + \lambda_i \end{pmatrix} \tag{5.18}$$

Although, earlier a different method is used for the pitch angle, Equation (5.18) is used for the initial value for the pitch angle and of course as well for the flapping angle, $\alpha_{\text{flapping1}}$. $v_{\text{ind}i}$ is the dimensionless induced velocity which is given in Equation (5.19). D is the total drag and C_{T} the thrust coefficient as mentioned before. The flapping angle is determined to be 8.73 [deg]. The initial pitch angle is 18.71 [deg].

$$v_{\text{ind}i} = \frac{v_i}{\omega_{\text{r}}} \tag{5.19}$$

Maximum Angle Rotor

The maximum angle of the rotor depends on the minimum flying speed and the flapping angle. With minimum speed it is meant the lowest speed when the lift equals the weight. With high disk angles of attack, the lift will increase so the minimum speed is lower. The flapping angle is 8.73 [deg]. The clearance angle of the fuselage and the rotor is 18 [deg]. This means that the maximum disk angle of attack is 9.27 [deg]. With this maximum disk angle of attack, the minimum forward velocity is 140 $\left[\frac{\text{km}}{\text{h}}\right]$ at sea level.

5.4 Rotor Forces

There are different kinds of aerodynamic forces acting on the rotor, such as lift, induced drag and the profile drag. The method to calculate the forces is obtained from [28]. The lift L and induced drag D_{i} are simply components of the thrust force, T_{rotor}. Their equations are respectively Equation (5.20) and Equation (5.21).

$$L = T_{\text{rotor}} \cdot \cos(\alpha_{\text{d}}) \tag{5.20}$$

$$D_{\text{i}} = T_{\text{rotor}} \cdot \sin(\alpha_{\text{d}}) \tag{5.21}$$

The profile drag is calculated with Equation (5.22).

$$H_{\text{force}} = C_H \rho \pi R^2 (\Omega R)^2 \tag{5.22}$$

Where H is the profile drag and C_H is the H-force coefficient, also referred to as profile drag coefficient. This coefficient is calculated as given in Equation (5.23). Both the equation for the profile drag and its coefficient are obtained from [31].

$$C_{\text{H}} = \sigma \frac{C_d}{8} \left(2\mu_{\text{a}} + \frac{1}{2} {\mu_{\text{a}}}^3 \right) \tag{5.23}$$

The results of the lift, thrust and induced drag for varying horizontal speed are given in Figure 5.11. The lift may seem high, but it has to be noted that the disk plane angle of attack increases with the velocity. This is caused by the constant weight assumption and increasing drag with horizontal speed in Equation (5.8). When the disk angle of attack is 5 [deg], the lift will equal the MTOW at cruise speed. In reality, the disk plane angle of attack is a pilot input. It just has to be made sure that the required angle to generate enough lift is not too high.

The profile drag of the rotor is given in a separate plot because its magnitude is around three orders of magnitude smaller than the lift and the induced drag. As expected, it can be seen in Figure 5.12 that the profile drag increases with horizontal velocity and its magnitude is relatively low compared to the other drag forces.

5.5 Drag

In analyzing the aerodynamic performance of the vehicle the drag is of major importance and influences many different properties of the vehicle such as the angle of the disk plane during flight. The drag can be distinguished into parasite drag, induced drag and blade profile drag. The thrust yields most of the drag, but the rotor and fuselage drag contribute as well. To calculate the drag of the entire vehicle both the rotor and fuselage contribution must be taken into account. The total drag of the vehicle is calculated with the equation below:

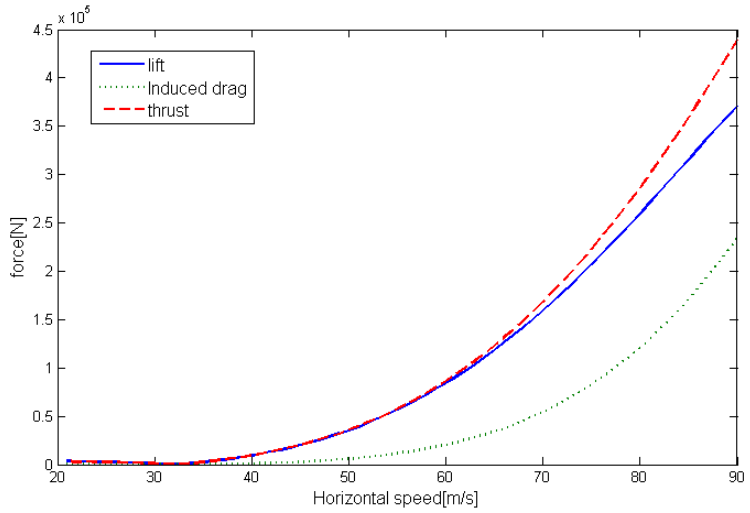

Figure 5.11: Thrust, lift and induced drag versus horizontal speed

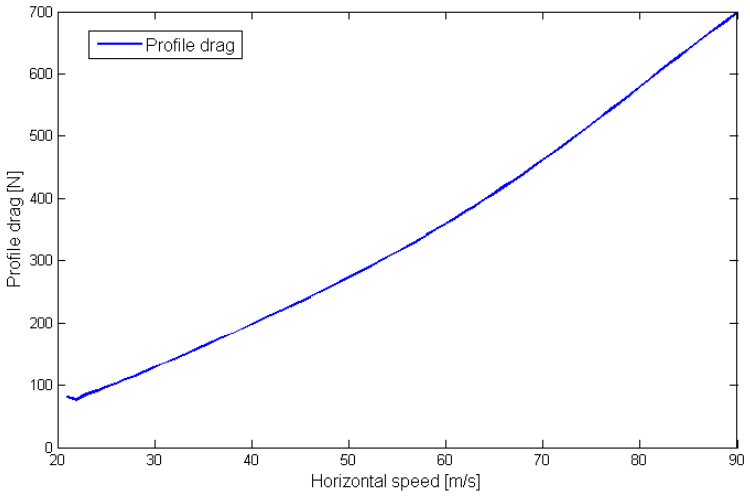

Figure 5.12: profile drag versus horizontal speed

$D = T_{\text{rotor}} \cdot \sin \alpha_{\text{b}} + H_{\text{force}} \cdot \cos \alpha_{\text{b}} + D_{\text{p}}$

The calculation of the induced drag and the H-force have been discussed in the previous section about auto-rotation. The parasite drag will be discussed in the next section and is mainly based on [20].

5.5.1 Parasite Drag

In calculating the total drag of the vehicle the parasitic drag should be taken into account having a considerable contribution. The parasite drag results from the interaction between the vehicle and the wind during flight and can be subdivided into streamline drag and bluff body drag. Bluff body drag means that the flow separates behind the body. In the latter form of drag the flow separates behind the body while the flow closes smoothly behind the body in the case of streamline drag. In this section an estimation is made for this drag based on statistical methods for helicopters [20]. Based on the frontal areas of different parts of the vehicle the drag coefficients are determined. The drag coefficients and areas for the different parts of the vehicle are multiplied with each other to yield the factor f as in Equation (5.24):

$$f = A \cdot C_d \tag{5.24}$$

In some cases a correction factor should be multiplied to f, which is the reason that f should be calculated separately for each part or combination of parts of the vehicle. The total drag of the vehicle is then given by Equation (5.25) below:

$$D = \frac{1}{2}\rho {v_0}^2 \sum_{i=1}^{n} f_{tot} \tag{5.25}$$

In (5.25) the factor f_{tot} is the sum of all factors of the different parts of the vehicle, as given in (5.26) below.

$$f_{tot} = f_F + f_{H+S} + f_{lg} + fHS + fVS \tag{5.26}$$

In this equation f_F, f_{H+S}, f_{lg}, f_{HS} and f_{VS} are the factors of the fuselage, hub and shaft, landing gear, horizontal and vertical stabilizer, respectively. These factors are outlined in the following sections. It should be noted that the determination of the drag is an estimation, partly based on reference data. It is not an accurate calculation of the exact parasite drag, since this would require an execution of detailed wind tunnel tests on a model of the vehicle. However, this estimation gives an acceptable indication of the magnitude of the parasite drag.

Fuselage Drag

The fuselage drag is a significant contribution to the parasite drag and is calculated in the same way as for a helicopter. The vehicle has a fuselage shape that is comparable to that of a helicopter, with some minor differences in shape and lay-out. It is assumed that the fuselage itself has a rectangular flat plate area in the front of the vehicle. The same holds for the front two ducted fans, which are attached to the fuselage. The total area corresponds to a certain drag coefficient which is obtained with the so called fineness ratio of the fuselage. The fineness ratio is defined in Equation 5.27.

$$f_{\text{fine}} = L_{\text{fuselage}}/d_f \tag{5.27}$$

In this equation L_{fuselage} represents the length of the fuselage in longitudinal direction and w_{fuselage} is the diameter of the circular cross section of the fuselage. From the graph in Figure 4.17 in [20], relating the fineness ratio to the drag coefficient, the drag coefficient for the fuselage is then determined. The same drag coefficient is assumed for the front two ducted fans. After that, the total fuselage drag is calculated through the well known relation in Equation (5.28).

$$D_{\text{fuselage}} = C_d \cdot \frac{1}{2}\rho {v_0}^2 A_{\text{frontal}} \tag{5.28}$$

In this equation the A_{frontal} is the frontal area of the fuselage, this area is determined assuming a rectangular area for the fuselage and ducted fans. This is shown in equation (5.29).

$$A_{\text{frontal}} = h_{\text{box}} \cdot w_{\text{fuselage}} + 2 \cdot h_{\text{fan}} \cdot 2 \cdot r_{\text{inlet}} \tag{5.29}$$

The total area of the fuselage including the ducted fans is then: $A_{\text{frontal}\,f} = 4.38$ [m^2]

In this equation h_{box} and w_{fuselage} represent the height and the width of the fuselage and h_{fan} and r_{inlet} represent the height and the width of the front two ducted fans. These shapes are not completely rectangular but this approximation is valid enough, since the shapes do not differ significantly. From reference data the drag coefficient that belongs to this frontal area for conventional helicopters is found to be $C_{dF} = 0.04$.

The product of the area and the drag coefficient of the fuselage is equal to $f_F = 0.1752$ [m^2]

Rotor Hub and Shaft

The rotor hub always causes flow separation because of its form and rotation. Therefore this drag is part of the vehicle's bluff body drag and can be minimized by using streamlined shapes for the rotor. The shaft yields less flow separation.

To calculate the drag that is caused by the rotor hub and the shaft the frontal areas of these parts of the vehicle are calculated first. The hub that is chosen for the design is comparable to the hub that is used in the Sikorsky H-34 helicopter, but with a smaller frontal area, that is equal to $A_{\text{frontal}\,H} = 0.5$ [m^2]. This hub has the ability to carry four blades and with the frontal area of this hub the drag coefficient

in non-rotating conditions is estimated from Table 4.2 in [20]. The drag ratio that relates the zero rpm drag coefficient to the full rpm drag coefficient is then read from Figure 4.22 in [20]. The drag coeffient at full rpm is then calculated with the equation:

$$C_{dH} = C_{d\mathrm{H,zeroRPM}} \cdot \mathrm{DR} \tag{5.30}$$

The final drag coefficient of the hub is then $C_{dH} = 0.4737$. The product of the frontal area and drag coefficient for the hub is then $f_S = 0.2368$ [m^2]. The shaft that is used is also comparable to the one used in the Sikorsky H-34 and has a diameter of $D_\mathrm{S} = 0.15$ [m] and a frontal area of $A_{\mathrm{frontal}S} = 0.1$ [m^2]. The drag coefficient is obtained from [20]. This graph relates the Reynolds Number to the drag coefficient of a circular cylinder. The Reynolds Number is calculated by the equation:

$$\mathrm{Re} = \frac{\rho \cdot v_0 \cdot D_\mathrm{S}}{\mu_\mathrm{a}} = 6400 \cdot v_0 \cdot D_\mathrm{S} \tag{5.31}$$

The drag coefficient is then determined from Figure 4.23 in [20] and corresponds to $C_{dS} = 0.3$. The product for the area of the shaft and its drag coefficient $f_S = 0.03$ [m^2]. The products of drag coefficient and area for both the hub and the shaft are added together to yield the total factor for the hub and the shaft together, as shown in (5.32).

$$f_{H+S} = f_H + f_S \tag{5.32}$$

This yields a total factor of $f_{H+S} = 0.2568$ [m^2].

The final step in calculating the final value for this factor is determining the hub gap to pylon width ratio. This value is taken from reference data for helicopters as $\frac{\text{Hub gap}}{\text{Pylon width}} = 0.3$. This yields a multiplication factor of 1.15 that has to be multiplied with f_{H+S} in order to arrive at the final value. Therefore this value is:

$f_{H+S} = 0.7472$ [m^2]

Landing Gear

The landing gear is another part of the vehicle that always yields flow separation because of its complex shape. The landing gear of the vehicle consists of wheels with struts which can very well be used to take shocks and drive from the landing site to the emergency site when needed. To reduce the drag fairings have been placed on the wheels, which produce a smooth outline. The frontal area of the landing gear is estimated to be $A_{\mathrm{frontal}lg} = 0.4$ [m^2] and from Figure 4.26 in [20] the drag coefficient of the wheels and struts is estimated from statistical data of faired wheels and is equal to $C_{dlg} = 0.36$. Since there are four wheels the final value of the drag coefficient multiplied by the areas is $f_{lg} = 0.5760$ [m^2].

Horizontal Stabilizer

The horizontal stabilizer is designed similar to the one used in an example helicopter in [20]. The airfoil used is the NACA-0012 and the area, span, mean aerodynamic chord and t/c ratio are determined. Calculating the Reynolds Number with Equation (5.31) again the zero lift drag coefficient is $C_{d0} = 0.01$ and is determined by Figure 4.15 in [20]. Estimating the lift coefficient from trim conditions and the span efficiency factor the induced drag coefficient can be calculated using equation:

$$C_{di} = \frac{C_{lH}(1+\delta)}{\pi AR} \tag{5.33}$$

With the thickness ratio of 12 % the junction drag coefficient is estimated from Figure 4.21 in [20] and with the aspect ratio and root thickness the equivalent junction drag coefficient is determined.

$$C_{dequiv} = 2\frac{C_{dj}(t^2)}{A_H} \tag{5.34}$$

The total drag coefficient for the horizontal tail is the sum of the drag coefficient mentioned above.

$$C_{dH} = C_{d0} + C_{di} + C_{dequiv} \tag{5.35}$$

The value for this drag coefficient is $C_{dH} = 0.0234$.

The horizontal tail has a dynamic pressure ratio compared to the rest of the vehicle $\frac{q_H}{q}$. This ratio is estimated to be 0.75 and should be taken into account when calculating the total drag of the vehicle. The area of the horizontal stabilizer is $S_{\text{h}} = 1.5$ [m^2] so the area/drag coefficient multiplication factor, taken into account the dynamic pressure ratio, is: $f_{HS} = 0.0263$. The tail dimensions are discussed in the stability and control chapter.

Vertical Stabilizer

The vertical stabilizer area is chosen to be similar to the one in the example helicopter described in [20]. The airfoil chosen for the vertical stabilizer is the same as the one for the horizontal stabilizer, the NACA 0012. The determination of its drag coefficient is similar to the determination for the horizontal stabilizer. Only the area is larger and the mean aerodynamic chord is longer. From Figure 4.15 in [20] the drag coefficient is determined. The dynamic pressure ratio is assumed the same as the one for the horizontal stabilizer, namely 0.75. Calculating the Reynolds Number with Equation (5.31) again, it can be seen in Figure 4.15 in [20] that the drag coefficient takes a value of $C_d = 0.010$. The drag coefficient/area factor is $f_{VS} = 0.0148$.

The final drag, calculated by Equation (5.25) takes the value $D = 3.06 \cdot 10^3$ [N] for cruise speed.

5.6 Results

In this section the main results for the initial conditions of the aerodynamics section are given. The results are all obtained for cruise speed, which is 200 $\left[\frac{\text{km}}{\text{h}}\right]$ and under the condition that the lift equals the weight. For a good overview, the results are listed in Table 5.3. Some of these values will change throughout the mission, such as the drag values. Other however will remain constant, such as the number of blades and the chord.

Table 5.3: aerodynamic results for initial conditions

Parameter	**Value**	
Flapping angle	8.72	[deg]
Initial pitch angle	18.71	[deg]
Max disk angle of attack	9.27	[deg]
Max forward velocity	227	$\left[\frac{\text{km}}{\text{h}}\right]$
Number of blades	4	[-]
Chord	0.28	[m]
Radius	4.24	[m]
Solidity ratio	0.0841	[-]
Aspect ratio	15.14	[-]
Disk loading	32.76	$\left[\frac{\text{kg}}{\text{m}^2}\right]$
Profile	NACA 8-H-12	
Parasite drag	$3.06 \cdot 10^3$	[N]
Profile drag	314.5	[N]
Induced drag	$1.53 \cdot 10^3$	[N]
Disk angle of attack	5	[deg]
Blade angle of attack	9.62	[deg]

6 Stability and Controllability

For the vehicle to be designed several stability characteristics are investigated. First of all, static stability is investigated. An aircraft is defined to be statically stable if it tends to return towards its trim flight condition following any external disturbance. For static stability, the center of gravity location is determined for several flight cases as well as different trim conditions during cruise flight at cruise speeds. Other center of gravity criteria are investigated including the shift during flight and general variation for different loading configurations of the vehicle.

The dynamic stability predicts how the response of the vehicle will propagate over time after a disturbance occurred. Statically stable but dynamically unstable vehicles show divergent oscillatory behavior when returning to a trim state. Dynamically stable vehicles will display convergent oscillatory motions which are damped around the trim state. For the eGyro a three degree of freedom model was established predicting the dynamical response of the vehicle for different disturbances in Section 6.5.

6.1 Center of Gravity Analysis

The center of gravity of the aircraft is an important parameter in the stability and control analysis. During both cruise and VTOL the center of gravity determines whether the vehicle is stable and controllable. Therefore, in this section the center of gravity is analyzed.

6.1.1 Center of Gravity During Cruise

During cruise the position of the center of gravity in absolute sense does not matter. However, as is found in [32] and in conversations with designers at PAL-V, an auto-gyro will be stable if the thrust line acts behind the center of gravity as it will then induce a pitch down moment when the angle of attack increases. This angle, shown as β in Figure 6.1, is determined from Chapter 5 to be 3.7 [deg] in cruise at MTOW. Futhermore, a clearance angle α in Figure 6.1 is required such that the rotor will not crash into the fuselage. This angle is determined to never exceed 10 [deg]. Together, these two conditions deliver the following system of Equations (6.1):

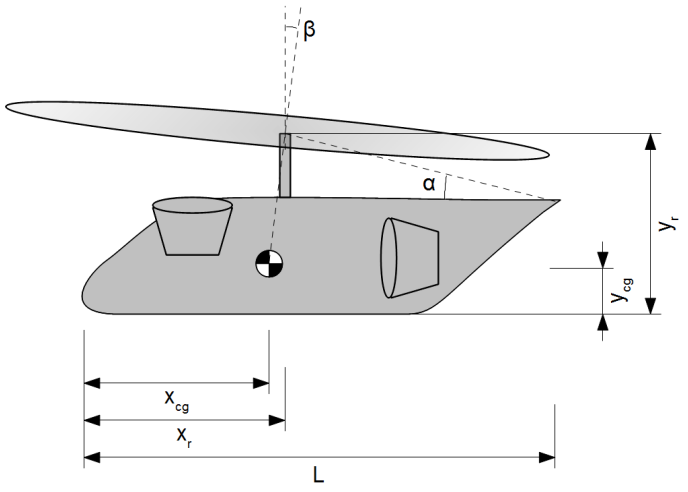

Figure 6.1: Hub and clearance angles of the rotor

$$\begin{cases} \tan\beta_{\mathrm{r}} = \dfrac{x_{\mathrm{r}} - x_{\mathrm{cg}}}{y_{\mathrm{r}} - y_{\mathrm{cg}}} \\ \tan\alpha_{\mathrm{r}} = \dfrac{y_{\mathrm{r}} - 1.7}{6 - x_{\mathrm{r}}} \end{cases} \tag{6.1}$$

This results in the following Equations (6.2) for x_{r} and y_{r}:

$$\begin{cases} x_{\mathrm{r}} = \dfrac{6\tan\alpha\tan\beta + 1.7\tan\beta - y_{\mathrm{cg}}\tan\beta + x_{\mathrm{cg}}}{1 + \tan\alpha\tan\beta} \\ y_{\mathrm{r}} = (6 - x_{\mathrm{r}})\tan\alpha + 1.7 \end{cases} \tag{6.2}$$

The aircraft will then be stable at all times during cruise, which will be shown in Section 6.2 about longitudinal static stability.

6.1.2 Center of Gravity During VTOL

During VTOL the equilibrium of forces is less complicated than during cruise. The only forces acting are the weight and the thrusts produced by the two ducted fans as shown in Figure 6.2.

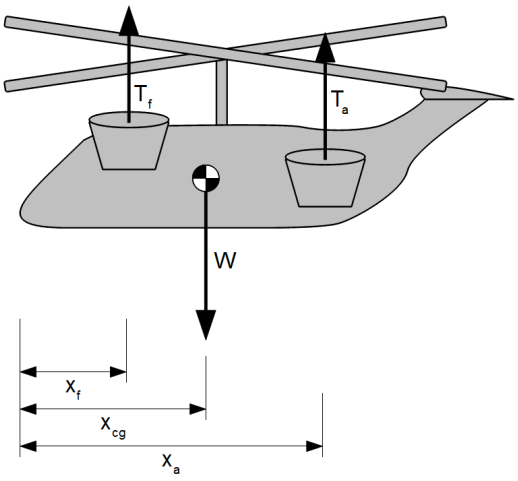

Figure 6.2: Forces acting on the vehicle during VTOL

Using this figure, taking moments about the center of gravity, which should be zero to be stable, Equation (6.3) is obtained:

$$\sum M_{\mathrm{cg}} = T_{\mathrm{a}}(x_{\mathrm{a}} - x_{\mathrm{cg}}) - T_{\mathrm{f}}(x_{\mathrm{cg}} - x_{\mathrm{f}}) = 0 \tag{6.3}$$

Hence, the center of gravity is found in Equation (6.4):

$$x_{\mathrm{cg}} = \frac{T_{\mathrm{f}}x_{\mathrm{f}} + T_{\mathrm{a}}x_{\mathrm{a}}}{T_{\mathrm{f}} + T_{\mathrm{a}}} \tag{6.4}$$

The critical case turns out to be when maximum thrust is delivered. The maximum thrust is required when the fully loaded vehicle with a weight of $W = \mathrm{MTOW}g_0 = 1850$ [kg] $= 18,149$ [N] is lifted at a RoC of 5 $\left[\frac{\mathrm{m}}{\mathrm{s}}\right]$. The ducted fans are designed to deliver this amount of thrust at full power. This means that in this situation the forces should be balanced so that no moment exists and the vehicle is stable. In all other cases, either the weight or the RoC is less such that there is power left to balance the forces and stabilize the vehicle. Therefore the critical case of take-off at MTOW and maximum RoC is analyzed here.

6.1.3 Center of Gravity Determination

To determine the location of the center of gravity Equation (6.4) is used.

At maximum power the thrust delivered by the ducted fans is known to be $T_f = 4429$ [N] per fan for the front two fans and $T_a = 5454$ [N] for the aft two as found in Section 4.1.

The remaining three parameters in the equation require an iterative process to determine x_{cg}, as this value is dependent on the location of the ducted fans as well. Therefore, the determination of the location of center of gravity is done using different system groups.

Center of Gravity of Fixed Systems

The location, and therefore center of gravity, of a lot of systems in the aircraft is fixed relative to the fuselage lay-out. For instance, the location of the cockpit instruments is fixed and does not depend on the location of the center of gravity. All these systems, their weights and their moment about the nose of the aircraft are shown in Table 6.1 and these are shown in a side view drawing of the aircraft in blue in Figure 6.3.

Table 6.1: Center of gravity determination of fixed systems

Component	Subcomponent	Weight [kg]	Location x [m]	Location y [m]	Moment x [kg · m]	Moment y [kg · m]
Power train	Engine	132	1.8	1.8	237.6	237.6
	Generator	71.3	2.5	1.8	178.3	128.3
	Motors front	31.7	1.4	1.5	44.4	47.6
	Extra	10	2.2	1.8	22	18
Ducted fans	Ducted fans front	30	1.4	1.5	42	45
Fuselage	Fuselage	100	2.2	0.9	220	90
Equipment	Avionics	22.7	0.5	0.2	11.3	4.5
	Controls	7.2	1	0.6	7.2	4.3
	Furnishing & equipment	14	1.5	0.6	21	8.4
	Instruments	8.2	0.8	0.6	6.5	4.9
Crew & payload	Pilot	80	1.6	0.6	128	48
	Copilot	80	1.6	0.6	128	48
	Payload	400	3	0.8	1200	320
Other	Landing gear	95	2.5	–0.4	237.5	–38
	Airco & anti-ice	13	2.5	1.5	32.5	19.5
	Manufacturing variation	6.4	2.5	0.9	16	5.8
Total		**1101.5**			**2532.3**	**991.9**

Center of Gravity of Variable Systems

Apart from the fixed systems shown in the previous section, four systems are not fixed. These are the rotor, fuel tanks, battery packages and aft ducted fans.

The rotor and fuel tanks are positioned relative to the center of gravity.

The determination of the location of the rotor is explained in Section 6.1.1 about cruise stability.

The fuel tank is positioned at the same location as the center of gravity such that the center of gravity will not shift during the mission when the vehicle is fully loaded.

The battery package can be situated everywhere in the floor or roof as long as it does not obstruct the fuel tanks and is used to balance the aircraft. It is chosen to be located below the floor since there is enough space and the batteries are easy replaceable and accessible from the bottom of the vehicle. The aft ducted fans have a horizontal range limited by the location and size of the loading doors and influence the center of gravity as is shown in Equation (6.4).

The locations of these systems are summarized in Table 6.2.

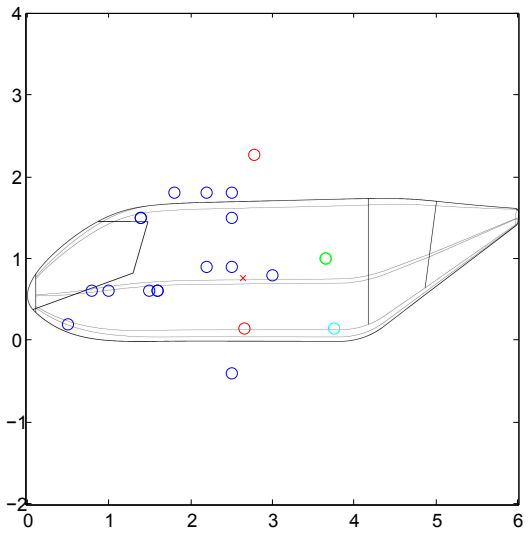

Figure 6.3: Center of gravity of subsystems and vehicle

Table 6.2: Center of gravity determination of variable systems

Component	Subcomponent	Weight [kg]	Location x [m]	Location y [m]	Moment x [kg · m]	Moment y [kg · m]
Power train	Batteries	257.1	$1.25 \leq x_{\text{batt}} \leq 5.75$	0.15 or 1.5	$257.1x_{\text{batt}}$	38.6 or 385.7
	Fuel	311.5	x_{cg}	0.15	$311.5x_{\text{cg}}$	46.7
	Motors aft	43.4	$3.5 \leq x_{\text{a}} \leq 5.75$	1	$43.4x_{\text{a}}$	43.4
Ducted fans	Rotor & hub	120	See Eq. (6.2)	See Eq. (6.2)	$120x_{\text{r}}$	$120y_{\text{r}}$
	Ducted fans aft	40	x_{a}	1	$40x_{\text{a}}$	40
Total		**772**				**516.7 or 863.8**

Center of Gravity MATLAB Iteration

To finally determine the location of the center of gravity a MATLAB script is made implementing all data shown before.

In this script first all constants are initialized. Then a loop is started that determines the location of the aft ducted fan x_{a} between 3.5 [m] and 5.75 [m] as shown before. Using this value, the location of zero moment due to the ducted fan thrust, which must be at the center of gravity x_{cg}, can be calculated using Equation (6.4). Then the location of the rotor can be calculated using Equation (6.2).

Using these parameters, the moment contribution of the fuel, aft motors, aft ducted fans, rotor and hub can be calculated. Then it is checked if the position of the fuel in the floor is physically possible before entering the second loop, which loops over the possible positions of the batteries x_{batt}.

Now, some last checks are done, such as the distance between fuel and batteries. Then the moment contribution of the batteries can be calculated. All moment contributions are then summed and divided by the weight so that the actual center of gravity is found. If this center of gravity is within 1 % of the location of zero moment the configuration is considered feasible and safe. Finally all feasible configurations are plotted as shown in Figure 6.4 and one is chosen, shown with a black vertical line.

The configuration that is chosen is the one with the batteries as far aft in the floor as possible – which is at 3.75 [m] – such that these are easily accessible while keeping the aft ducted fan as far aft that enough room for the loading door is created.

The center of gravity contribution due to the variable systems for this configuration is shown in Ta-

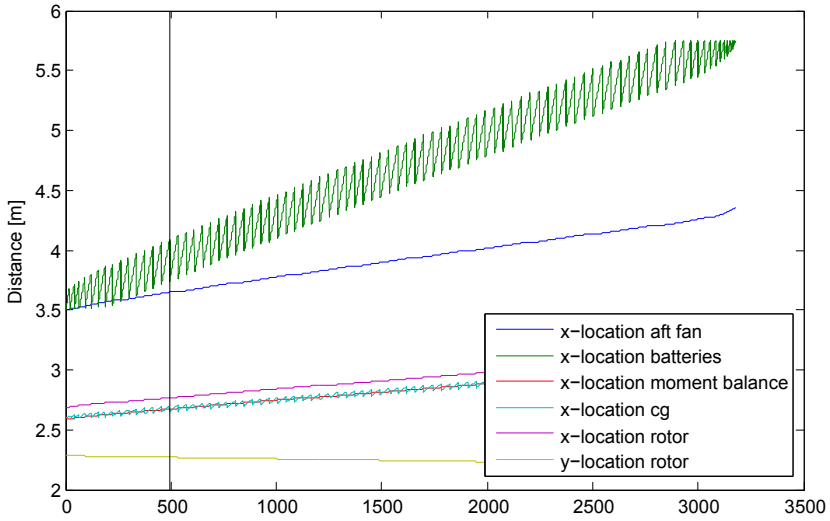

Figure 6.4: Feasible stability configurations, chosen configuration indicated with black vertical line

ble 6.3. This is shown visually in Figure 6.3 with red, green and blue dots.

Table 6.3: Center of gravity determination of variable systems for the chosen configuration

Component	Subcomponent	Weight [kg]	Location x [m]	Location y [m]	Moment x [kg · m]	Moment y [kg · m]
Power train	Batteries	257.1	3.75	0.15	964.1	38.6
	Fuel	311.5	2.65	0.15	825.5	46.7
	Motors aft	43.4	3.65	1	158.4	43.4
Ducted fans	Rotor & hub	120	2.77	2.27	332.4	272.4
	Ducted fans aft	40	3.65	1	146	40
Total		**772**			**2450.2**	**509.5**

Finally, the location of the center of gravity can then be calculated by summing all moments and dividing it by the sum of all weights. For the chosen configuration these are $x_{cg} = 2.65$ [m] and $y_{cg} = 0.76$ [m], which is also shown with a red cross in Figure 6.3.

6.1.4 Center of Gravity Shift

Another important parameter to consider is the center of gravity shift. The location of the center of gravity as calculated before is the most aft possible position of the center of gravity, as the vehicle will otherwise not be stable as explained in Section 6.1.1. However, the center of gravity is allowed to move forward.

The only systems that can change weight are the payload/crew and the fuel. As the payload is located after the center of gravity, it will move the center of gravity forward, so this is no problem. The fuel is located at the center of gravity, so this will also not be a problem. However, as the copilot is located in front of the center of gravity a problem occurs. As the copilot is removed and the payload kept in place, the location of the center of gravity will be $x_{cg} = 2.69$ [m]. However, it is found that with a payload weight of 190 [kg] the center of gravity is back at 2.65 [m] again. So, a copilot is needed if the payload is larger than 190 [kg], or a thorough balancing of the payload is needed (should be moved backward).

When the copilot is present and no payload and fuel is present the center of gravity is located at 2.59

[m], which is the most forward position in all configurations. In the same condition, the height of the center of gravity is 0.94 [m], which turns out to be the maximum value as well.

6.2 Static Stability Analysis

As can be found in [33] the longitudinal static stability of an aircraft is determined by a very simple criterion, shown in Equation (6.5):

$$\frac{dC_{\mathrm{m}}}{d\alpha} = C_{m_\alpha} < 0 \quad \text{at} \quad C_m = 0 \tag{6.5}$$

Here, $d\alpha$ is the change in angle of attack with respect to the trim position.

So, to determine this longitudinal stability, all moments acting on the aircraft as a function of angle of attack α have to be determined. The forces and moments acting on the aircraft are shown in Figure 6.5.

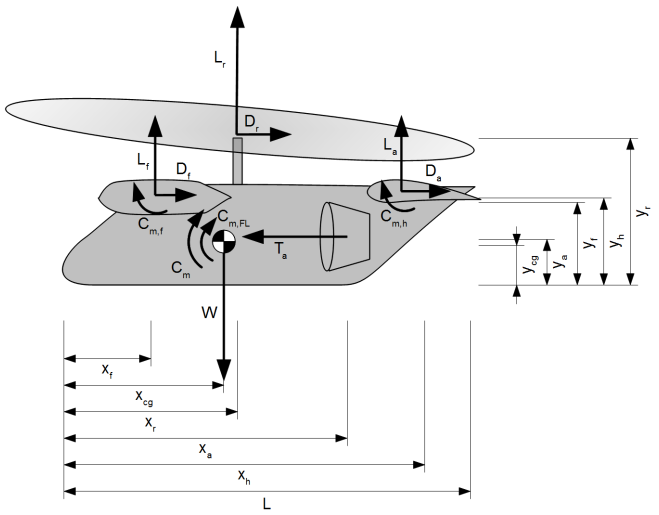

Figure 6.5: Forces and moments acting on the aircraft during cruise. C_m is the sum of all the moments around the center of gravity.

A MATLAB script is created to determine the relation between the angle of attack and the moments. To do this, a trim condition is defined first. For this condition, the moments are calculated as shown later on so that the required angle of attack of the horizontal tailplane can be determined. As this tailplane is used as trimming device but not as elevator, this angle of attack with respect to the fuselage (α_h) is considered constant during disturbances.

After this trim condition is defined, the angle of attack is varied between -10 and 10 [deg]. For each of this angles the moments and forces are determined as explained shortly hereafter.

Fuselage Moment M_{FL} The fuselage moment is determined using statistical data from [34] and is determined to be $C_{m,\mathrm{FL}} = C_{m,0} + C_{m_{\alpha,\mathrm{FL}}}\alpha$ with $C_{m,\mathrm{FL}} = -0.01$ and $C_{m_{\alpha,\mathrm{FL}}} = 0.0012$. The fuselage moment equals then to Equation (6.6):

$$M_{\mathrm{FL}} = \frac{1}{2}\rho V^2 S_p C_{m,\mathrm{FL}} \tag{6.6}$$

Fan Moment M_{a} The fan moment depends on the thrust delivered by each ducted fan, which is $T_{\mathrm{a}} = \frac{1}{2}\frac{W}{L/D}$. As can be seen from Figure 6.5 the moment per fan then becomes (Equation (6.7))

$$M_{\mathrm{a}} = -T_{\mathrm{a}}(y_{\mathrm{a}} - y_{\mathrm{cg}}) \tag{6.7}$$

Front Fan Fairing Moment M_f Using XFLR5 [35] the C_L–α, C_D–α and C_M–α curves of the fairing are found. Using this data, $C_{L,\mathrm{f}}$, $C_{D,\mathrm{f}}$ and $C_{M,\mathrm{f}}$ can be found at the current angle of attack, and the forces and moment are then found using $X_\mathrm{f} = \frac{1}{2}\rho V^2 S_\mathrm{f} C_{X,\mathrm{f}}$ for $X = L, D, M$. The moment of the fairing then equals to Equation (6.8):

$$M_\mathrm{f} = L_\mathrm{f}(x_\mathrm{cg} - x_\mathrm{f}) + D_\mathrm{f}(y_\mathrm{f} - y_\mathrm{cg}) + M_\mathrm{f} \tag{6.8}$$

Rotor Moment M_r Using the data from Chapter 5 the lift and drag of the rotor are obtained. The moment due to the rotor is then found with Equation (6.9).

$$M_\mathrm{r} = -L_\mathrm{r}(x_\mathrm{r} - x_\mathrm{cg}) + D_\mathrm{r}(y_\mathrm{r} - y_\mathrm{cg}) \tag{6.9}$$

Horizontal Tail Moment M_h The moment of the horizontal tail is determined in the same way as the fairing moment, using curves from XFLR5. However, not the disturbance angle α is used to lookup the coefficients, but the sum of the trim angle and the disturbance angel $\alpha_h + \alpha$. As shown L_h, D_h and M_h are then found. The final total tail moment is shown in Equation (6.10).

$$M_\mathrm{h} = -L_\mathrm{h}(x_\mathrm{h} - x_\mathrm{cg}) + D_\mathrm{h}(x_\mathrm{h} - y_\mathrm{cg}) + M_\mathrm{h} \tag{6.10}$$

By summing and saving all these moments at different angles of attack, the relation between the pitching moment and angle of attack can be plotted as shown in Figure 6.6.

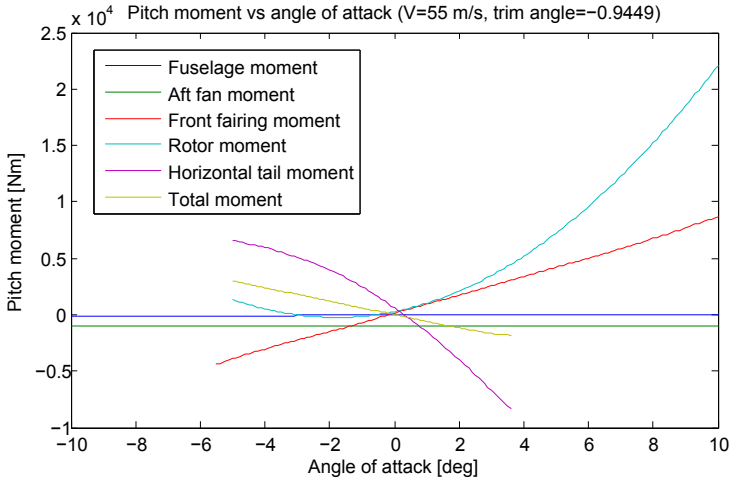

Figure 6.6: Angle of attack versus pitching moment at trim around trim condition during cruise at maximum loading

In Figures 6.6 and 6.7 the total moment is shown, but as this is just the moment coefficient multiplied with a constant, the graphs for the pitch moment coefficient will look exactly the same. As can be seen, the total moment line is descending, so the condition from Equation (6.5) is satisfied in the whole center of gravity range as explained in Section 6.1.4.

In Figures 6.6 and 6.7 also the trim angle of the horizontal stabilizer is shown to acquire a stable flight. As can be seen, trim condition can be reached with relative small trim angles, so low drag, which is what is desired.

6.3 Vertical Tail Dimensioning

As only a longitudinal three degrees of freedom model is created, analysis of the vertical stabilizers based on actual vehicle data is impossible. Therefore, to dimension the vertical stabilizer, analytical data from [36] is used. Of course, note has to be taken that this is fixed wing data. However, as vertical stabilizers are not necessary for helicopters, whilst they are essential in gyroplanes, this fixed aircraft method is used. Since rudders are placed on the vertical tailplane their effectiveness is increased if they are placed in the high velocity stream from the ducted fans. When a H-tail configuration is used, this is the case and

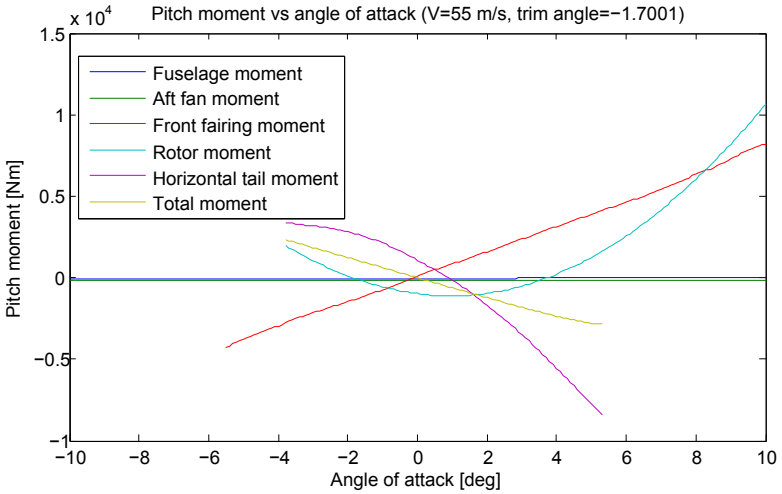

Figure 6.7: Angle of attack versus pitching moment at trim around trim condition during cruise at minimum loading

the tail can be placed relatively low, to have a larger spacing between the rotor and the tail. In Figure 6.8 a relation between the MTOW and vertical stabilizer surface area is derived based on statistical data. Using this data, the total surface area is found to be $S_v = 1.9734$ [m^2], or 0.99 [m^2] per vertical tailplane. The final lay-out can be seen in Figure 3.1.

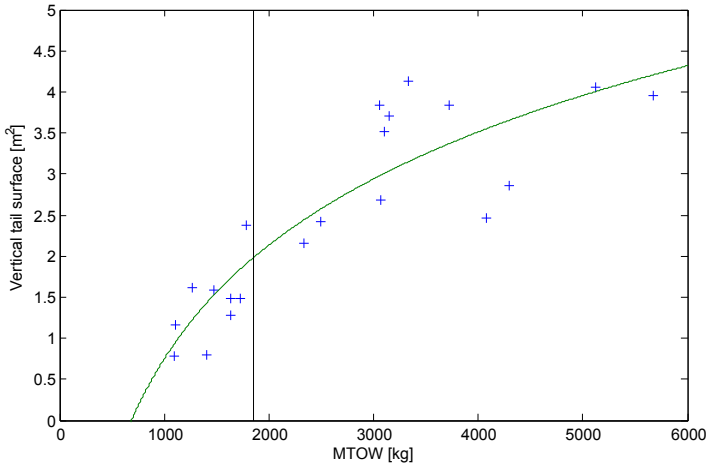

Figure 6.8: Relation between MTOW and vertical tail surface area. eGyro case indicated with a black line.

6.4 Trim for Different Cruise Speeds

For different air speeds the aircraft has to be trimmed to perform steady symmetrical cruise flight. For the eGyro this is done by varying two different control variables; the rotor disk angle θ_c and the trim angle of the horizontal tail α_{trim}. Thrust of the aft ducted fans is set in such a way that the cruise speed v_0 and lift are maintained.

A MATLAB script is created to obtain different trim deflections for different cruise speeds. The script uses another MATLAB script created to compute the static stability (Section 6.2), in which all the forces and moments are computed that act on the vehicle.

The general algorithm is to vary θ_c until all accelerations on the vehicle are equal to zero. Rotor characteristics are computed using the same method as in Section 5.3. Afterwards another loop ensures

that the pitching moment M_{pitch} acting on the vehicle is zero by varying α_{trim}. This change in α_{trim} changes the vertical force balance which brings the algorithm back to the first step. This process converges to a point where both the pitching moment and vertical force are zero.

Trim angles of θ_{c} and α_{trim} for different cruise speeds are displayed in Figure 6.9 and Figure 6.10.

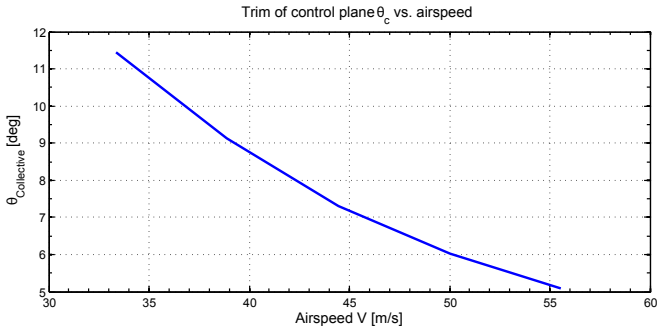

Figure 6.9: Control plane pitch angle θ_{c} vs. Airspeed

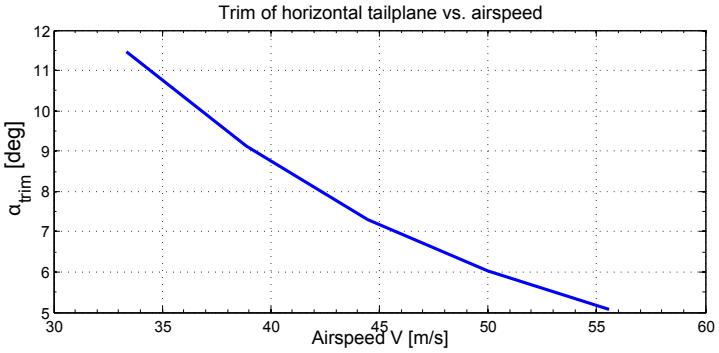

Figure 6.10: Horizontal tailplane trim angle α_{trim} vs. Airspeed

6.5 Dynamic Stability

Static stability of an aircraft concerns the direction of motion of the vehicle due to a perturbation. Dynamic stability determines the reaction of the vehicle over a time span. An aircraft is said to be dynamically stable if, after a disturbance, it returns to its initial trim condition and the following oscillation damps out [33].

To asses dynamical behavior the eigenmotions of the vehicle have to be determined. Eigenmodes can be excited by any disturbance, such as a gust or a control input. Symmetrical eigenmodes display the response of the vehicle to a perturbation in the plane of symmetry (longitudinal direction) and assymetrical eigenmodes display the response of the vehicle in lateral directions. For the longitudinal eigenmodes the phugoid and short period oscillation are going to be analyzed. Lateral eigenmodes, such as the dutch roll (lateral phugoid) and spiral motion, will be discussed, but not analyzed.

6.5.1 Longitudinal Eigenmotions

A convenient first estimate for the response of the longitudinal eigenmotions of any aircraft can be provided with a linearized state-space system [33]. Such a system is based on stability derivatives which state the vehicle response for different control inputs and state variables. For rotorcraft the linearized

system is as displayed in Equation 6.11 below [37].

$$\begin{Bmatrix} \Delta\dot{u} \\ \Delta\dot{w} \\ \Delta\dot{\theta_f} \\ \Delta\dot{q} \end{Bmatrix} = \frac{1}{m} \begin{bmatrix} X_u & X_w & X_{theta_f} - g \cdot m\cos\theta_{f_0} & X_q - w_0 \cdot m \\ Z_u & Z_w & Z_{theta_f} - g \cdot m\sin\theta_{f_0} & Z_q \\ 0 & 0 & 0 & 1 \\ \frac{M_u \cdot m}{I_y} & \frac{M_w \cdot m}{I_y} & \frac{M_{\theta_f} \cdot m}{I_y} & \frac{M_q \cdot m}{I_y} \end{bmatrix} \begin{Bmatrix} \Delta u \\ \Delta w \\ \Delta\theta_f \\ \Delta q \end{Bmatrix} + \begin{bmatrix} X_{\theta_0} & X_{\theta_c} \\ Z_{\theta_0} & Z_{\theta_c} \\ 0 & 0 \\ M_{\theta_0} & M_{\theta_c} \end{bmatrix} \begin{Bmatrix} \Delta\theta_0 \\ \Delta\theta_c \end{Bmatrix} \tag{6.11}$$

In this linearized system for helicopters, the accelerations of the vehicle $\dot{u}$, $\dot{w}$, $\dot{\theta}_\mathrm{f}$ and $\dot{q}$ are computed as a linear function of the stability derivative matrix multiplied with the state variable vector and the matrix vector multiplication of the control derivative matrix with the control input vector. The state variables are u, w, θ_f and the $\dot{\theta}_\mathrm{f}$. The control variables are the collective pitch and the θ_c.

To use a linearized system as described in Equation 6.11 the stability derivatives of the vehicle that are analyzed have to be known. As the eGyro is a unconventional vehicle it is not able to use statistical methods to come up with the stability and control derivatives to use in a linearized system. The choice was thus made to construct a three degrees of freedom model, based on aerodynamic properties unique for the eGyro concept.

6.5.2 Longitudinal Three Degree of Freedom Model

For the eGyro a longitudinal three degree of freedom model is created. This has two interesting purposes. First of all the vehicle response can be computed for different flight conditions and disturbances. Second, it enables computation of stability derivatives which can be used for the linearized system.

General Layout In general the simulation scheme is based on the three degrees of freedom outline provided in [38]. The three degree of freedom model constructed for the eGyro uses a comparable algorithm. It has to be noted that the model holds for a free, uncontrolled motion, this means that $\Delta\theta_\mathrm{c} = 0$, meaning that the cyclic control is fixed at a trim angle.

Summarized, for each time instant the model computes the free stream properties, with which it calculates the rotor thrust and lift. Then the aerodynamic moment and force of each subcomponent (fan fairings, fuselage, tailplane etc.) are computed. With these numbers available the vehicle accelerations and pitch rate acceleration can be obtained. These are then used to determine the velocity and pitch rate of the vehicle, which is followed by a computation of the position and pitch. Then the process iterates again with computing the airflow for the following time instant. A block diagram of the model can be found in Figure 6.11. Each block is elaborated on in more detail.

Trim of the Vehicle First a user input for v_0 is required before the computational hold is asked. By default this is 200 $\left[\frac{\mathrm{km}}{\mathrm{h}}\right]$ and the model produces the most valid results for this speed, because the thrust magnitude is fixed. The algorithm to compute the trim deflections is given in Section 6.4.

Main User Input With θ_c and α_trim known, the t_{end} and t_step of the simulation can be specified. It has to be noted that the model provides unsatisfactory oscillatory behavior for a t_step larger than 0.01 [s]. The user can provide disturbance inputs which will be applied in the 10th iteration of the program loop. This is to ensure that a change in the default flight condition is clearly noticeable. By default these are zero. Input disturbances include: $\Delta\ \alpha$, $\Delta\ \theta_\mathrm{f}$, $\Delta\ q$, $\Delta\ u$ and $\Delta\ w$.

Stream Properties The α is computed with Equation 6.12.

$$\alpha = \frac{w}{u}; \tag{6.12}$$

The v_inf is computed by adding vectors u and w which is displayed below in Equation 6.13.

$$v_\mathrm{inf} = \sqrt{w^2 + u^2}; \tag{6.13}$$

Also the α_f and the α_c are determined and displayed in Equation 6.14 and 6.15

$$\alpha_\mathrm{f} = \theta_\mathrm{f} - \alpha \tag{6.14}$$

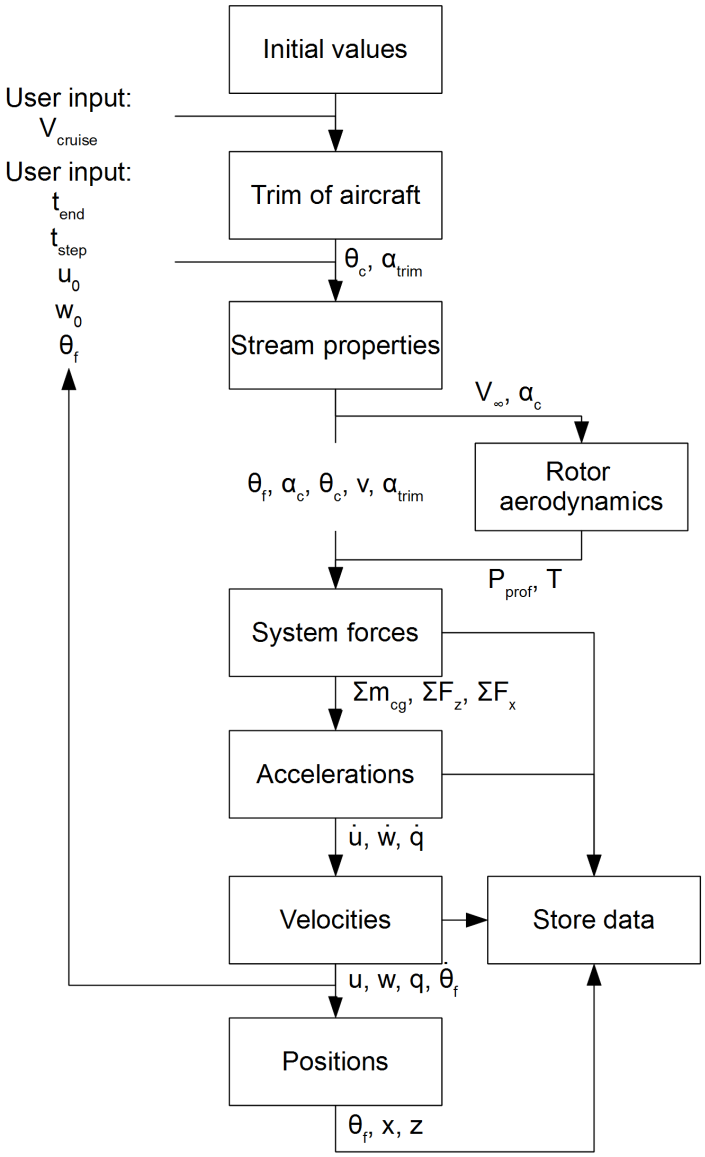

Figure 6.11: Block diagram of the 3 degree of freedom model

$$\alpha_{\mathrm{f}} = \theta_{\mathrm{c}} - \alpha \tag{6.15}$$

Rotor Aerodynamics Using the script introduced in section 5.3 T_{rotor} perpendicular to θ_{c} and D_{profile} parallel to θ_{c} can be computed for a given v_{inf} and α_{c}. The algorithm is slightly different than provided in Figure 5.7 in section 5.3 as the v_{inf} and α_{c} are already provided. In summary the applied theory is Glauert's rotary wing theory with axis torque set to zero for auto-rotation [20].

System Forces With the rotor T_{rotor} and D_{profile} known, the system total forces can be computed as explained in 6.2. All moments and forces acting on the vehicle in longitudinal cruise flight are displayed in figure 6.5. Furthermore, all relevant angles, velocities, accelerations and pith rates are displayed with sign convention in figure 6.12.

With an input of T_{rotor}, D_{profile}, α_{f}, v_{inf}, θ_{f} and α_{trim} a function script returns the $\sum F_{\mathrm{x}}$ and $\sum F_{\mathrm{z}}$ in the earth frame. The $\sum M_{\mathrm{cg}}$ is also given.

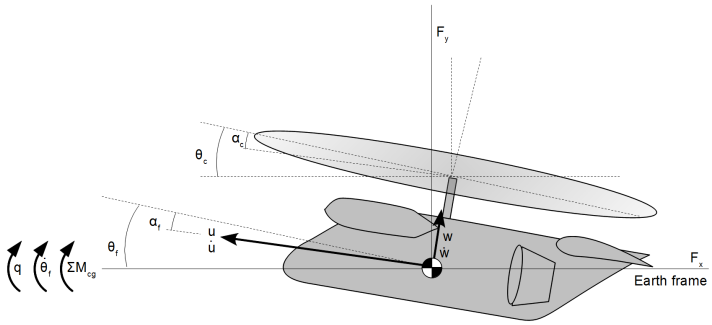

Figure 6.12: Summary of vehicle angles and motion directions.

System forces Using $\sum F_{\mathrm{x}}$, $\sum F_{\mathrm{z}}$ and $\sum M_{\mathrm{cg}}$ the vehicle accelerations can be computed. The acceleration parallel to the vehicle frame can be computed with Equation 6.16

$$\dot{u} = \frac{\sum F_{\mathrm{x}} \cos\theta_{\mathrm{f}} + \sum F_{\mathrm{z}} \sin\theta_{\mathrm{f}}}{\mathrm{MTOW}} - q \cdot w \tag{6.16}$$

Accelerations and velocities The acceleration perpendicular to the vehicle frame can be computed with Equation 6.17.

$$\dot{w} = \frac{-\sum F_{\mathrm{x}} \sin\theta_{\mathrm{f}} + \sum F_{\mathrm{z}} \cos\theta_{\mathrm{f}}}{\mathrm{MTOW}} + q \cdot u \tag{6.17}$$

The $\dot{q}$ is computed with Equation 6.18.

$$\dot{q} = \frac{\sum M_{\mathrm{cg}}}{I_{\mathrm{yy}}} \tag{6.18}$$

With the accelerations in the vehicle frame available the changes in u, w and q are simply computed, by adding the previous known speed and the current acceleration. An example is displayed for u in Equation 6.19.

$$u_{i+1} = u_i + \dot{u} \tag{6.19}$$

Iteration Using the velocities, pitchrates and angles the process can start over. This is continued until the simulation reaches the t_{end} specified by the user.

6.5.3 Phugoid longitudinal eigenmotion

For rotorcraft the phugoid longitudinal eigenmotion is the exchange of speed and height. In general it is characterized by a low frequency oscillation in height, u and θ_{f} at an approximately constant α. For rotorcraft this eigenmode is not necessarily stable, as it may diverge for free, uncontrolled motions. In general the longitudinal phugoid is highly damped by a horizontal tailplane.

To analyze the phugoid motion for the eGyro, the model described in section 6.5.2 was used. A disturbance of 5 $\left[\frac{\mathrm{m}}{\mathrm{s}^2}\right]$ was applied to initiate the phugoid. The input data for the simulation can be found in Table 6.4.

To determine the time to half amplitude of the phugoid motion an extrapolation of the positive peaks of the oscillation is constructed. With this extrapolation the time to half amplitude can be constructed more accurately as it is not dependent on the locations of the peaks. From theory it can be derived that the magnitude of the amplitude dampens exponentially.[33] The extrapolation used is given in Equation 6.20 as a function of time t, where M is the magnitude of the extrapolation and coefficients A and B are derived from the maximum and following peak respectively.

$$M = A \cdot e^{B \cdot t} \tag{6.20}$$

Using the extrapolation, a t_{12} and period were obtained , which are displayed in Table 6.5. A plot with the extrapolation is given in Figure 6.13.

Table 6.4: Phugoid input data

Input	Value	Unit
t_{end}	20	[s]
step	0.01	[s]
cruise speed	200	$[\frac{\text{km}}{\text{h}}]$
α_{dist}	0	[deg]
q_{dist}	0	$[\frac{\text{deg}}{\text{s}}]$
θ_{fdist}	0	[deg]
w_{dist}	5	$[\frac{\text{m}}{\text{s}}]$
u_{dist}	0	$[\frac{\text{m}}{\text{s}}]$

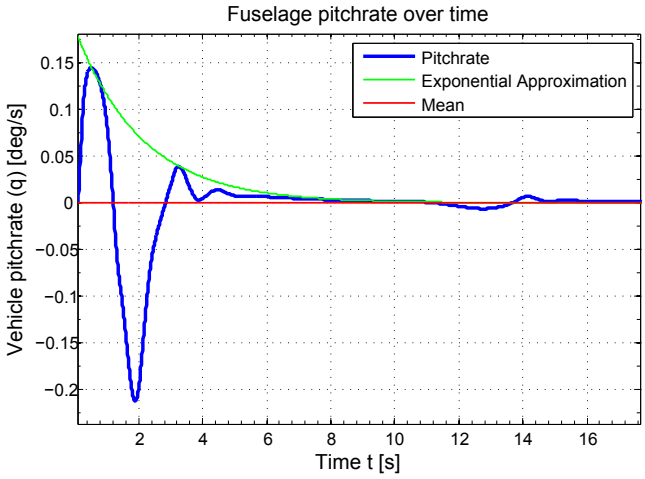

Figure 6.13: Plot of phugoid pitchrate

The real and imaginary parts of the eigenvalues can be computed with Equations 6.21 and 6.22 [38]. For the simulation these are displayed in Table 6.5.

$$t_{12} = -\frac{\ln 2}{\text{Re} \cdot \lambda} \tag{6.21}$$

$$\text{period} = \frac{2\pi}{|\ \text{Im} \cdot \lambda\ |} \tag{6.22}$$

The phugoid eigenmotion can also be approximated analytically using Equation 6.23 [37]. For this equation, the stability derivatives M_u, X_u and M_q have to be known. These are obtained by applying a step change, in for example u, and observing the change in M_{cg} using the three degrees of freedom simulation program. However unsatisfactory results (only real eigenvalues) are obtained. The results are displayed in 6.5.

$$\lambda^2 - \left(X_u + g_0 \cdot \frac{M_u}{M_q}\right)\lambda - g_0 \frac{M_u}{M_q} = 0 \tag{6.23}$$

In conclusion it can be observed the eGyro shows a stable, fast converging phugoid eigenmotion. This can be contributed to the relatively large horizontal tail surface which dampens the phugoid eigenmotion.

6.5.4 Short period longitudinal eigenmotion

To analyze the short period motion of the eGyro, the model described in subsection 6.5.2 is used. A disturbance θ_{f} of only 0.2 [deg] is applied to initiate the short period motion. The model is unstable for larger instantaneous fuselage deflection angles. The input data for the simulation can be found in table 6.6.

Table 6.5: Results of the phugoid eigenmotion

Variable	Numerical	Analytical
t_{12}	1.450 [s]	–
Period	2.72 [s]	–
Re lambda	-0.478	-0.762 and -695
Im lambda	$-2.31i$ and $2.31i$	–

Table 6.6: Input values short period

Input	Value
t_{end}	10 [s]
step	0.01 [s]
v_0	200 $[\frac{\text{km}}{\text{h}}]$
α_{dist}	0 [deg]
q_{dist}	0 $[\frac{\text{deg}}{\text{s}}]$
$\theta_{\text{f}dist}$	0.2 [deg]
w_{dist}	0 $[\frac{\text{m}}{\text{s}}]$
u_{dist}	0$[\frac{\text{m}}{\text{s}}]$

The $t_{1/2}$ and period of the short period eigenmotion are determined graphically as displayed in 6.14. The α plot provides the suitable values to obtain $t_{1/2}$ and period. The obtained values are given in Table 6.7.

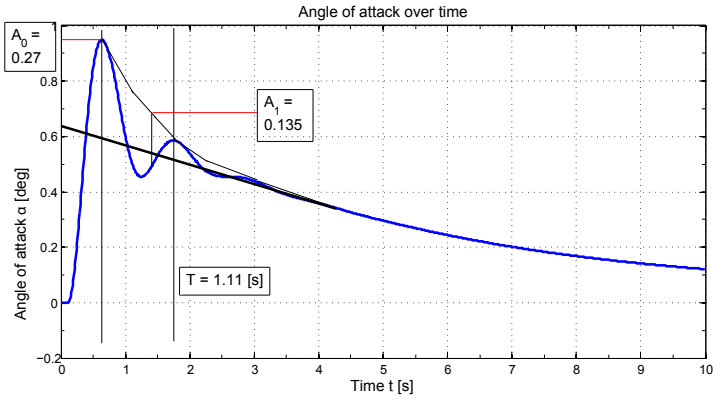

Figure 6.14: Plot of short period angle of attack

The short period eigenmotion can also be approximated analytically using Equation 6.24 [37]. For this equation, the stability derivatives Z_w, M_q and M_w have to be known. These were obtained as described in subsection6.5.3. However unsatisfactory values (only real eigenvalues) were obtained. The results are displayed in 6.7.

$$\lambda^2 - (Z_u + M_q)\,\lambda - M_w \cdot u_0 = 0 \tag{6.24}$$

To conclude the short period motion analysis, it can be stated that a realistic short period motion is displayed with the analysis. For short period motions in general t_{12} is less than one second. The eGyro shows a t_{12} of 0.762 [s]. Rotorcraft generally posses strongly damped short period motion. It is shown that the eGyro has a stable, fast converging short period motion.

Table 6.7: Results of the short period eigenmotion

Variable	Numerical	Analytical
	0.762 [s]	–
	1.11 [s]	–
Re λ	-0.912	16.67 and -0.6466
Im λ	$-5.66i$ and $5.66i$	–

6.6 Lateral stability

For the eGyro several lateral eigenmotions are of interest. These include the spiral and dutch roll mode. Analysis of these motions is beyond the scope of this report.

6.6.1 Spiral mode

The spiral mode is initiated by a roll perturbation in forward flight. This can increase the roll angle or the roll angle can converge back to the initial undisturbed condition. The reaction of the aircraft for such a perturbation is determined by the static roll stability.

When the spiral motion is statically unstable the pilot has to react to apply a corrective control input.

The spiral motion is mainly affected by the these stability derivatives: N_r which gives the change in yaw moment for a yaw rate perturbation and N_v provides the change in yaw moment for a lateral velocity perturbation. Also L_r and L_v determine the spiral motion response. These give the change in roll moment as a result of a disturbance in yaw and lateral velocity respectively [37]. The vertical tail surface has a large influence on the mentioned stability derivatives and thus contributes to the spiral stability of the vehicle.

6.6.2 Dutch Roll

For helicopters, the dutch roll motion is generally referred to as the lateral/directional oscillation. The combines an oscillation in yaw, roll and pitch angle, coupling longitudinal and lateral stability. It is affected by the same derivatives as the spiral mode, complemented by the sideslip of the vehicle during forward flight.

For a lateral stable rotorcraft a suitable configuration of the dihedral effect and the directional stability has to be found. Often, a stable Dutch Roll motion does not imply a stable spiral motion and vice versa [20]. This is illustrated in figure 6.15.

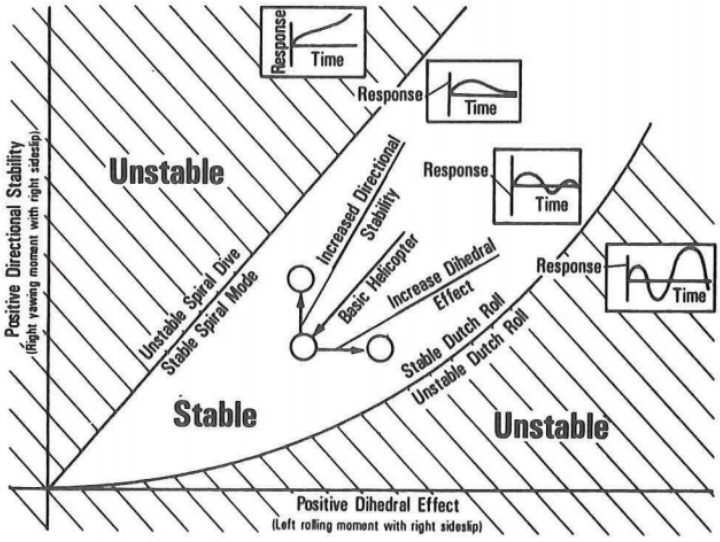

Figure 6.15: Dihedral effect and directional stability

6.7 Controllability

For the control of the eGyro no analysis is performed as stability is a much more important criteria and controllability cannot be analyzed without a solid static and dynamic stability analysis. However, a general impression of the control characteristics during cruise flight and VTOL is given.

6.7.1 Auto-rotation control

It can be stated that the general control characteristics of an auto-gyro type aircraft can be regarded as favorable during cruise flight. Another advantage of auto-gyros is the absence of a full stall. When compared to fixed wing aircraft it is really hard to get a gyro-plane into full stall. Pilot induced oscillations (PIO's) can be a problem for higher cruise speeds for auto-gyro type aircraft. If the three degrees of freedom model is any indication, the aircraft shows stable longitudinal behavior, which is important for sufficient control characteristics. However, an aircraft which is too stable can show control characteristics which respond too slow and makes the aircraft harder to maneuver.

During flight on auto-rotation, the control of the eGyro is manual and no fly-by-wire system interacts with pilot control inputs. By default, the auto-gyro has three control inputs: the cyclic-pitch θ_c, horizontal propulsion thrust and rudder (vertical tail surface) control. For the eGyro, these are all present and the horizontal thrust is provided by the aft ducted fans. One extra control input may be identified as α_{trim}, which is used to trim the aircraft for different cruise conditions.

6.7.2 Control during hover and VTOL

During VTOL, control of the vehicle is performed using the four ducted fans. A control algorithm comparable to those of Quadcopter Unmanned Aerial Vehicles is used. Thrust differentiation of the fans is implemented to obtain maneuver and stability characteristics. This is achieved by placing the center of gravity such that the resultant moment during VTOL and hover of the fans is zero.

Furthermore, a computerized system ensures that thrust differentations are applied such that vehicle attitude and longitudinal, lateral accelerations stay within predefined bounds. It is assumed that rapid thrust differentations can be applied, as the fans are powered by a series of electric motors. Electric motors are characterized by the ability to produce large fluctuations in power output. The motors provide their maximum torque at low rotations per minute. Also rapid power delivery to the fans and motors can be achieved as electric power is always available from the batteries. Furthermore, no mechanical or transmission linkage is present which could limit rapid power delivery and rpm change to the fans.

The pilot can provide control inputs to a fly-by-wire system, which would then allow accelerations and attitude changes of the vehicle which correspond to the output of the pilot control input.

Fly-by-wire systems will also assist the pilot during the transition from VTOL to cruise flight.

7 Performance

The performance characteristics of the eGyro are discussed in the following chapter. First an extensive mission description is presented, followed by the payload-range diagrams. After that, the performance diagrams are shown and the load factors for the vehicle will be explained. Finally, the sustainability aspects like noise and emissions are discussed.

7.1 Mission Description

The main mission that the eGyro has to carry out is defined from the point at which the crew enters the vehicle on the ground. From there it covers the take-off, transition, cruise, descent and landing phase. All important parameters such as time, distances, climb-performances and velocities, are calculated for each segment of the mission. On that basis, the final mission performance can be obtained. The most relevant factors are the rescue time, range and endurance. Furthermore, this section will assist in later calculations for the emission, which is rated as another very critical component for the vehicle to be designed. For all calculations, a MATLAB script is used. In case of input changes, the related parameter changes can be found immediately. A mission profile diagram, showing all the different phases that are described further in this subsection can be seen below, in Figure 7.1. All different phases are indicated as function of altitude and time. Furthermore, the climb rates are shown. The entire mission consists of a VTOL and cruise to the area of interest, where a patient can be boarded and brought to the nearest located hospital if necessary. The flight to the hospital is only optional and thus indicted with the dashed line. The final VTOL and cruise segment describes the flight back to the main base, where the vehicle can be prepared for the next mission immediately. The mission profile gives an example of the mission, directly related to the set requirements, with a distance of 110 [km] and the therewith spent rescue time [3].

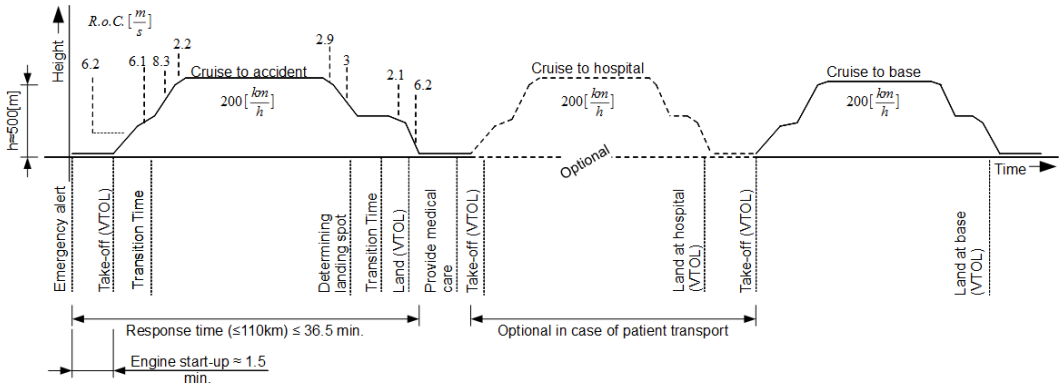

Figure 7.1: Flight Mission Profile of the eGyro, with Rate of Climb Values

7.1.1 Input

The input for the calculations are derived mostly from the Baseline Report [3] and the other analysis performed in this report. The most important inputs are the MTOW of 1850 [kg], which was used for the initial iteration and the maximum power of the front and rear fans, which are 260 [kW] and 356 [kW] respectively. Furthermore, the maximum available thrust at cruise equals 2.017 [kN] and mass flows of 88 $\left[\frac{\text{kg}}{\text{s}}\right]$ and 110 $\left[\frac{\text{kg}}{\text{s}}\right]$ are used for the front and rear fans, respectively. These values were obtained from the propulsion analysis. The mass flow is assumed to be independent of the different thrust and power settings of the motors. This is not entirely realistic, but the mass flow change is hard to determine as

a function of the different power settings and/or rotations per minute of the motors, with the limited information given. However, considering the fact that the fans will mostly operate close to full cruise power, zero power or the power necessary to assure hovering of the vehicle, it is assumed that the change in mass flow at these stages is not a critical factor at this point. Furthermore, a mass flow efficiency of 80 % for the rear fans during lower cruise speeds and 90 % for the front fans is assumed. However, close to the cruise speed a 100 % mass flow efficiency for the rear fans is assumed. Also, a lift over drag (L/D) ratio of 4.5 during cruise and vehicle dimensions are input values from other sections. Aerodynamic parameters like the rotor lift at different speeds and the profile drag coefficients are provided in Chapter 5. Finally, engine specifications such as the specific fuel consumption of 0.274 $\left[\frac{\text{kg}}{\text{kWh}}\right]$ are obtained from the engine data sheet [15].

7.1.2 Phase 1, Start-up and Vertical Take-off

During the first phase of the mission, the pilots have to enter the vehicle, close the doors and get seated. Additional, the Arriel 2C2 turboshaft engine has to be put in idle mode, while the motors in every ducted fan are put to full power setting, using the batteries as energy source. It is assumed that refueling and all other preparations, including the medical components, are already done beforehand. This part is assumed to take 90 [s], whereof only the last 20 [s] are dedicated to the gradual power increase of the motors. The final part of phase 1 covers the Vertical Take-off (VTO) till a height of 100 [m]. During VTO, the main rotor is unfolded entirely, but does not rotate yet. The height of 100 [m] is chosen due to clearance factors. From that altitude the rotor should have enough space to start rotating in most cases. Furthermore, a constant climb rate of 6.2 $\left[\frac{\text{m}}{\text{s}}\right]$ is calculated. An explanation for the climb rate computation is given in the next section. Using the basic distance versus speed and time formula and the assumption of only vertical climb, without any movement in the horizontal direction, a time of 17 [s] can be derived for the first ascent part. Hence, the total time for phase 1 equals 1:47 [min], of which the motors are running 37 [s] on full power. The Arriel 2C2 turboshaft engine is only operating in idle mode throughout the first phase.

7.1.3 Phase 2, Pre-rotation of Rotor

At the start of phase 2, the rear motors will still be operating at full power in order to provide the highest possible thrust upwards. However, at the same time the main rotor is pre-rotated by a small pre-rotation motor to 160 [rpm]. This minimum rotational speed is calculated on the basis that the maximum profile drag of the rotor has to be overcome by the initial pre-rotation, making use of blade element theory [14]. Using the power relations between the hovering power and the induced power, the profile power can be found, using Equation (7.1)

$$P_{\text{p}} = P_{\text{hover}} - P_{\text{i}} = \frac{\text{MTOW} \cdot g_0}{\eta_{\text{hover}}} \cdot \sqrt{\frac{\text{MTOW} \cdot g_0}{2 \cdot \rho \cdot \pi \cdot {r_{\text{r}}}^2}} - (1.2 \cdot \text{MTOW} \cdot g_0 \cdot v_{\text{ind}}) \tag{7.1}$$

The hover efficiency η_{hover} is taken from the figure of merit [29] and assumed to be 0.8.

$$v_{\text{ind}}^4 + V^2 \cdot v_{\text{ind}}^2 - 1 = 0 \tag{7.2}$$

$$v_{\text{ind}}^4 = \frac{v_i^4}{v_{\text{ind}_{\text{h}}}} \tag{7.3}$$

$$\bar{V}^2 = \frac{V}{v_{\text{ind}_{\text{h}}}} \tag{7.4}$$

$$v_{\text{ind}} = \sqrt[4]{\frac{(\text{MTOW} \cdot g_0)^2}{4 \cdot \rho^2 \cdot \pi^2 \cdot {r_{\text{r}}}^4}} \tag{7.5}$$

Furthermore, using the velocity relations at low speed, Equations (7.2), (7.3) and (7.4) can be used to determine the induced velocity, which is given by Equation (7.5), where a horizontal velocity V of 0 $\left[\frac{\text{m}}{\text{s}}\right]$ due to hovering is assumed.

Computing with the given parameters, a hovering power of 262.5 [kW], an induced power of 252 [kW] and thus a profile power of 10.5 [kW] is obtained. Next, using Equation (7.6) with a velocity of 0 $\left[\frac{\mathrm{m}}{\mathrm{s}}\right]$, it can be shown that the profile power above is equal to the profile power at hovering.

$$P_{\mathrm{p,hover}} = \frac{P_{\mathrm{p}}}{1 + 4.65 \cdot \left(\frac{V}{\omega_{\mathrm{r}} \cdot r_{\mathrm{r}}}\right)^2} \tag{7.6}$$

$$\omega_{\mathrm{r}} = \sqrt[3]{\frac{P_{\mathrm{p,hover}}}{\sigma \cdot C_{d,\mathrm{profile}} \cdot \rho \cdot \pi \cdot {r_{\mathrm{r}}}^5}} \tag{7.7}$$

Finally, the rotational rate can be determined. A profile drag with a profile drag coefficient of 0.03 during cruise has to be overcome during pre-rotation with a solidity ratio σ of 0.0841. Both values are provided by the aerodynamic analysis, as can be seen in Chapter 5. Equation (7.7) gives a minimum pre-rotational value of 13.7 $\left[\frac{\mathrm{rad}}{\mathrm{s}}\right]$, which is equivalent to 130 [rpm]. Since achieving a sufficient rotational speed on the main rotor is necessary to start the auto-rotation phase properly. 160 rotations per minute are chosen to ensure a safety margin of 20 %.

Since the pre-rotation procedures cause a moment around the vehicle's z-axis, a counteracting moment has to be created in order to prevent the vehicle from rotating. Therefore, the rear fans will start to tilt in opposite directions. One fan is tilted forward, whilst the other fan is tilted backwards. Hence, the horizontal vector of the thrust produced forward by one fan will be opposed by the same thrust in the other direction, caused by the other fan. Hence, there is no horizontal net thrust force. For this phase it is assumed that the fans can tilt with a rate of 1 $\left[\frac{\mathrm{deg}}{\mathrm{s}}\right]$.

The abovementioned rotational rate does not cause any mechanical problems. Furthermore, it is slow enough to make sure that the moments acting are not increasing too fast during the most critical part of the mission. Since the motors are rotating with a constant power setting, the vertical thrust produced by the fans will decrease over time, as the tilt angle φ gets larger. This also implies a decrease of the fan introduced climb rate. At time $t = 0$ and tilt angle $\varphi = 0$, the vertical thrust is equivalent to the thrust in phase 1. Hence, also the climb rate is identical at that point. In order to calculate the climb rate in phase 2, the maximum thrust is first determined using Equation (7.8).

$$T_{\mathrm{max}} = \sqrt{2 \cdot \dot{m} \cdot \eta_{\dot{m}} \cdot P_{\mathrm{max}}} \tag{7.8}$$

The maximum thrust can be found for both the front and rear fans using the respective mass flow efficiencies, mass flows and maximum power settings. Since the maximum power settings are chosen such that the vehicle stays in static equilibrium during the climb, the thrust ratio for stability of the vehicle can be found by dividing the highest rear fan thrust by the highest front fan thrust. Making use of this thrust ratio, the thrust necessary for hovering can be found for all four fans.

During the second step, the vertical thrust is computed as a function of the motor tilt angle φ, as can be seen in Equation (7.9).

$$T_{\mathrm{vertical}} = T_{\mathrm{max}} \cdot \cos\varphi \tag{7.9}$$

As equation (7.9) indicates, the vertical thrust of the fans decreases with an increase of φ. Using the vector with the decreasing vertical thrust values and Equation (7.9), the related vertical power can be found for every angle setting. However, for the climb rate the vertical power in excess is important. This can be computed by subtracting the power necessary for hovering from the total vertical power at the different stages. While the power from the rear fans decreases, also the thrust from the front fans has to decrease in a relative manner, such that the vehicle remains stable. Thus, the excess power of the front fans is determined using the stability ratio. Additionally, the rotor produced lift is accounted for.

As the rotor is speeding up, its vertical lift will also increase. A value of 2000 [N] of rotor thrust is given from the aerodynamics analysis, Section 5, at 160 [rpm] and the corresponding rotor angle setting. For simplicity reasons a linear progression of the rotor lift is assumed. The thrust produced by the rotor will be subtracted from the fan thrust at each time step, such that the climb rate stays within a reasonable range. This also means that the fan power decreases equally with the increase in rotor thrust.

Once the total excess power for the rear fans, front fans and rotor is known as a function of pitch angle θ, the pointwise climb rate is calculated using Equation (7.10)

$$\mathrm{RoC} = \frac{P_{\mathrm{hover,excess}}}{\mathrm{MTOW} \cdot g_0} \tag{7.10}$$

With the climb rate at each angle θ, the total climb distance due to the fans can be found for phase 2, by integrating over each interval, as can be seen in Equation (7.11)

$$s_{\text{climb}} = \sum \left(s_{\text{climb},i-1} + \frac{0.5 \cdot (\text{RoC}_{i-1} + \text{RoC}_i)}{t_{\text{step}}} \right) \tag{7.11}$$

The only undetermined factors are the final pitch angle of the fans and thus the time for phase two. In order to get these parameters, the moment created by the rear fans is used. This is dependent on the angle setting, the thereof derived horizontal thrust and the distance to the vehicle center of gravity, Equation (7.12):

$$M_{\text{fan}} = T_{\max} \cdot \sin \varphi \cdot d_{\text{cg}} \tag{7.12}$$

Since the vehicle has to be kept stable, the moment created by the rotor has to be equal to the moment of the fans for every angle φ. Knowing these moments and the inertia of the main rotor, the angular acceleration at each time step is calculated by using Equation (7.13).

$$\alpha_{\text{rotor}} = \frac{M_{\text{fan}}}{I_{\text{rotor}}} \tag{7.13}$$

The inertia of the rotor is calculated to be 247 [$\text{kg} \cdot \text{m}^2$], using the general equation of the beam inertia. With Equation (7.14), the final angular velocity can be found when integrating over each interval.

$$\omega_{\text{r}} = \sum \left(\omega_{\text{r},i-1} + \frac{0.5 \cdot (\alpha_{\text{rotor},i-1} + \alpha_{\text{rotor},i})}{t_{\text{step}}} \right) \tag{7.14}$$

The angular velocity desired at the highest angle, is equal to half of the final angular velocity in phase 2. In other words, the fans will first increase the tilt angle φ until half of the pre-rotational speed is achieved and will then rotate back to the original position. By the time both rear fans are vertically oriented, the rotor will be at its final rotational speed. This means that the time and maximum angle of phase 2 can now be found by simply optimizing these two parameters until the desired rotational speed of the main rotor of 160 [rpm] is achieved. Furthermore, a check is performed, which makes sure that the maximum angle of the fans does not exceed the maximum allowable angle. This critical angle is defined as the angle φ. At which the vertical thrust is less than the vertical thrust necessary to keep the vehicle hovering. This angle is computed to be 26.45 [deg].

The final results for phase 2 are a total time of 9 [s], a total climb distance of 51 [m] and a maximum tilt angle of 4.5 [deg]. This also clearly shows that the maximum angle is far below the critical angle. It is also important to notice that several additional assumptions are made to simplify the calculations above. For phase 2 no drag forces are considered, since the climb rate with a maximum of 6.2 $\left[\frac{\text{m}}{\text{s}}\right]$ and an average of 6.14 $\left[\frac{\text{m}}{\text{s}}\right]$ is assumed to have a low impact on the produced drag. Also, the entire climb is assumed to be steady, with no wind gust interruptions. In case of sudden wind gusts, the power settings of the fans will be adjusted to keep the vehicle stable. The rotation of the fans is purely due to the counteracting moment and not meant for any stability issue corrections.

7.1.4 Phase 3, Acceleration with Lift from Rotor

Phase 3 consists of the first horizontal acceleration. The rotor is now rotating with its pre-rotational speed of 160 [rpm]. The pre-rotational motor maintains the angular velocity from phase 2. However, towards the end of phase 3, the motor will be disconnected entirely as soon as the airspeed is high enough to put the rotor into auto-rotation. To make this feasible, both rear fans are tilted forward from their initial vertical position in a synchronized way. The rotational rate is still kept at 1 $\left[\frac{\text{deg}}{\text{s}}\right]$, for the same reasons as already stated in phase 2. Phase 3 is finalized when both rear fans have rotated till the critical tilt angle φ. The power of both rear fans is kept at maximum, such that the highest possible forward acceleration is achieved. Thus, the vehicle will move forward and climb at the same time, while the thrust settings of the front fans have to be adjusted accordingly in order to ensure stability. Once the fans are at the critical tilt angle, the vertical thrust is just high enough to keep the vehicle stationary and the climb rate will be solely determined by the rotor. The climb rate of the fans is computed in a similar

manner as already described in the previous section. For the acceleration, the horizontal force vector at every time instant is found. Using Equation (7.15), the acceleration at each time step is computed.

$$a_{\text{hor}} = \frac{T_{\max} \cdot \sin\varphi}{\text{MTOW}} \tag{7.15}$$

The mass is assumed to stay constant during the VTOL phases. This assumption is very reasonable, since all VTOL phases have a short duration and the turboshaft engine is only operating in idle mode, which requires low fuel consumption. However, towards the end of phase 3, the Arriel 2C2 will be put on its operational power, such that the motors can be further provided with the required power, while the batteries can be recharged simultaneously. After the determination of all stepwise accelerations, the speed for each equivalent interval can be found using the simple acceleration equation over the vector length, as can be seen in Equation (7.16):

$$v_i = (a_{\text{hor},i+1} - a_{\text{hor}\,i}) \cdot t_{\text{step}} \tag{7.16}$$

This velocity vector still has to undergo further operations. First of all the drag is included, using Equation (7.17). Hence, the initial velocities are updated with a simple optimization process, including the drag values. Furthermore the thrust from the fans will decrease, since the power required increases with speed. For simplicity reasons a linear decrease of thrust versus speed is used, taking the thrust values from cruise speed and take-off as a reference.

$$D = \frac{1}{2} \cdot \rho \cdot {v_{\text{ind}}}^2 \cdot S \cdot C_d \tag{7.17}$$

Iterating Equation (7.17) and (7.16) and the resulting decrease in thrust for a sufficiently small error, a final velocity of 31 $\left[\frac{\text{m}}{\text{s}}\right]$ is achieved. This is at the end of phase 3, with the final fan angle φ being the critical one at 26.45 [deg].

Finally the climb rate due to the rotor has to be found. The first step is to find the lift produced by the rotor. Again a linear assumption is made, using a final value of 6500 [N] at 30 $\left[\frac{\text{m}}{\text{s}}\right]$ and the 2000 [N] at 160 [rpm] from the aerodynamic analysis, as can be seen in Chapter 5.

With Equations (7.18) and (7.19), the total parasitic drag and thereof derived disk angles are obtained.

$$D_{\text{par}} = \frac{1}{2} \cdot \rho \cdot {v_{\text{ind}}}^2 \cdot \pi \cdot {r_{\text{r}}}^2 \cdot C_{d,\text{par}} \tag{7.18}$$

$$\alpha_{\text{d}} = \frac{D_{\text{par}}}{(\text{MTOW} \cdot g_0)} \tag{7.19}$$

Parasitic drag increases to around 1150 [N] towards the end of phase 3. In Equation (7.18), r_{r} describes the rotor radius of 4.24 [m] and the corresponding parasitic drag coefficient. Finally, the induced velocity can be found after computing the resultant velocity through an iterative process, using the Glauert's method [27], as can be seen in Equations (7.20) and (7.21):

$$v_{\text{r}} = \sqrt{(v_0 \cdot \cos\alpha_{\text{d}})^2 + \left(v_0 \cdot \sin\alpha_{\text{d}} - \frac{T_{\text{rotor}}}{2 \cdot \rho \cdot \pi \cdot {r_{\text{r}}}^2 \cdot v_{\text{r}}}\right)^2} \tag{7.20}$$

$$v_{\text{ind}} = \frac{T_{\text{rotor}}}{2 \cdot \rho \cdot \pi \cdot {r_{\text{r}}}^2 \cdot v_{\text{r}}} \tag{7.21}$$

As soon as the induced velocity at every point is known, the climb rate, provided due to the rotor climb velocity, can be found with the momentum theory for vertical climb [28], using Equation (7.22).

$$v_{\text{climb}} = \frac{(T_{\text{rotor}} - (2 \cdot \rho \cdot \pi \cdot {r_{\text{r}}}^2 \cdot {v_{\text{ind}}}^2))}{(2 \cdot \rho \cdot \pi \cdot {r_{\text{r}}}^2 \cdot v_{\text{ind}})} \tag{7.22}$$

Adding together the climb rate vector from the rotor with the equivalent time step climb rates of the fans, the total climb rate is obtained. The average total climb rate in phase 3 equals 8.3 $\left[\frac{\text{m}}{\text{s}}\right]$, which over the time of 27 [s] leads to a ascent distance of 217 [m]. Furthermore, the vehicle travels 300 [m] in the horizontal direction. Also in this phase, certain assumptions are made. The actual climb rate will be lower in reality, since drag values are not included for the climb speed. Additionally, the lift produced by the rotor will not increase linearly with increasing velocity as assumed for the previous calculations. For the entire phase, the motors will still run on the battery power, while the turboshaft engine is running on idle.

7.1.5 Phase 4, Final Acceleration to Cruise Speed

During phase 4, the vehicle will continue its accelerating from 31 $\left[\frac{\text{m}}{\text{s}}\right]$ to the final cruise speed of 55.54 $\left[\frac{\text{m}}{\text{s}}\right]$. Since the rotor is already producing a large amount of lift, the fans are now rotating beyond the critical angle, while the rotor start to take over larger portions of the lift produced. The rotational rate during this phase is chosen to be 2 $\left[\frac{\text{deg}}{\text{s}}\right]$ to speed up the acceleration process. The front fans are slowly shut down, as the main rotor produces sufficient lift to keep the vehicle airborne. Also, the electric motors are switched from battery provided power to engine provided power, as soon as the transition into phase 4 has started. For the fuel flow calculations it is assumed that the batteries will stop their power delivery after half of phase 4 is complete.

The velocity increase is calculated on a similar basis as in phase 3, using Equations (7.15), (7.16) and (7.17), meaning that the effect of increasing thrust with an increase in velocity is accounted for. Additional, as for phase 3, the reduction in thrust due to the gain in speed is used. On that basis, the full cruise speed is achieved after 21 [s] into phase 4 and a horizontal travel distance of 505 [m] is computed at that point. The total altitude after phase 3 is still only 439 [m]. Therefore, an additional climb of $61 - 161$ [m] has to be performed, in order to arrive at the nominal cruise altitude of $500 - 600$ [m]. This particular altitude is chosen to minimize the response time and is closely related to the typical cruise altitude of helicopters in emergency missions, as stated by the helicopter rescue service in Rotterdam. Furthermore, the highest buildings in the Netherlands do not exceed 500 [m]. This final ascent can be achieved by the rotor during phase 4. In case of special missions in remote areas, the cruise altitude might increase due to mountains and other obstacles. In that case, the climb to cruise altitude will take longer than the 21 [s] of phase 4. However, an additional minute is included between phase 4 and the final cruise flight for that reason. During that minute the vehicle can already cruise with its cruise speed, or further climb to a higher altitude if preferred by the pilots. The total time till cruise is 3.44 [min], including the start up at the ground. From this time, the electric motors are operating on battery power for a maximum of 1.33 [min]. The total distance travelled equals 4.1 [km].

7.1.6 Phase 5, Cruise

The cruise flight is the main part of the mission. During cruise, fuel fraction calculations are used to calculate the maximum range efficiently. In order to do that, a steady condition is assumed, where the lift produced by the rotor is equal to the weight of the vehicle. Using the specific fuel consumption of the Arriel 2C2 turboshaft engine [15], the mass flow rate can be determined as a function of the provided power, as can be seen in Equation (7.23).

$$\dot{m}_{\text{fuel}} = \frac{\text{SFC} \cdot P_{\text{a}}}{3600} \tag{7.23}$$

For every time step, the vehicle weight, and thus the required lift decreases, leading to a change in the rotor disk angle. Therefore the profile drag coefficient will decrease, using Equation (7.19), which results in a decrease of the total drag. With less drag, the required power that the rear fans have to produce decreases, which implies another reduction of the fuel flow. Iterating over the span of the cruise phase with the known amount of accessible fuel weight on board, the cruise endurance is computed, giving a value of 2.07 [h]. Based on that, the cruise range of 430 [km] is determined, since the cruise speed is an already known parameter of 55.54 $\left[\frac{\text{m}}{\text{s}}\right]$. It should be noticed that a totally stable and undisturbed cruise flight is assumed. In reality, wind conditions and required operational maneuvers, will result in a slight decrease of these cruise specifications. The cruise phase, including the extra ascent time of 1 [min] and an extra descent time of 2 [min], both performed at cruise speed. The main reason to include such an extra time margin is the case of a higher required cruise altitude and the fact that a low speed descent before the landing is preferred due to safety reasons.

7.1.7 Phase 6, First Descent

During phase 6 the vehicle will start to reduce altitude. In order to save fuel, advantage is made of the drag, reducing the velocity and altitude. Therefore, the motors are nearly switched off and the vehicle will decelerate. This is done by iterating the velocity, drag and deceleration for each time step. The duration of phase 6 is chosen to be 1 [min]. During that time, the vehicle will decelerate from cruise speed to 17 $\left[\frac{\text{m}}{\text{s}}\right]$, with a descent distance of 180 [m]. The travelled distance during phase 6 equals 1714 [m] (see Equation (7.24)). The rear fans will start to slowly move back to the vertical position with $1 - 2$

$\left[\frac{\text{deg}}{\text{s}}\right]$ until the static hovering angle is achieved. As a safety margin, it is assumed that the motors run on battery power for the last half of phase 6 with an average descent rate of 3 $\left[\frac{\text{m}}{\text{s}}\right]$.

$$s_{\text{descend}} = \sum \left[v_{\text{ind}} + \left(\frac{\frac{1}{2} \cdot \rho \cdot {v_{\text{ind}}}^2 \cdot C_d \cdot S}{\text{MTOW} \cdot g_0} \right) \cdot t_{\text{step}} \right] t_{\text{step}} \tag{7.24}$$

7.1.8 Phase 7, Final Deceleration

During phase 7, the vehicle is further decreasing its velocity to zero. Also the front fans are switched on, in order to produce lift and maintain stability. The main rotor has to be put in a steadily increasing disk angle, in order to assist the deceleration. The time for phase 7 is 16 [s] and the travel distance 124 [m]. Since the fans are slowly put to the necessary lift, no descent is achieved. During phase 7, the electric motors are operating on battery power again, while the Arriel 2C2 is running in idle mode.

7.1.9 Phase 8, Stopping Rotor

Similar to phase 2, Equations (7.8) to (7.14) are used in phase 8 for the rotor deceleration. For the beginning of phase 8, the same rotational rate of 160 [rpm] is assumed, being equivalent to the final rotational speed at the end phase 2. In other words, the slowing down process is similar to the speeding up procedure. The only difference is that the fans are producing slightly less thrust. The reason for that is the descent rate which is achieved at the same time. Therefore, the fans are put to a power level with a net vertical thrust deficit of 500 [N], compared to the hovering required thrust. With that, the total time of phase 8 becomes 10 [s], during which both rear fans are moving in opposite direction, to counteract the moment created by the decelerating rotor. The average descent rate is calculated to be 2.1 $\left[\frac{\text{m}}{\text{s}}\right]$, which leads to a total descent distance of 21 [m]. Also phase 8 is performed while the engine runs on idle, and the motors are provided with the required energy by the batteries.

7.1.10 Phase 9, Landing

During phase 9, the vehicle will descent the last 120 [m], where the rotor is stationary. The motors are running on battery and provide just enough lift to assure an average descent rate of 6.2 $\left[\frac{\text{m}}{\text{s}}\right]$. The required time for this procedure is calculated to be 20 [s]. Furthermore a shut-down time of 20 [s] is included in this phase.

The total time to land from cruise is therewith 4.46 [min]. From this time, 2 [min] are used for an additional descent between phases 5 and 6. Since the total descent distance mentioned in the previous paragraphs equals only 321 [m], an additional descent of $178 - 278$ [m] is required to land from the nominal mentioned cruise altitude of 500 to 600 [m]. During the total descent time, only a maximum of 1.18 [min] of battery power is necessary, including half of phase 6 with battery power delivery. The total distance travelled after cruise equals 8504 [m]. In order to have a visual image of the times, distances and altitudes of the cruise to VTOL procedure, the final part after the dashed line of the height versus altitude and height versus time diagrams can be used.

A summary of the time, travel distance and altitude for each phase is indicated in Figures 7.2 and 7.3. The above mentioned phases, excluding the extra climb and descent times of in total 3 min and the cruise, are indicated by the solid blue line. The cruise and reserve times for extra climb and descent are shown with the dashed line segment in the plots. The corresponding values for the time, height and travelled distance are written on the y and x axis. It should be noticed that the cruise and start-up phase are not indicated with an equivalent scale, in order to make the plots easier to read.

7.1.11 Range, Endurance and Rescue Time

Finally, a total endurance of 2.4 [h] and total range of 442.6 [km] can be calculated. This is done by summing up the travelled distances and spent times of every phase. Since the fuel flow of the turboshaft engine at idle is unknown, a value has to be estimated. Since the fuel flow is derived from the specific fuel consumption, an idle power has to be found. As no exact values could be found, an idle power value of 60 [kW] is assumed at this point, which is 12 % of the maximum delivered power. In reality it is probably lower. Thus, the range and endurance values can be even higher, also considering that the batteries are recharged during cruise, and could be used as energy source for further flight maneuvers. However,

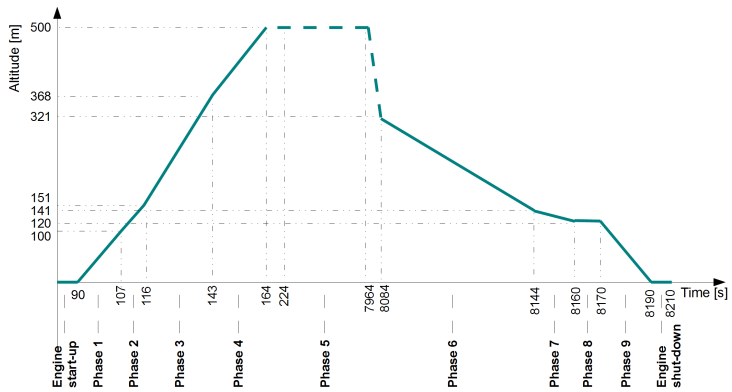

Figure 7.2: Altitude versus Time Diagram

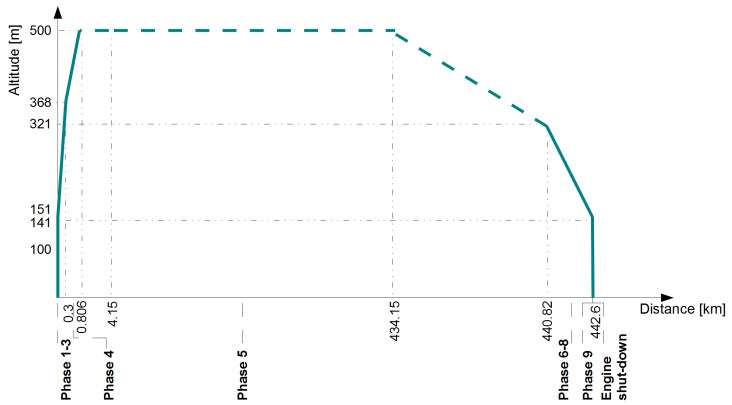

Figure 7.3: Altitude versus Distance Diagram

for safety reason this is not included in the nominal maximum range and endurance calculations. On the other hand, outside factors like wind gusts and other operational variations that might involve extra power are not accounted for.

Considering the flight mission profile, the maximum emergency area distance, within reach of the eGyro is 205 [km], assuming that the maximum distance from the emergency area to the closest hospital is 30 [km]. To give an overview of the range possibilities from Amsterdam, a range map is shown in Figure 7.4. The map shows that the range covers the entire Netherlands and even Dortmund in Germany can almost be reached from Amsterdam. One should notice that this range is based on maximum take off weight, with normal fuel tanks, but under ideal flight conditions. Furthermore, this maximum range is based on an entire performed mission, including a 30 [km] flight to a hospital and the return to the base without refueling possibilities in between.

The rescue time is 1 [h] and [5 min] at the range border lines indicated on the range map. However, a distance of 30 [km] and 50 [km] to the emergency location would be more frequent in the Netherlands. For that, a rescue time of 12:22 [min] and 19:50 [min] would be required respectively. For the requirement check, a rescue time of 36:37 [min] would be required to get to an emergency area at 110 [km] distance. The requirement was set to less than 30 [min], meaning that the goal time can not be satisfied. Suggestions for improvements will be given in Section 12.1.

7.2 Payload-Range Diagram

The range of the vehicle depends on the weight it has to carry during the mission. The weight that it can cary consists of the payload weight and fuel weight. It would be ideal to have an infinite range by just increasing the fuel weight all the time. However, this is a constraint by the MTOW that can not be exceeded. The range for different combinations of payload and fuel weight can be presented in a payload-range diagram. First it should be calculated what the ranges of the vehicle will be when the

Figure 7.4: Range Map

maximum payload of 485 [kg] is on board. Evidently, the range is zero when there is no fuel on board to operate the engines. When more fuel is loaded, the range will increase linearly until the maximum fuel weight is reached. This maximum fuel weight equals 311.5 [kg] according to Section 4 on propulsion.

For nominal conditions the total weight of the vehicle equals the maximum take-off weight. The range at this point is determined to equal 442 [km], as already calculated in Subsection 7.1.11. There are two possibilities to further increase the range: either decrease the payload weight whilst keeping the fuel weight constant or increase the fuel weight by placing fuel tanks instead of payload. First the situation where the fuel stays constant will be explained. After that the situation where fuel tanks are placed in will be described.

7.2.1 Constant Fuel Weight

This section explains how the range is found for different payload weights and a constant fuel weight. The maximum range will be achieved when the payload weight equals zero. The new take-off weight is found using Equation (7.25).

$$\text{TOW} = \text{MTOW} - W_{\text{PL}} - W_{\text{crew}} = 1365 \text{ [kg]} \tag{7.25}$$

This weight is then put in the ducted fan program that has been discussed in Subsection 4.1 to get a new power required during cruise, which equals 264.6 [kW] for the two ducted fans together. The loss in thrust at higher altitudes of 70% should however still be taken into account. The final power required is calculated with Equation (7.26).

$$P_{\text{range,max}} = \frac{264.6}{0.7} = 378 \text{ [kW]} \tag{7.26}$$

The fuel flow during cruise is calculated using Equation (7.27).

$$\dot{m}_{\text{fuel}} = (\text{SFC} \cdot P_{\text{range,max}}) = (0.274 \cdot 382) = 104.7 \left[\frac{\text{kg}}{\text{h}}\right] \tag{7.27}$$

Where SFC is equal to 0.274 $\left[\frac{\text{kg}}{\text{kW}\cdot\text{h}}\right]$ as determined in Section 4.

The new total cruise endurance of the vehicle can now easily be calculated using Equation (7.28).

$$E = \frac{W_{\text{F,max}}}{\dot{m}_{\text{fuel}}} = \frac{311.5}{104.7} = 2.97 \text{ [h]} \tag{7.28}$$

The maximum range can now be computed with Equation (7.29), where the cruise speed still equals 200 $\left[\frac{\text{km}}{\text{h}}\right]$.

$$R_{\text{max}} = E \cdot v_0 = 595 \text{ [km]} \tag{7.29}$$

This range is only for a one way trip, so when a return trip has to be flown the range halves. Everything is known at this point to create the payload-range diagram which can be seen in Figure 7.5.

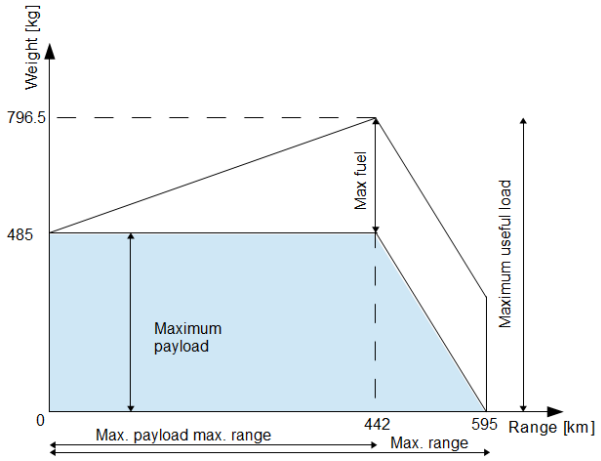

Figure 7.5: Payload-Range diagram of the eGyro for the EMS mission

7.2.2 Additional Fuel Tanks

This section explains how the range is found for different payload weights when the payload weight is replaced by additional fuel tanks. In this situation the maximum range will also be achieved when the payload weight equals zero. However, the new take-off weight is in this case equal to the MTOW, because the weight of the payload is fully replaced by fuel tanks.

As a result of the unchanged MTOW, which equals 1850 [kg], the power required during cruise equals 512 [kg], as calculated before in Section 4. Note that the loss in power on higher altitudes of 70% is already included in this value.

The fuel flow during cruise is calculated using Equation (7.30).

$$\dot{m}_{\text{fuel},2} = (\text{SFC} \cdot P_{\text{range,max}}) = (0.274 \cdot 512) = 140.29 \left[\frac{\text{kg}}{\text{h}}\right] \tag{7.30}$$

wher all parameters in this equation have the same meaning as in the previous section.

The fuel weight for this situation is calculated using Equation (7.31).

$$W_{\text{F}} = W_{\text{F},1} + W_{\text{PL}} - W_{\text{tank}} = 311.5 + 485 - 35 = 761.5 \text{ [kg]} \tag{7.31}$$

Since the additional fuel is loaded instead of the payload weight, the total fuel weight equals the old fuel weight plus the fuel weight. However, the weight of the tank itself is also taken into account and estimated to be 35 [kg].

The new total cruise endurance of the vehicle can now easily be calculated using Equation (7.32).

$$E = \frac{W_{\text{F}}}{\dot{m}_{\text{fuel},2}} = \frac{761.5}{140.29} = 5.43 \text{ [h]} \tag{7.32}$$

The maximum range can be calculated with Equation (7.33).

$$R_{\text{max}} = E \cdot v_0 = 1086 \text{ [km]} \tag{7.33}$$

Here, the cruise speed still equals 200 $\left[\frac{\text{km}}{\text{h}}\right]$. Everything is known at this point to create the Payload-Range diagram, which can be seen in Figure 7.6

7.3 Performance Diagrams

The performance of the eGyro can be shown graphically with the power curves, flight envelope and climb performance graphs.

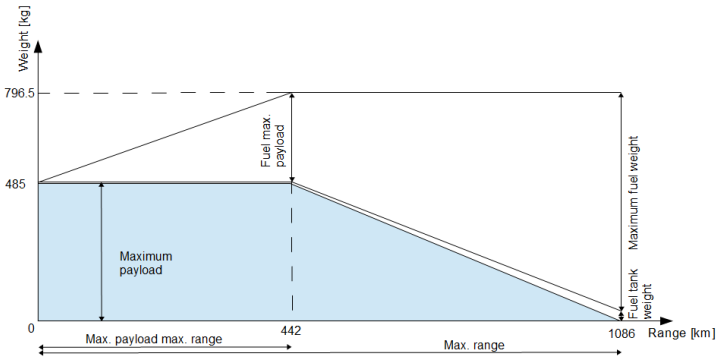

Figure 7.6: Payload-Range diagram of the eGyro for the EMS mission using additional fuel tanks

7.3.1 Power curves

The power curves can be divided in power available and power required during cruise. The total power required curve consists of three parts; profile power, induced power and parasitic power. The relation for the profile power can be seen in Equation (7.34). Where C_{Dp} is determined using a regression line in MATLAB with the C_{Dp} value for different flapping angles.

$$P_{\text{pro}} = \frac{\sigma \cdot C_{d,\text{p}}}{8} \cdot \rho \cdot (\omega_{\text{r}} \cdot r_{\text{r}})^3 \cdot \pi \cdot {r_{\text{r}}}^2 \cdot \left(1 + 4.665 \cdot \left(\frac{V}{\omega_{\text{r}} \cdot r_{\text{r}}}\right)^2\right) \tag{7.34}$$

The induced power required is given by Equation (7.35), where the rotor induced loss factor k equals 1.2 and the induced velocity v_i is determined using the graph in Figure 7.7, were the low speed flight is used. In which v_i is determined by Equation (7.36).

$$P_{\text{i}} = k \cdot T \cdot v_i \tag{7.35}$$

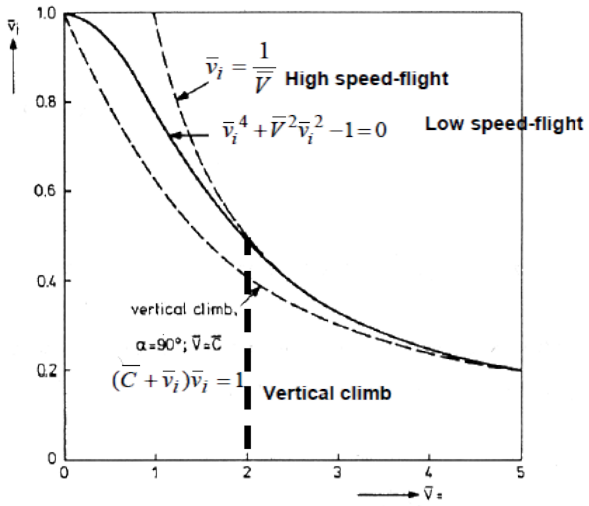

Figure 7.7: Induced velocity as function of cruise speed [14]

v_{ih} from the figure above is equal to Equation (7.36).

$$v_{ih} = \sqrt{\frac{\text{MTOW}}{2 \cdot \rho \cdot \pi \cdot {r_{\text{r}}}^2}} \tag{7.36}$$

Finally, the parasitic power is determined using Equation (7.37).

$$P_{\text{par}} = 0.5 \cdot \rho \cdot V^3 \cdot C_d \cdot S \tag{7.37}$$

The plot of each separate power required including the total power required of the three contributors at sea level can be seen in Figure 7.8.

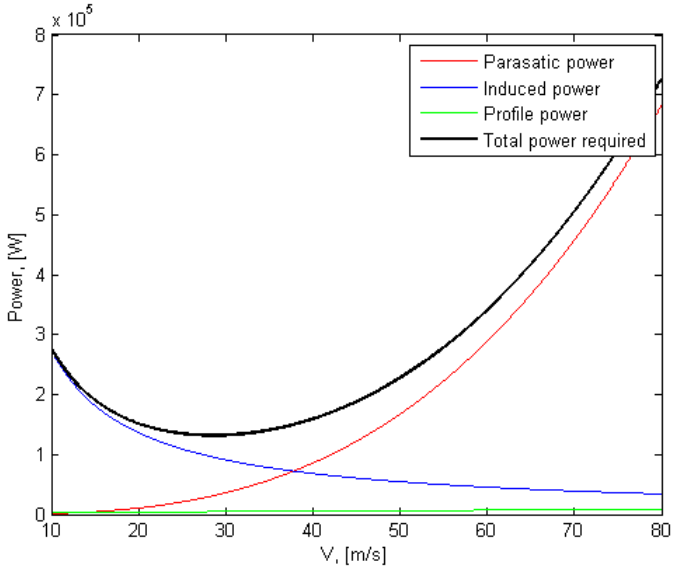

Figure 7.8: Profile, induced, parasitic and total power required against velocity

The power required curve changes when the altitude increases because of the decrease of density with altitude. The same holds for the power available, where the relation in Equation (7.38) has been determined.

$$P_{\mathrm{a}} = P_{\mathrm{a0}} \cdot \eta \cdot \frac{\rho}{\rho_0}^{1.28} \tag{7.38}$$

Where, η represents the generator efficiency, which is equal to 90% and the power 1.28 is calculated assuming that the power loss factor at an altitude of 2000 [m] should be 0.7 which was provided by the tutor as a conventional value. The power curves for different altitudes can be seen in Figure 7.9.

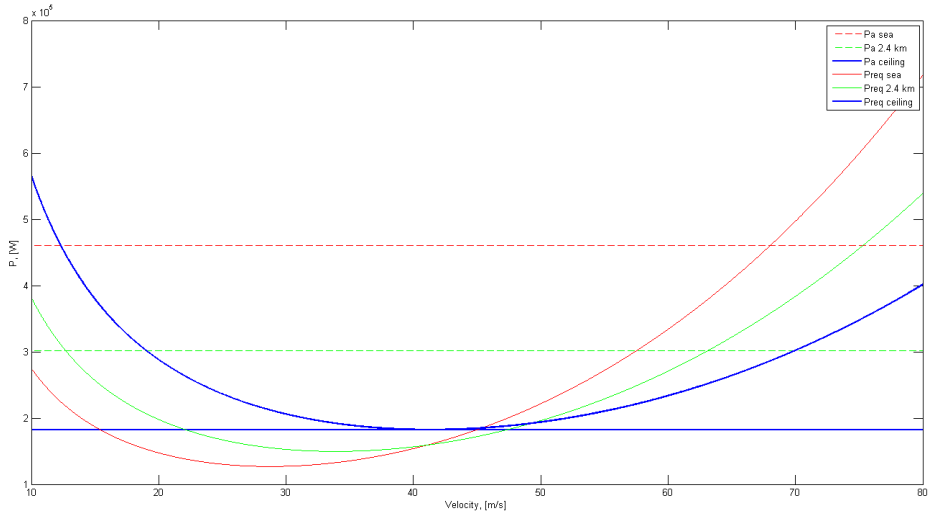

Figure 7.9: Total power required against velocity for different altitudes

7.3.2 Flight Envelope

With the power curves for different altitudes the first two lines of the flight envelope can be computed. As can be seen in Figure 7.9 the power available and required curves generally intersect at two points as depicted by the curve for 2.4 [km] altitude. The first intersection represents the minimum velocity and the second one the maximum velocity. The two come closer when the altitude is increasing until there is only one intersection. The altitude at which this occurs is called the ceiling and the corresponding power can be seen in Figure 7.9. The other limit line in the flight envelope is the maximum cruise speed constrained by the maximum tip speed of the rotor blades. The formula for maximum tip speed can be seen in Equation (7.39).

$$v_{\text{tipmax}} = (a \cdot M_{\text{max}}) - v_0 \tag{7.39}$$

M_{max} is the maximum Mach number that the blade is allowed to experience and equals 0.95, while a is a function of height and therefore temperature according to Equation (7.40).

$$a = \sqrt{\gamma \cdot \mathcal{T} \cdot R} \tag{7.40}$$

The final flight envelope can now be computed and is displayed in Figure 7.10.

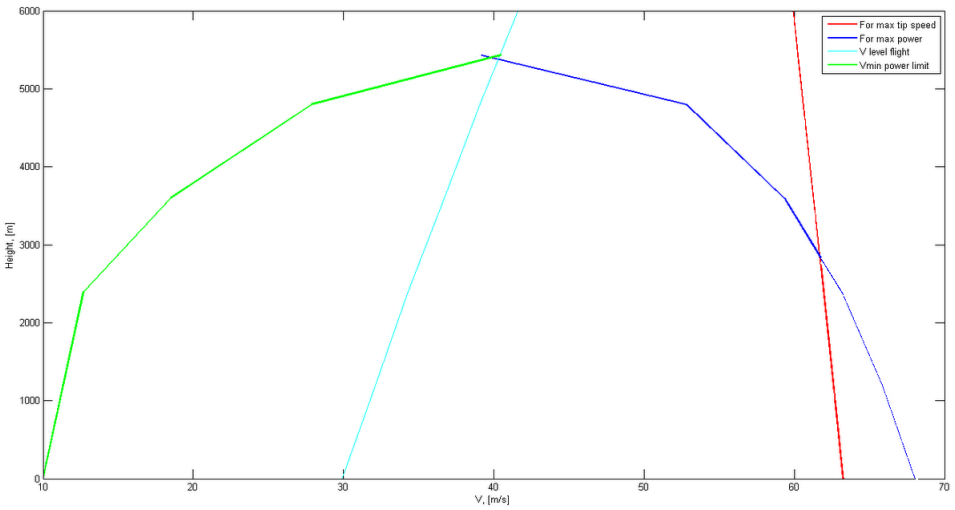

Figure 7.10: Flight envelope

It can be seen that the maximum velocity is limited by the maximum tip speed up until 2875 [m] and from then on by the maximum power. The point where the maximum and minimum velocities intersect is called the ceiling and equals 5430 [m] as can be derived from the figure. An extra line is plotted to show the required speed to remain in level flight for each altitude but that is not a limit for the flight envelope.

7.3.3 Climb rate

Using the power curves the climb rates can be determined as a function of velocity for different heights. The climb rate equals Equation (7.41).

$$\text{RoC} = \frac{P_{\text{a}} - P_{\text{r}}}{\text{MTOW}} \tag{7.41}$$

As can be seen in Figure 7.9 the climb rates decrease when the speed is getting closer to the maximum or minimum speed. This can be clearly seen in Figure 7.11.

It can be seen that for each altitude the climb rate is maximum for a certain altitude. However when the altitude increases the climb rates decrease until the climb rate is equal to 0. The maximum rates of climb as a function of the altitude are shown in Figure 7.12.

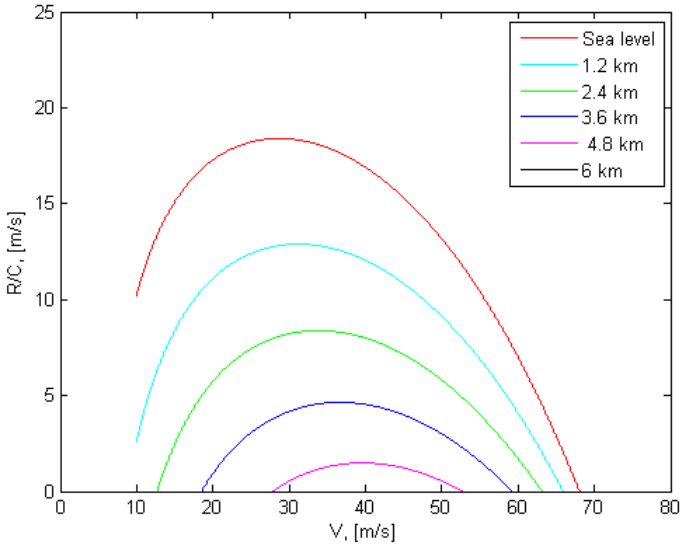

Figure 7.11: Rate of climbs for different velocities

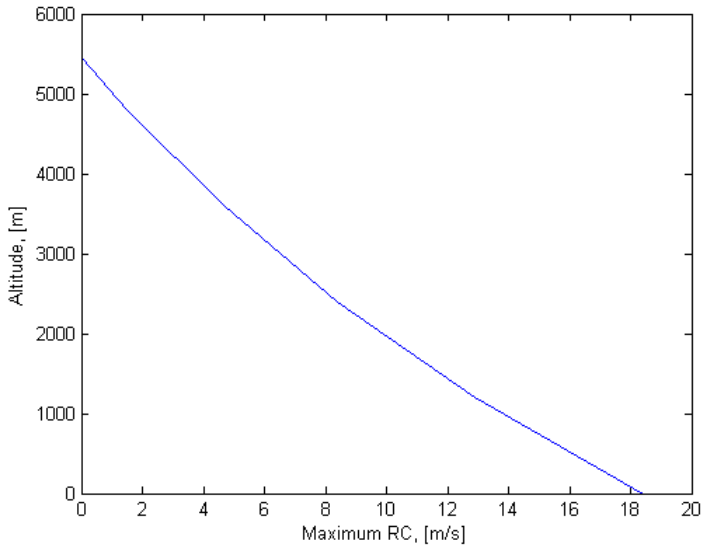

Figure 7.12: Maximum rate of climb against velocity

7.4 Load Factors

The vehicle performs different maneuvers during each mission, such that different loads act on it. These loads are generally expressed in load factors, which represent the load during a maneuver in relation to the gravitational acceleration. In other words, the load factor equals the amount of g-forces that are encountered during the maneuver. To determine the design load factors of the eGyro, several maximum load factors for different flight conditions are used [39]. The load factors for an auto-rotation flight condition are higher compared to a level flight condition. For a cyclic-pitch pull-up, the difference equals 0.17. In Table 7.1 some maximum load factors in auto-rotation conditions can be seen.

The load factors are all around 2.5. Since the eGyro is an unorthodox design, the values are probably somewhat higher and therefore a design load factor of 3 is chosen for the structural analysis of the concept. Gust loads are less critical compared to maneuver loads. To achieve a load factor of 2.5, a gust velocity of 18.3 $\left[\frac{\mathrm{m}}{\mathrm{s}}\right]$ is required. Usually a load factor due to gusts equals 1.9. It is found that the maximum

Table 7.1: Maximum load factors of the eGyro

Maneuver	Maximum load factor	Flight condition
Cyclic-pitch pull-up	2.55	Auto-rotation at 129 $\left[\frac{\text{km}}{\text{h}}\right]$
Cyclic-pitch pull-up	2.52	50 [deg] dive in auto-rotation

acceleration in an abrupt turn at a speed of 202 $\left[\frac{\text{km}}{\text{h}}\right]$, which is almost equal to the cruise speed of the eGyro, equals 4.3 times the gravitational acceleration [40]. Since this maneuver is not very likely to happen during the mission, the 4.3 times the gravitational acceleration is taken as a limit load. The vehicle is designed with a safety factor of 1.5 on top of the design limit load factor of 3. This means that it will be capable of withstanding a load of 4.5 once in its life cycle without resulting in a failure of any system.

7.5 Noise

This section describes the determination of the produced noise by the eGyro vehicle. The noise that the vehicle generates is produced by several components. The main contributors to the noise are the rotor and ducted fans. The rotor noise can be divided in rotor rotational noise and rotor vortex noise. The Sound Pressure Levels (SPLs) are calculated using the steps explained in a paper on aerodynamic noise from propellers [41] and eventually the Effective Perceived Noise Levels (EPNLs) is calculated with the steps explained in a paper on aircraft noise [42].

7.5.1 Rotor Rotational Noise

For the rotor rotational noise, a rotational noise spectrum is created for a certain point on the ground, which is described in this subsection.

Noise Spectrum

First, the distance from the vehicle to the point on the ground is determined. Secondly, the rotational Mach number is calculated using Equation (7.42).

$$M = \frac{0.8 \cdot \omega_{\text{r}} \cdot r_{\text{r}}}{a} = 0.35 \tag{7.42}$$

From this equation, the effective rotational Mach number is calculated using Equation (7.43).

$$M_{\text{E}} = \frac{M}{1 - M_{\text{F}} \cdot \cos(\theta^p)} = 0.4 \tag{7.43}$$

Where M_{F} represents flight Mach number and θ^p the angle between the flight direction and the line that connects the vehicle with the ground point. The angle θ between the rotor plane and the line that connects the vehicle with the field point is determined using Equation (7.44), where the disk incidence angle i_{d} is one of the inputs. The x,y and z values are the coordinates of the ground point with reference to the vehicle.

$$\theta = \tan^{-1}\left(\frac{z}{\sqrt{x^2+y^2}}\right) - i_{\text{d}}\left(\frac{x}{\sqrt{x^2+y^2}}\right) = 32.5 \text{ [deg]} \tag{7.44}$$

The values for M_{E} and θ are then used to obtain values for the harmonic SPLs I_N from [41]. These values should be corrected using Equation (7.45).

$$\mathrm{SPL_N} = I_N + 11 + 10 \cdot \log\left(\frac{T}{r^2} \cdot \mathrm{DL}\right) \text{ [dB]} \tag{7.45}$$

The fundamental frequency can be computed using the values calculated above using Equation (7.46).

$$f_{\mathrm{f}} = \frac{n \cdot B}{2 \cdot \pi \cdot (1 - M_{\mathrm{E}} \cos\theta)} = 16.14 \text{ [Hz]} \tag{7.46}$$

This fundamental frequency is multiplied by the harmonic numbers to have the SPLs as a function of frequency. This octave band is plotted in Figure 7.13.

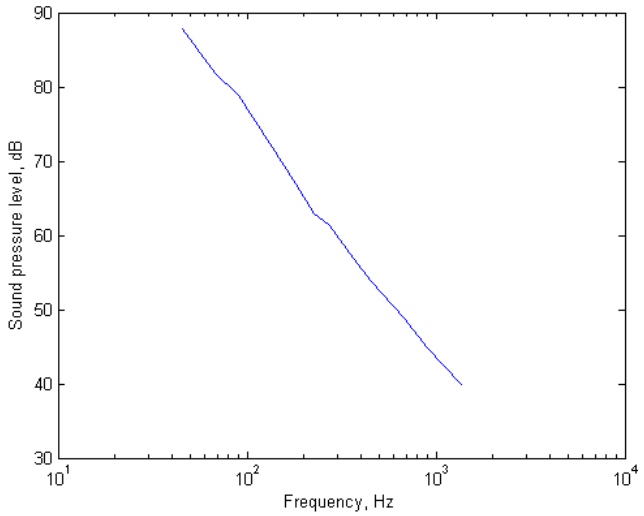

Figure 7.13: Octave band sound pressure level

Maximum Perceived Noise

A maximum perceived noise level can be computed from this octave band using the following steps. First the octave band of the SPL is divided in 24 different 1/3 octave bands and is then converted to perceived noise by means of a Noy table. The definition of the bands for frequencies ranging from 50 to 10000 [Hz] can be seen in Table 7.2 [43]. For these frequencies and the corresponding SPL, the corresponding Noy values can be read from the Noy table [42].

These Noy values are combined and converted to a Perceived Noise Level (PNL). For combining the Noy values Equation (7.47) is used.

$$N = 0.85 \cdot n_{max} + 0.15 \sum_{i=1}^{24} n(i) = 18.97 \tag{7.47}$$

Where $n(i)$ are all the Noy values for each i 1/3 octave band. With this value as input, the equivalent PNL at 1000 [Hz] frequency is determined using Equation (7.48).

$$\mathrm{PNL} = 40 + \frac{10}{\log(2)} \cdot \log(N) = 82.45 \text{ [dB]} \tag{7.48}$$

The next thing that has to be done is the calculation of the tone correction to account for subjective response to the presence of spectral irregularities. This is done using the following approach:

Step 1 The slope of the SPLs is calculated for the octave bands from the third one on, using Equation (7.49).

$$s = \mathrm{SPL}(i) - \mathrm{SPL}(i-1) \tag{7.49}$$

Table 7.2: Definition of one-third octave-bands

One-Third Octave-Band Number	Nominal Center Frequency [Hz]	One-Third Octave-Band Number	Nominal Center Frequency [Hz]
17	50	29	800
18	63	30	1000
19	80	31	1250
20	100	32	1600
21	125	33	2000
22	160	34	2500
23	200	35	3150
24	250	36	4000
25	315	37	5000
26	400	38	6300
27	500	39	8000
28	630	40	10000

Step 2 Determine the values of the slope where the absolute value of the change in slope is larger than five, as can be seen in Equation (7.50).

$$|\Delta s(i)| = |s(i) - s(i-1)| > 5 \tag{7.50}$$

Step 3 Determine whether the values of Step 2 are positive, zero or negative.

Step 4 The SPLs at the frequency where the slope is too large have to be changed using the method in Equation (7.51).

$$\mathrm{SPL}'(i) = \frac{1}{2} \cdot (\mathrm{SPL}(i-1) + \mathrm{SPL}(i+1)) \tag{7.51}$$

Step 5 New slopes have to be computed for these new SPLs with the relation in Equation (7.52).

$$s' = \mathrm{SPL}'(i) - \mathrm{SPL}'(i-1) \tag{7.52}$$

Step 6 The arithmetic average of three adjacent slopes can be computed now with Equation (7.53).

$$\bar{s}(i) = \frac{1}{3}\left(s'(i) + s'(i+1) + s'(i+2)\right) \tag{7.53}$$

Step 7 Compute the final 1/3 octave band SPLs by including the arithmetic averages as stated in Equation (7.54).

$$\mathrm{SPL}''(i) = \mathrm{SPL}''(i-1) + \bar{s}(i-1) \tag{7.54}$$

Step 8 The difference between this final background SPL and the original SPL is calculated using Equation (7.55). Only the values that are greater or equal to one are noted, because that ones are too far of.

$$F(i) = \mathrm{SPL}(i) - \mathrm{SPL}''(i) \tag{7.55}$$

Step 9 For each relevant octave band the tone correction factor is determined with $F(i)$ from Table 7.3.

Table 7.3: Tone Correction Factor [42]

Frequency f [Hz]	Level Difference F [dB]	Tone Correction C [dB]
$450 \leq f \leq 500$	$1.5 \leq F < 3$	$F/3 - 0.5$
	$3 \leq F < 20$	$F/6$
	$20 \leq F$	$3\frac{1}{3}$
$500 \leq f \leq 5000$	$1.5 \leq F < 3$	$2 \cdot F/3 - 0.5$
	$3 \leq F < 20$	$F/3$
	$20 \leq F$	$6\frac{2}{3}$
$5000 \leq f \leq 10000$	$1.5 \leq F < 3$	$F/3 - 0.5$
	$3 \leq F < 20$	$F/6$
	$20 \leq F$	$3\frac{1}{3}$

Step 10 Determine the largest correction factor and add this one to the PNL and arrive at the maximum value of the tone corrected PNL for rotational noise, which equals 85.79 [dB].

7.5.2 Rotor Vortex Noise

The overall SPL of the vortex noise is also determined using a stepwise method. The first step is the determination of the linear velocity of the 0.7 radius section of the rotor using Equation (7.56).

$$V_{0.7} = 0.7 \cdot \frac{n \cdot \pi \cdot D}{60} = 104 \ \left[\frac{\mathrm{m}}{\mathrm{s}}\right] \tag{7.56}$$

The blade plan form area A_b is calculated using Equation (7.57), where n_{blades} is the number of rotor blades, r_{r} the radius and c the chord of the rotor blades.

$$A_{\mathrm{b}} = n_{\mathrm{blades}} \cdot r_{\mathrm{r}} \cdot c = 2.21 \ [\mathrm{m}^2] \tag{7.57}$$

The overall SPL is determined at a distance of 300 [m], which is a common value for helicopter noise analysis. First, the SPL at a 91 [m] distance has to be calculated using Equation (7.58).

$$\mathrm{SPL}_{91} = 10 \cdot (2 \cdot \log(V_{0.7}) + 2 \cdot \log(T) - \log(A_{\mathrm{b}}) - 3.57) = 73.25 \ [\mathrm{dB}] \tag{7.58}$$

From this value the SPL at the 300 [m] distance can be determined with Equation (7.59).

$$\mathrm{SPL}_{300} = \mathrm{SPL}_{91} - 20 \cdot \log\left(300/91\right) = 62.8 \ [\mathrm{dB}] \tag{7.59}$$

Finally, an approximation to the vortex spectrum shape is determined. First, the peak frequency is calculated using Equation (7.60).

$$f = \frac{V_{0.7} \cdot St}{h} = 256.36 \ [\mathrm{Hz}] \tag{7.60}$$

Here, St represents the Strouhal number, which can be taken to equal 0.28 according to [41]. The projected blade thickness $t_{\mathrm{projected}}$ is calculated with Equation (7.61).

$$t_{\mathrm{projected}} = t_{\mathrm{blade}} \cdot \cos(\alpha) + c \cdot \sin(\alpha) = 0.11 \ [\mathrm{m}] \tag{7.61}$$

Using the values for the overall SPL and peak frequency, the noise spectrum is constructed as can be seen in Figure 7.14.

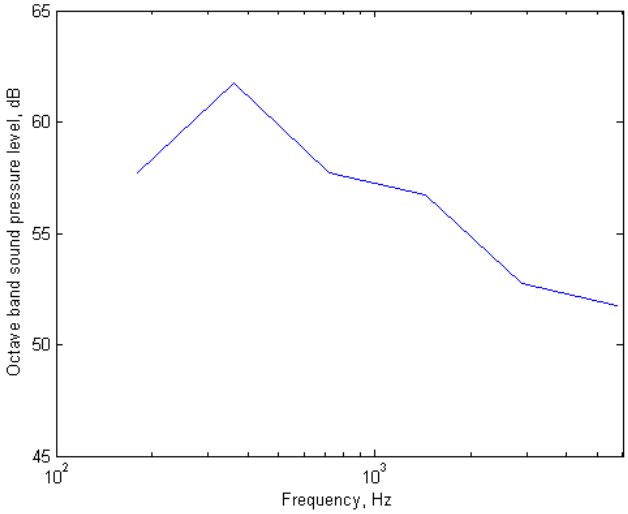

Figure 7.14: Octave band sound pressure level vortex noise

Maximum Perceived Noise

From above noise spectrum a maximum PNL can be determined in the same way as in Section 7.5.1.

The combined Noy value for the rotor vortex noise is found to be 13.64 and the PNL then follows from Equation (7.62):

$$\mathrm{PNL} = 40 + \frac{10}{\log(2)} \cdot \log(13.64) = 77.7 \text{ [dB]} \tag{7.62}$$

Following the same steps as in Section 7.5.1, the maximum value of the tone corrected PNL is determined with Equation (7.63).

$$\mathrm{PNL_{TM}} = 77.7 + 2.85 = 80.55 \text{ [dB]} \tag{7.63}$$

7.5.3 Fan Noise

The fan noise is determined from a set of geometric parameters and operating conditions in a stepwise manner. The front ducted fans have other parameters than the aft ducted fans. However, the calculation method is the same. Therefore, only the method for the aft ducted fans is explained below and the noise emissions of the front ducted fans are computed the same way. First, the rotor annulus area A_a has to be calculated using Equation (7.64).

$$A_\mathrm{a} = \frac{\pi}{4} \cdot {r_\mathrm{f}}^2 \cdot \left(1 - \left(\frac{r_\mathrm{f}}{r_\mathrm{h}}\right)^2\right) = 1.46 \text{ [m}^2\text{]} \tag{7.64}$$

The energy flux per unit area can then be computed using Equation (7.65).

$$E = \frac{H_t \cdot \dot{m}}{A_\mathrm{a}} = 1.97 \cdot 10^3 \left[\frac{\mathrm{kWh}}{\mathrm{s} \cdot \mathrm{m}^2}\right] \tag{7.65}$$

Where, the total enthalpy H_t is assumed to be equal to 0.08 $\left[\frac{\mathrm{kWh}}{\mathrm{kg}}\right]$ the same value as in the paper [41].

From Figure 7.15, a normalized overall sound power can be determined for the above calculated energy flux. Hence, Equation (7.66) holds.

$$\mathrm{PWL} - 10 \cdot \log\left(\frac{A_\mathrm{a} \cdot n_\mathrm{rpm}}{B} \cdot \left(\frac{r_\mathrm{f}}{r_\mathrm{h}}\right)^2\right) = 120 \text{ [dB]} \tag{7.66}$$

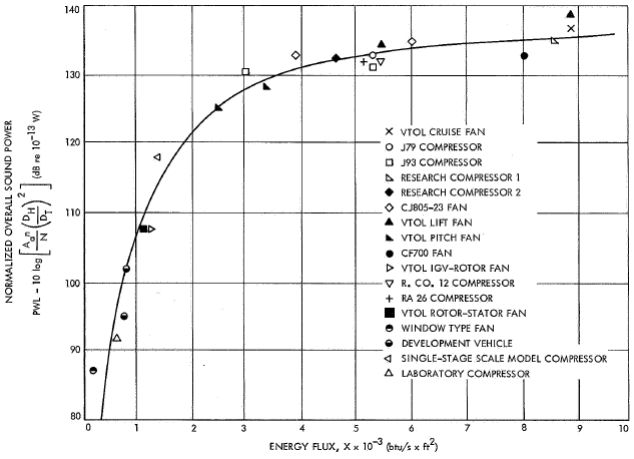

Figure 7.15: Normalized overall power of compressor and fan noise [41]

The PWL can be obtained from the calculated energy flux and the corresponding normalized overall sound power, as seen in Equation (7.67).

$$\mathrm{PWL} = 10 \cdot \log\left(\frac{A_\mathrm{a} \cdot n_\mathrm{rpm}}{B} \cdot \left(\frac{r_\mathrm{f}}{r_\mathrm{h}}\right)^2\right) + 120 = 128.72 \text{ [dB]} \tag{7.67}$$

From the overall sound power determined above, a sound power spectrum can be generated using the graph in Figure 7.16.

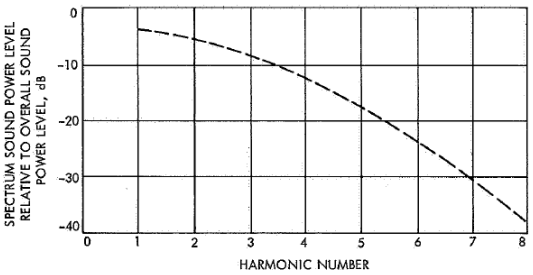

Figure 7.16: Normalized power spectrum of compressor and fan noise [41]

In that way, an octave band spectrum can be made by computing the SPLs for each frequency. For the first and second harmonies, this equals to Equation (7.68) and Equation (7.69) respectively.

$$\text{First harmonic} = \mathrm{PWL} - 3.5 = 125.22 \text{ [dB]} \tag{7.68}$$

$$\text{Second harmonic} = \mathrm{PWL} - 5.5 = 123.22 \text{ [dB]} \tag{7.69}$$

The final octave bands for the aft and front ducted fans can be seen in Figures 7.17 and 7.18, respectively.

Maximum Perceived Noise

From above noise spectra, the maximum PNLs can be determined in the same way as in Section 7.5.1.

The combined Noy value for the aft and front ducted fan noises are determined to be 21.2 and 23.9. The PNLs then follows from Equations (7.70) and (7.71).

$$\mathrm{PNL}_\mathrm{aft} = 40 + \frac{10}{\log(2)} \cdot \log(21.2) = 84.1 \text{ [dB]} \tag{7.70}$$

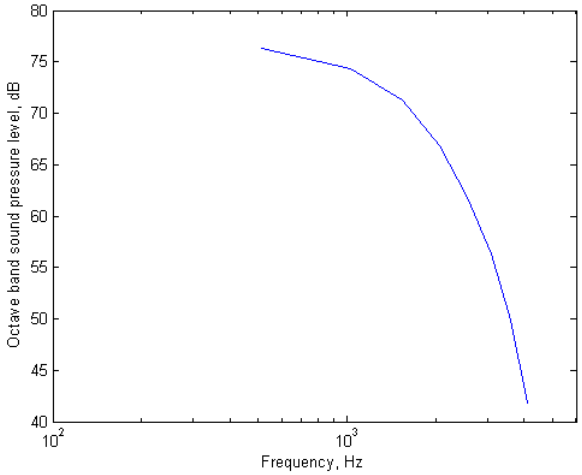

Figure 7.17: Octave band sound pressure level

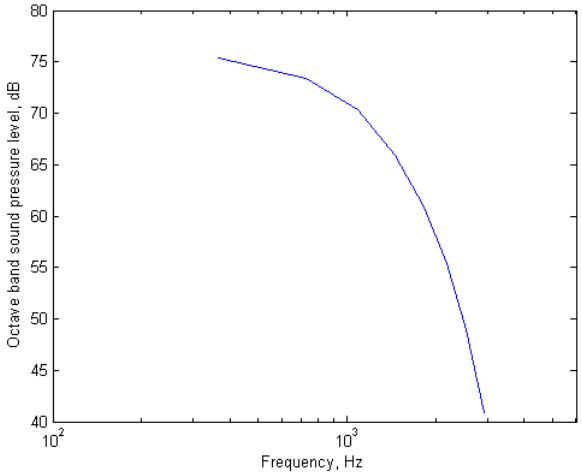

Figure 7.18: Octave band sound pressure level

$$\mathrm{PNL}_{\mathrm{front}} = 40 + \frac{10}{\log(2)} \cdot \log(23.9) = 85.8 \text{ [dB]} \tag{7.71}$$

Following the same steps as in 7.5.1, the maximum values of the tone corrected PNLs are determined with Equations (7.72) and (7.73).

$$\mathrm{PNL}_{\mathrm{TM,aft}} = 84.08 + 2.16 = 86.24 \text{ [dB]} \tag{7.72}$$

$$\mathrm{PNL}_{\mathrm{TM,front}} = 85.8 + 2.84 = 88.65 \text{ [dB]} \tag{7.73}$$

7.5.4 Total EPNL

The total EPNL can now be computed using the different contributions in the cruise and VTOL phase, which will result in two different noise levels. The formulas for the calculation of the EPNL during cruise are described in Equations (7.74) and (7.75).

$$\mathrm{EPNL}_{\mathrm{cruise}} = 10 \cdot \log\left(\frac{\mathrm{PNL}_{\mathrm{TM,rotational}}}{10} + \frac{\mathrm{PNL}_{\mathrm{TM,vortex}}}{10} + 2 \cdot \frac{\mathrm{PNL}_{\mathrm{TM,aft}}}{10}\right) - 13 = 78.25 \text{ [dB]} \tag{7.74}$$

$$\mathrm{EPNL_{VTOL}} = 10 \cdot \log\left(2 \cdot \frac{\mathrm{PNL_{TM,front}}}{10} + 2 \cdot \frac{\mathrm{PNL_{TM,aft}}}{10}\right) - 13 = 80.64 \text{ [dB]} \tag{7.75}$$

These values are only 40% of the EPNLs of the current EMS vehicle, the EC135 [44].

7.6 Emissions

The emissions produced by the eGyro are calculated in this section. After selecting the Arriel 2C2 turboshaft engine, the relevant engine parameters for the calculations are found in the [15] and [45]. The following method and the following calculations are based on [45].

The emissions are based on reference data, which is collected for several engine types. A direct relation between the shaft horse powers (SHP), nitrogen oxide (NOx), hydrocarbons (HC), carbon monoxide (CO) and non-volatile particles (PM) is used to find the values for each of these pollutant substances. The emissions are calculated for the cruise and the VTOL phase respectively. However, for the VTOL phase of the mission, an estimation of the emissions has to be used, since the paper approximations are only valid for high power settings, while the engine is only running in idle during the VTOL phases. For cruise, the emission factor for every particle is first calculated using Equation (7.76).

$$\text{Emission factor} = a1 \cdot ({P_\mathrm{a}}^2)^{a2} + b1 \cdot {P_\mathrm{a}}^{b2} + c \tag{7.76}$$

The constants a1, a2, b1, b2 and c vary for every particle type and can be found in Table 7.4 shown below. Finally the burnt amount of each particle can be calculated with the cruise time, the cruise mass flow and the particle emission factor, as can be seen in Equation (7.77).

$$\text{Particles} = 60 \cdot T \cdot \dot{m}_\mathrm{cruise} \cdot \text{Emission factor} \tag{7.77}$$

The emission values of each particle are stated in Table 7.4 below, together with the emission in $\left[\frac{\mathrm{kg}}{\mathrm{min}}\right]$.

Table 7.4: Emissions

Particle Type	**a1**	**a2**	**b1**	**b2**	**c**	**Emissions total [kg]**	**Emission factor $\left[\frac{\mathrm{g}}{\mathrm{km}}\right]$**	**Emissions total [kg]**
NOx	0	1	0.2113	0.5677	0	1.36	8.6	0.04
HC	0	1	3819	-1.0801	0	0.53	3.3	0.016
CO	0	1	5660	-1.11	0	0.64	4.0	0.019
PM	$-4.8 \cdot 10^{-8}$	1	$2.3664 \cdot 10^{-4}$	1	0.1056	0.04	0.25	$1.2 \cdot 10^{-3}$

The total emission values in [kg] are calculated from the type of mission, which are mentioned in the requirements. It involves a mission with the three VTOL operations indicated in the mission profile, with a mission distance of 110 [km] and a optional flight to the nearest hospital of 30 [km]. For the VTOL emission, it is assumed that the amount of burnt particles equals 15 % of the full power emissions. This value stems from the idle power estimation percentage, chosen during the VTOL phase.

8 Materials & Structures

A structural analysis and a material selection is done for the eGyro. This chapter discusses six important structural parts of the vehicle: the rotor, the rotor mount, the rotor hub, the airframe, the tail beam and the landing gear. For each of these parts an appropriate material selection or recommendation is done, based on the load calculations on the subparts.

8.1 Rotor Blade Structural Analysis

For the rotor design, the rotor blades are considered as a rectangular box with a circular leading edge and a triangular trailing edge. It is assumed that the leading edge and the trailing edge are not carrying any loads. Figure 8.1 shows the profile view of one blade.

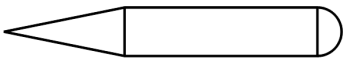

Figure 8.1: Simplified rotor profile for eGyro

8.1.1 Rotor Blade Analysis Method

Since it is assumed that only the rectangular box in Figure 8.1 carries the loads, the analysis of this structure is straightforward. It is assumed that the lift on the rotor blades is a distributed load along the blade length. The distributed load w is calculated using Equation 8.1.

$$w = \frac{\text{MTOW} \cdot g_0}{n_{\text{blades}} \cdot r_{\text{r}}} \tag{8.1}$$

Where n_{blades} is the number of blades of the rotor and r_{r} is the rotor radius. The load acts on the quarter chord line of the box, inducing a bending moment and a torque. At last, a centrifugal force is acting on the box when the rotor is turning. In general, the centrifugal force can be calculated using Equation 8.2

$$F_{\text{centrifugal}} = \frac{m \cdot V^2}{r} \tag{8.2}$$

With m the mass of the rotating object. The speed V equals $\omega_{\text{r}} \cdot r_{\text{r}}$, such that the equation for the centrifugal force for the rotor blades becomes equal to Equation 8.3.

$$F_{\text{centrifugal}} = m \cdot r_{\text{r}} \cdot {\omega_{\text{r}}}^2 \tag{8.3}$$

The method that is used for the calculation of the stresses in the box is based on structural idealization using stress-carrying booms and shear-carrying skins [46]. This method is applied for the calculations in the script that was created in for this purpose. The rectangular cross section of the box is divided into booms and skins as shown in Figure 8.2.

The distance between each boom is equal to 1 [mm], such that the number of booms that will be used depends on the size of the box. The length of the box is divided into 500 elements from tip to root. The calculations on the stresses per element are conducted from tip to root. This is due to the fact that the moment of the tip element has an influence on the moment of the root element, and not the other way around. To perform these calculations, a MATLAB [13] script has been written to calculate and plot all stresses along the beam.

For each element, the distributed lift force is converted to a point load in the middle of the element. This force is of course pointed upwards. The gravitational force of each element is subtracted from this lift force to get the resultant force per element. The bending moment is then calculated with this resultant

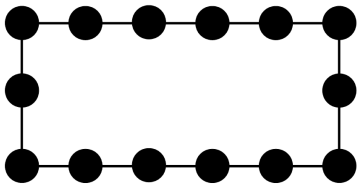

Figure 8.2: A rotor box cut-out with the boom representation

force multiplied by the moment arm. At last the torsion is calculated by multiplying the point load with the torsion moment arm. Figure 8.3 shows the side and front view of an element including an explanation of the loads and moment arms. c_{box} is the chord of the box and h_{box} is the height of the box.

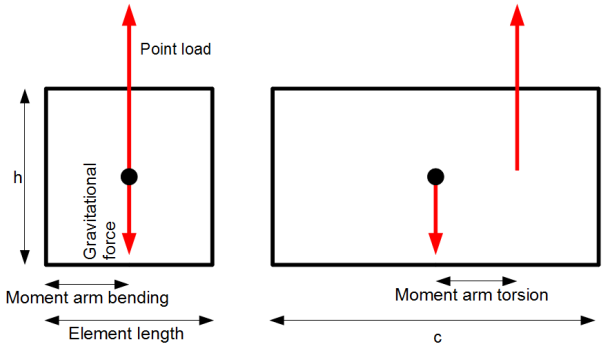

Figure 8.3: Side and front view of one of the 500 elements in which the rotor box is divided including forces

All forces are assumed to be transferred to the root side of each element. Each element has an equal thickness at all sides. The calculation is performed starting with the first element at the tip. The moment and the torque on the element are calculated as explained before. Next, the weight of the element is calculated using the thickness, the beam dimensions and the material density. The density is 1800 $\left[\frac{\text{kg}}{\text{m}^3}\right]$ since the material used for the rotor is a CFRP called T700S, with a maximum tensile strength of 2550 [MPa] and a maximum compressive strength of 1470 [MPa] [47]. The selection of this material will be elaborated on in Section 8.1.2. The calculated mass is used in Equation 8.3 to calculate the centrifugal force on each individual element. A safety factor of 1.5 and a load factor of 3 is used in all calculations. The safety factor of 1.5 is standard in aerospace industry. The load factor of 3 is a result of the analysis of Section 7.4. Now all moments and forces are known, the normal stress and shear stress are calculated. The centrifugal force is translated to a stress by dividing it by the element frontal area, which is calculated using Equation 8.4.

$$A_{\text{element}} = c_{\text{box}} \cdot t_{\text{skin}} \cdot 2 + h_{\text{box}} \cdot t_{\text{skin}} \cdot 2 - 4 \cdot {t_{\text{skin}}}^2 \tag{8.4}$$

The bending moment is transferred to a bending stress with Equation 8.5.

$$\sigma_{\text{z,box}} = -\frac{M_{\text{bending}} \cdot y}{I_{\text{xx}}} \tag{8.5}$$

In Equation 8.5 $\sigma_{\text{z,box}}$ is the normal stress, M_{bending} is the bending moment, y is the distance from the centroid to the boom and I_{xx} is the moment of inertia in [m^4]. The moment of inertia around the x-axis is calculated with Equation 8.6.

$$I_{\text{xx}} = 2 \cdot \left[\left(\frac{1}{12} \cdot c \cdot {t_{\text{skin}}}^3 \right) + \cdot t_{\text{skin}} \cdot \left(\frac{h}{2} \right)^2 \right] + \frac{1}{6} \cdot t_{\text{skin}} \cdot h^3 \tag{8.6}$$

At last the torsion is transferred to a shear stress τ with Equation 8.7 and 8.8.

$$q_{\text{shear}} = \frac{T_{\text{q}}}{2 \cdot A_{\text{enclosed}}} \tag{8.7}$$

In Equation 8.7 q_{shear} is the shear flow, T_{q} is the torque, which is calculated by multiplying the load with the torsion arm and A_{enclosed} is the enclosed area, calculated by $c_{\text{box}} \cdot h_{\text{box}}$.

$$\tau = \frac{q_{\text{shear}}}{t_{\text{skin}}} \tag{8.8}$$

These calculations are done for each element. It is taken into account that the moment arm of the loads of each element changes when the MATLAB program moves on to the next element in the beam. In the end the normal stresses and shear stresses are known in every boom of each element of the beam. These are then transferred into a total stress Y_{Mises} per location on the beam using the Von Mises method in Equation 8.9.

$$Y_{\text{Mises}} = \sqrt{\left(\sigma_{\text{z,box}} + \frac{F_{\text{centrifugal}}}{A_{\text{element}}}\right)^2 + 3 \cdot \tau^2} \tag{8.9}$$

The weight of the rotor is a summation of the weight of each element. In Figure 8.5 the first beam analysis is shown. c_{box} is equal to 0.110 [m] and h_{box} is equal to 0.026 [m], with a rotor radius of 4.105 [m]. These values come up when the ideal box is fitted in the selected airfoil of the rotor blade. The total radius of the rotor disk is 4.24 [m], but a length of 0.135 [m] is subtracted due to the fact that the hub is located at the center of the rotor disk. The hub design will be elaborated on in Section 8.3. Figure 8.4 shows how the box fits in the airfoil.

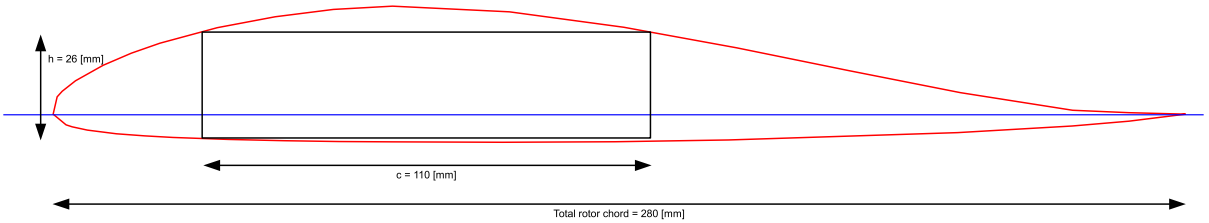

Figure 8.4: The rotor box fits exactly in the airfoil when it has a width of 110 [mm] and a height of 26 [mm]

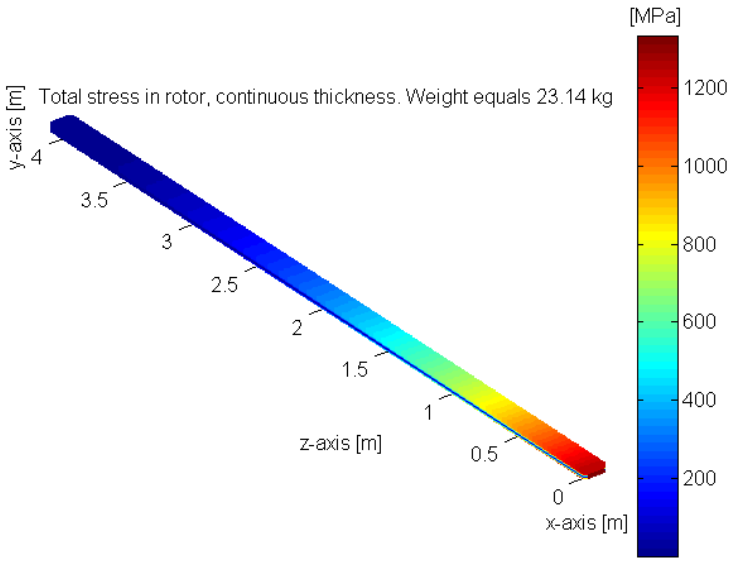

Figure 8.5: Initial rotor beam analysis

The skin thickness is selected to be 10 [mm], to make sure that the maximum stress in the beam is lower than the yield stress of T700S. The maximum tensile stress occurring is 1333 [MPa], while the maximum compressive stress is 1289 [MPa]. The weight of a single beam is 17.14 [kg], but 35 % is added for the leading edge and trailing edge material, resulting in a total blade weight of 23.14 [kg]. The 35 % is based on the cross sectional area of the airfoil when it has a thickness of 1 [mm], compared to the cross sectional area of the rotor box. A blue line can be seen along the length of each side of the box. As one can see, a blue color means that the stress is relatively low. This is due to the fact that along that neutral line, the stress switches from tension to compression, as the upper skin panel is in compression and the lower panel is in tension. It can also be seen that the stresses are not very well distributed along the blade. Therefore a second calculation is done where the thickness is varied along the length of the beam: from 1 [mm] at the tip up to 10 [mm] at the root. This results in Figure 8.6.

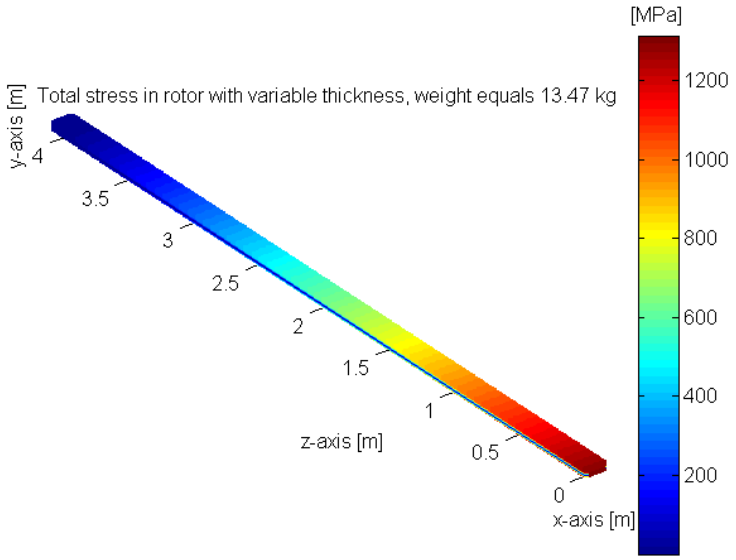

Figure 8.6: Second rotor beam analysis

The second iteration shows a significant reduction in blade weight from 23.14 to 13.47 [kg]. The maximum tensile stress equals 1314 [MPa] and the maximum compressive stress equals 1295 [MPa]. Both occur at the root of the blade. Still, more than half of the rotor is too strong for the stresses that are applied. Therefore a third calculation is made, where the thickness is kept constant at 1 [mm] from the tip to 25 % of the beam length, and from that point on the thickness increases linearly per element to 10 [mm] at the root. In Figure 8.7 the final rotor beam analysis is shown. Figure 8.8 shows the thickness variation along the beam length.

As can be seen, the red area with high stresses has expanded further towards the tip, which means that the highest stresses are occurring less locally. At the tip the beam still shows low values of stress. However, it is not possible to lower the skin thickness to less than 1 [mm], since this can not be produced. The maximum tensile stress is 1309 [MPa] and the maximum compressive stress is 1296 [MPa]. Another important aspect to notice in Figure 8.7 is the stress concentration at 25 % of the tip. This is due to the fact that from the tip the stress starts increasing towards the root, up until 25 % of the length, where the thickness starts increasing per element, reducing the stress slightly at that location. The weight of each blade is 10.77 [kg], a significant reduction compared to the initial weight of 23.14 [kg].

8.1.2 Rotor Blade Material Selection

The rotor analysis is, like many other design processes, an iterative process. To be able to do the calculations, one needs a material density, but since the stresses on the box are of course not known in advance, one can not pick a material and thus a density yet. This problem is overcome by starting with an estimated density of 1750 $\left[\frac{\text{kg}}{\text{m}^3}\right]$. With this value the calculations provide an indication of the stresses

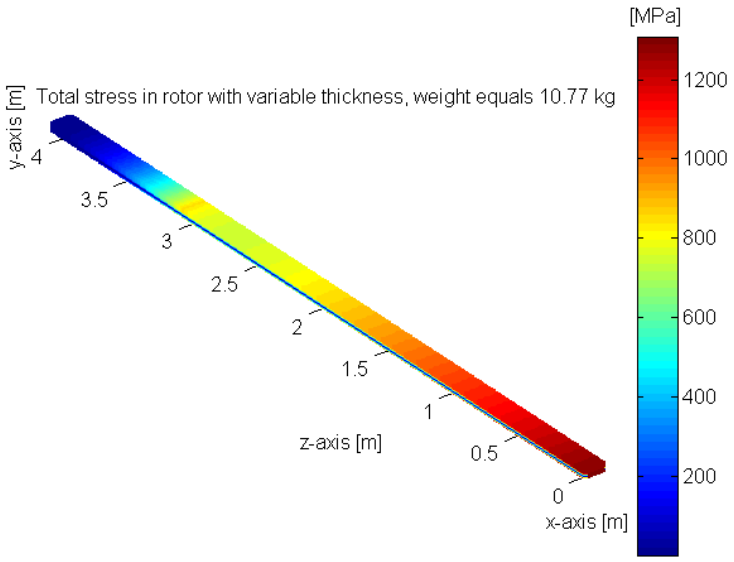

Figure 8.7: Final rotor beam analysis

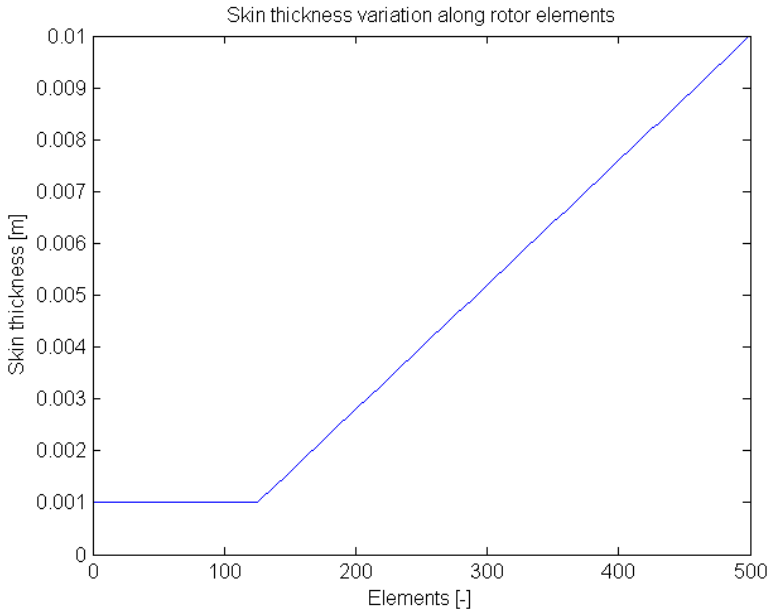

Figure 8.8: Thickness variation along beam length

with which the material should be able to operate. Now the preliminary stresses are known, it becomes clear that conventional materials like aluminum are not applicable at all. It would result in too high weights, as the density is around 2600 $[\frac{\text{kg}}{\text{m}^3}]$, and the maximum tensile stress of aluminum is around 600 [MPa], depending on the alloy [48]. Composites prove to be the better choice, as the density is lower and the tensile and compressive strength is higher, depending on the type of composite [49]. To assure that the cost will not grow to undesired heights, strong but expensive materials like Boron Fiber are excluded [50]. Eventually the selected material is carbon fiber T700S [47]. This is a high strength carbon fiber, which has the best suitable tensile and compressive strength, as well as a relatively low density of 1800 $\left[\frac{\text{kg}}{\text{m}^3}\right]$.

8.2 Rotor Mount Structural Analysis

In this section it is explained how the mount that connects the fuselage to the rotor hub is designed. To design the rotor mount a model is built that analyzes the mount in detail. This is done by first determining the forces that act on the mount. Next the same structural idealization method as for the rotor blade design that uses booms and skins is used, to determine the stresses in the mount. Then an optimization is done to reduce the weight, using optimal dimensions and a light material.

8.2.1 Rotor Mount Analysis

The dimensions of the rotor mount are based on the clearance of the rotors and the optimization for the weight of the mount. The necessary clearance height of the rotor influences the length of the rotor mount. The main influence is the angle at which the rotor blades are tilted to make sure that the blades do not collide with anything. It is found that the clearance height is 0.55 [m]. To have space for mounting the rotor mount to the airframe and the hub on the the rotor mount, this length is increased with 0.2 [m]. The optimization for the weight influences the width, height and the thickness. The minimum values for the height and the width are determined to be 0.1 [m]. This is to make sure that there is enough space for the attachments. This is due to the dimensions of the hub and the mounting of the rotor and hub on the mount. The final mount dimensions are shown in Table 8.1. These values resulted from the weight optimization discussed later in this section.

Table 8.1: Rotor Mount Dimensions

Parameter	**Value [m]**
Length	0.75
Width	0.1
Height	0.18
Thickness	0.001

Three different forces are identified that act on the rotor mount: the drag of the rotor system, the lift of the rotor system and the torque that is necessary to pre-rotate the rotor blades. The drag and the lift forces are point forces as can be seen in Figure 8.9. In these forces the assumption is made that the weight of the rotor system is negligible compared to the weight of the rest of the vehicle. Because of this, the tensile force in the mount is constant throughout the beam. In reality the tensile force throughout the mount is increasing from bottom to top, due to the fact that the weight of the mount has to be carried as well. However, this error is small and will therefore be neglected. The drag force on the rotor mount is mainly caused by tilting the rotor, which causes a backwards pointing drag force. This drag force is the highest when the tilting angle is 13.66 [deg] at maximum airspeed. This situation is used to determine the drag component of the rotor system. Next the drag component can be determined using Equations (8.10) and (8.11).

$$L = \text{MTOW} \cdot g_0 \tag{8.10}$$

$$D_{\text{rotor}} = L \cdot \tan(\alpha_{\text{rotor}}) \tag{8.11}$$

The torque on the mount is caused by the pre-rotation of the rotor in the transition phase. This pre-rotation torque is calculated in Section 7.1.3. The resulting forces can be seen in Table 8.2.

The rotor mount is designed for the critical case, which means that all three forces are applied at the same time, as can be seen in Figure 8.9. This will occur during the end of the transition phase and just before the start of the cruise phase. Here it is assumed that it is possible that the speed at the end of the transition phase is the maximum speed of the eGyro. However, in reality this will only occur when a failure of the control system occurs, which forces the nose of the eGyro down into a dive.

When designing the rotor mount for these forces, a load factor of 3 and a safety factor of 1.5 are used. The reason for these values is already mentioned before. This is done to design the mount in such a way that it can carry all the loads during the mission.

The method that is used to determine the stresses in the rotor mount is the same as for the rotor. However, since the forces are of a different kind point forces are used instead of distributed loads. Also

Table 8.2: Forces on the Rotor Mount

Parameter	**Value**	**Unit**
Vmax	226.8	$[\frac{\text{km}}{\text{h}}]$
Lift	$1.815 \cdot 10^5$	[N]
Rotor Drag Component	$5.06 \cdot 10^3$	[N]
Rotor mount Torque	$5.6 \cdot 10^3$	[N]
Critical Tilting angle	13.66	[deg]

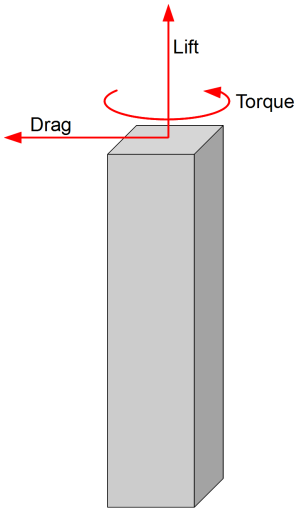

Figure 8.9: Forces acting on the rotor mount

no loads are applied that cause a moment, only a torque is applied. Therefore an adaptation is made to the MATLAB [13] script to account for these changes.

The drag component causes a bending moment throughout the mount, this bending moment can be calculated using Equation 8.14. To be able to use this equation, first the arm and load on each individual element needs to be known.

$$d_{\text{element}} = L_{\text{element}} \cdot n_{\text{element}} \tag{8.12}$$

In this equation d_{element} is the arm of each element, this is calculated by multiplying the length L_{element} of each element by the element number n_{element}.

$$F_{\text{element}} = D_{\text{rotor}} \cdot factor_{\text{safety}} \cdot factor_{\text{load}} \tag{8.13}$$

The load F_{element} on each individual element is determined by multiplying the drag component D_{rotor} of the rotor by the safety factor and the load factor.

$$M_{\text{element}} = F_{\text{element}} \cdot d_{\text{element}} \tag{8.14}$$

Equations 8.12 until 8.14 are then used for each individual element along the length of the mount, which is done using 250 elements. The amount of elements is selected to accurately determine the stresses in the mount. From the bending moment in each element the stress in each boom can then be determined.

First, each stress is determined that is caused by each individual load, next they are combined using the Von Mises stress method, as explained during the rotor design in Section 8.1.1. The bending stress that occurs in the mount can be determined using the same equation as for the rotor design, even though the bending moment is determined in a different way, as explained above. The equation for the bending stress can be seen in Equation 8.5. The tension stresses in the mount can be calculated using Equation8.15.

$$\sigma_z = \frac{F_{\text{element}}}{A_{\text{element}}} \tag{8.15}$$

In this equation the stress σ_z is calculated by dividing the tension F_{element} in each element by the surface area A_{element} in each element. The torsion stress in the mount can be found using Equation 8.7 and 8.8 as explained in Section 8.1.

Now that all the stresses are determined they can be combined using the Von Mises method using Equation 8.9 as explained in Section 8.1.1. The resulting stresses in the rotor mount can be seen in Figure 8.10.

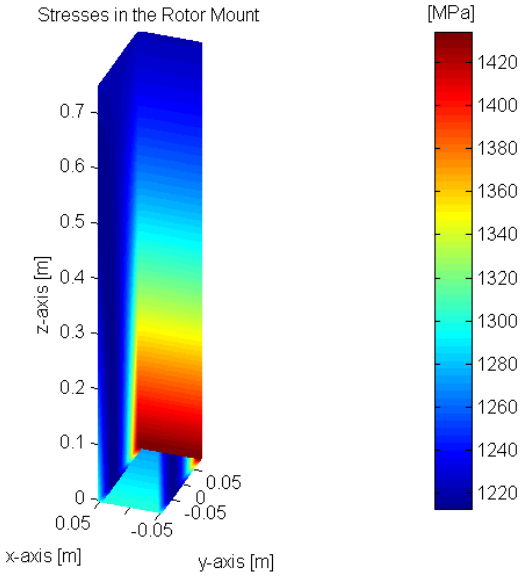

Figure 8.10: Stresses in the Rotor Mount

The design is optimized to decrease the weight. There are several ways to decrease the weight, by optimizing material choice and choose the best width, height and thickness. The choice of material is further elaborated on in Section 8.2.2.

It is investigated which dimension parameter could best be optimized to get the lowest possible weight. This is done by optimizing for each different parameter and combinations of parameters and finally compare the resulting weights. It is found that the width (x-axis) should be as small as possible, this is due to the fact that the stress is maximum in the wall (y-axis) of the beam, as can be seen in Figure 8.10. The final result is that optimizing the height (y-axis) was the best optimization strategy. When optimizing for the thickness, the weight is found to be about double the value as for the height. When an optimization is done for a combination of thickness and height, the weight is slightly higher than the weight for the height-only optimization method. The final rotor mount weight is 0.75 [kg]. The maximum stress in the rotor mount is 1434 [MPa].

8.2.2 Material Selection

The method for selecting the material that is used for the rotor mount is again the same method as for the material selection for the rotor. Since the main design criteria is the weight of the rotor mount, the strength of the material needs to be high with a low density. It is found that carbon fiber is the best material that can be used in this case, as explained in Section 8.1.2. Again carbon fiber T700S is found to be the best option as the material for the rotor mount. It is a high strength carbon fiber, which has the best suitable tensile and compressive strength, as well as a relatively low density of 1800 $\left[\frac{\text{kg}}{\text{m}^3}\right]$.

8.3 Rotor Hub Design

The rotor hub consists of the mechanical connection of the rotor blades to the vehicle and the rotor disk pitch mechanics. In helicopters it is a highly complex system that is capable of increasing and decreasing the pitch of each separate blade of the rotor. It also allows the blades for flapping movements and lead-lag movements. The auto-gyro hub is comparable to the helicopter hubs, but has one important

difference: the blade pitch is not adjustable, making the hub mechanically much less complex. Also lead-lag movements are less critical. However, designing the rotor hub from scratch is too hard to do within the time span of the project and with the knowledge available. A structural analysis of such complex objects would mean that CFD and finite element analyses are necessary. Calculations by hand on the subparts of the hub are not possible. Therefore it is chosen to investigate existing hub designs and scale them to fit on the eGyro.

8.3.1 Existing Hub Designs

Most auto-gyro designs operated today make use of two rotor blades. The hub is capable of performing teetering movements around a centrally located hinge, like a seesaw. As an example the PAL-V hub is shown in Figure 8.11 [9].

Figure 8.11: A close-up view of the PAL-V hub [51]

From the aerodynamic analysis it has become clear that not two but four rotor blades are necessary. Therefore the conventional auto-gyro hub design like the PAL-V's is not directly applicable to the eGyro. A study into four-bladed autogyros led to the hub of the Cloud Dancer II [52]. It uses exactly the same principle as the hub of the PAL-V, but since the vehicle has four blades, the second set of blades is placed perpendicularly on top of the first set. Both sets of blades have a teetering hinge. Figure 8.12 shows the hub of the Cloud Dancer II.

8.3.2 eGyro Hub Design

The PAL-V has an MTOW of 910 [kg], roughly half of the eGyro MTOW. It is assumed that the teetering part of the hub can therefore be almost exactly copied and placed perpendicularly on top of each other. The rotor shaft can of course not be copied in that way, as the forces on that are at least twice as high as on the PAL-V. The shaft is therefore designed as a square beam with a width of 100 [mm] and a thickness of 5 [mm]. The total length of the shaft is 505 [mm]. The shaft deforms from square at the top to round at the lower end. It is connected to the rotor mount with a ball and socket joint. Calculations on the shaft are performed in the same way as on the rotor mount. It is assumed that the forces are also applied in exactly the same way. This is in reality not the case. The bending moment due to the drag of the rotor blades is in reality distributed along the shaft, while it is calculated as a point load at the upper side of the shaft. The same holds for the torque in the shaft. Calculations are performed in the same way as for the rotor mount, showing that the shaft is able to withstand the applied forces when the shaft is made of steel. The maximum occurring stress is 490 [MPa], while the maximum stress for steel varies from 240 [MPa] to 1500 [MPa] [54]. Steel is chosen because of the complex shape of the shaft, which is easier to make using steel compared to for instance carbon fiber. Figure 8.13 shows the designed shaft.

The other parts of the hub are based on the PAL-V hub in Figure 8.11. The pre-rotation motor consists of two BLDC motors stacked, equal to the motors in the ducted fans that are discussed in Section 4.2.4.

Figure 8.12: A close-up view of the Cloud Dancer II hub [53]

Figure 8.13: Rotor shaft

In total they provide 10.4 [kW] power. The gears that transfer the motor rotations to the rotor have a ratio of 4 to 1. Since the pre-rotation speed is 200 [rpm], the motor has to provide 800 [rpm]. The design of the eGyro hub can be seen in Figure 8.14.

8.4 Tail Beam Design

As the tail produces lift in almost all phases of flight, a tail beam is designed to transfer the lift force to the fuselage. The tail is located 1.5 [m] behind the fuselage, requiring the tail beam to be the same length. For the analysis of the beam, the same method is used as for the rotor mount.

8.4.1 Tail Beam Analysis

The analysis is conducted in exactly the same way as the rotor mount, with exactly the same MATLAB [13] script. The only force applied is a point load at the end of the beam. It is assumed that the beam is clamped at the front. The maximum force applied is 3000 [N]. This force is induced when the vehicle is making sharp turns while a disturbance occurs. The load is again multiplied with the safety factor of 1.5 and a load factor of 3. The analysis is shown in Figure 8.15.

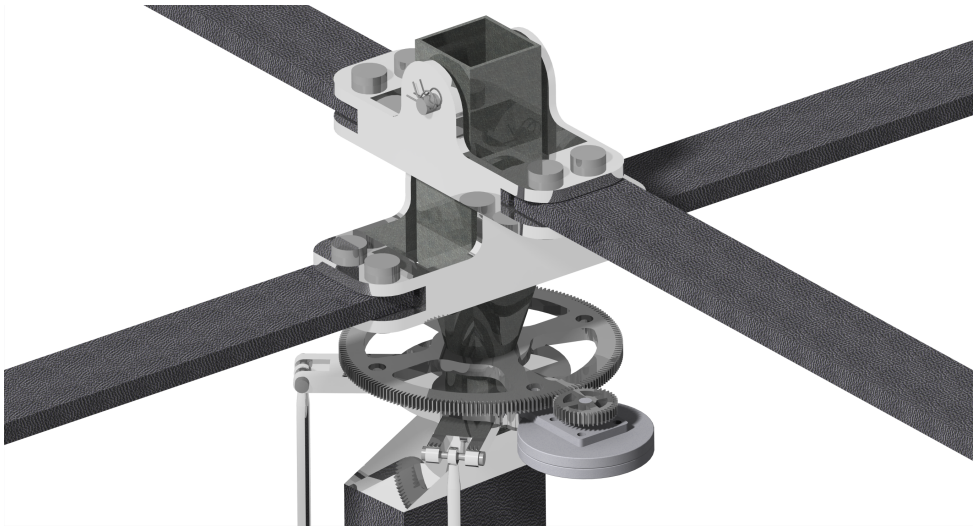

Figure 8.14: The eGyro hub

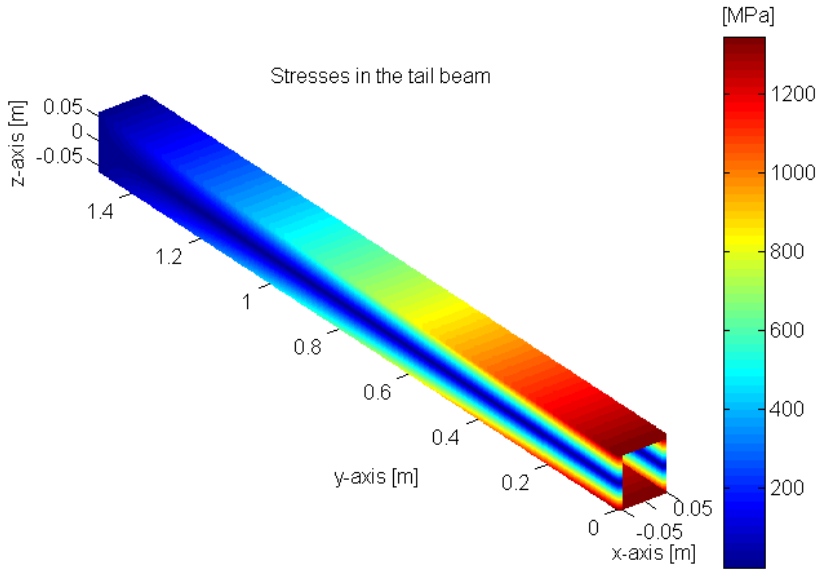

Figure 8.15: The tail beam analysis

8.4.2 Material Selection and Results

The analysis shows that the thickness can be 1 [mm] along the whole beam length. The width and height of the beam are 0.10 [m] and 0.11 [m] respectively. The length is set at 1.5 [m]. The maximum tensile and compressive stress occurring is 1347 [MPa]. The weight of the beam with these dimensions is 1.13 [kg] when using the same carbon fiber as for the rotor blades and rotor mount. Using other materials is possible, but the weight increase when using for instance aluminum is large, as the thickness of the beam should increase to lower the maximum stresses and the density of aluminum is already higher than for the T700S carbon fiber.

8.5 Fuselage Analysis

In this section the analysis of the fuselage is discussed. This is done by first explaining the method that is used to analyze the fuselage. Next, the different load cases are explained and analyzed. From this analysis the critical location for the fuselage is determined. Finally the critical load case is determined,

using the data that is obtained from the analysis of each load case.

8.5.1 Fuselage Design Method

The method that is used for the fuselage analysis consists of determining the critical load case and determining the locations in the fuselage were the highest stresses can be found. These stresses are then plotted where the tension and compression locations are shown. Here colors are used to show the stresses at each location in the fuselage. These colors represent a quantitative comparison between the location of the fuselage. The actual value of the stress of each point on the fuselage needs to be determined for a later stage of the design process, using software built for that purpose. However, to be able to analyze the fuselage the critical location need to be considered when starting the detailed design of the fuselage. This stress location can be used to give recommendations for the next step of the design iteration.

To determine the loads and the stresses on the fuselage, a simplified model of the fuselage is created. The simplified version of the fuselage can be seen as a simple beam with the general dimensions of the fuselage. These dimensions are determined from the requirement analysis and can be found in Table 8.7. Furthermore, since the tail beam is also designed in detail, this is not considered a part of the fuselage. This causes the analyzed fuselage to be 4.5 [m] long from the nose to the start of the tail beam. Next, to be able to calculate with the beam, it is assumed that the fuselage is in equilibrium during all the different load cases. The forces on the tail that are carried by the fuselage are represented with a moment at the fuselage, at the point where the tail beam is connected to the fuselage. An example of this can be seen in Figure 8.16. It has to be mentioned that this is only the case for the load cases where there is a vertical tail force. For example, there is no vertical tail force during the VTOL phase of the mission (Load Case 3) and for the landing phase (Load Case 4).

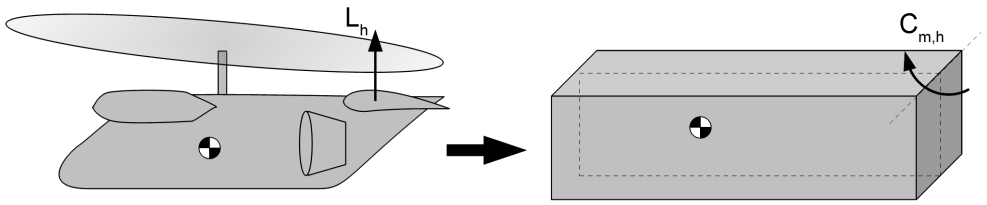

Figure 8.16: Tail Moment Representation

This is done to be able to determine the locations where the stress in the fuselage is critical. This can then be used to determine a detailed fuselage in later phases of the design. To be able to determine these stress locations a thickness is assumed. This thickness equals 0.001 [m], which is chosen because it is the engineering limit for most materials. This is the most critical case for the fuselage as the fuselage can be thicker when needed. However, this needs to be determined in later stages of the detailed fuselage design.

Table 8.3: Fuselage Representation Dimensions

Parameter	**Value [m]**
Length	4.5
Width	1.5
Height	1.7

To determine the stresses in the fuselage, a detailed analysis of all the forces throughout the fuselage needs to be performed. This is done through the loads that are placed on the fuselage for the different load cases. To make sure that the fuselage does not fail during its life-time, a safety factor of 1.5 and a load factor of 3 are used to account for all the possible forces that can occur during the mission. However, the load factor for the landing load case is higher and equals 4, as explained in Section 8.6, where the landing gear is designed in more detail. These loads throughout the fuselage can then be used to determine the representation of the stresses in the fuselage. However, the stresses that finally result from this method are not the final values that will occur in the fuselage of the final vehicle. The location of these stresses will be similar to the critical locations in the detailed design of the fuselage and can thus be used to further design the final fuselage with specialized computer software.

8.5.2 Load Cases

For the fuselage analysis, four different load cases are found. These four different load cases are used to determine the loads and the stress locations in the fuselage and can be found in Table 8.4. The loads that are applied during each of these load cases is different due to the change in orientation of the eGyro throughout its mission.

Table 8.4: Fuselage Load Cases

Parameter	Mission phase
Load Case 1	Cruise phase
Load Case 2	Transition phase
Load Case 3	VTOL phase
Load Case 4	Landing

Weight

The weight causes loads to be present throughout the fuselage. During this method it is assumed that the weight does not change for each load case. This means that the amount of fuel is constant for each load case. This is done because the weight during a VTOL operation is assumed constant for the VTOL load case. Since the transition phase is part of the VTOL phase, the weight during this phase is constant as well. This causes the weight during the beginning of the cruise phase to still be equal to the MTOW. Finally it might be necessary, due to emergencies or other special circumstances, that an emergency landing needs to be made when the cruise altitude still is not reached. This causes the critical weight to be equal to the MTOW for landing.

The weight of the vehicle for these load cases is distributed using point loads for the main components of the vehicle. These point loads are then placed at the center of gravity of each individual component. These point loads are further explained in Section 6. A representation of these weight can be seen in Figure 6.3 and in Table 6.1 and Table 6.2. The weights cause a moment in in the fuselage, these moments can be seen in Figure 8.17.

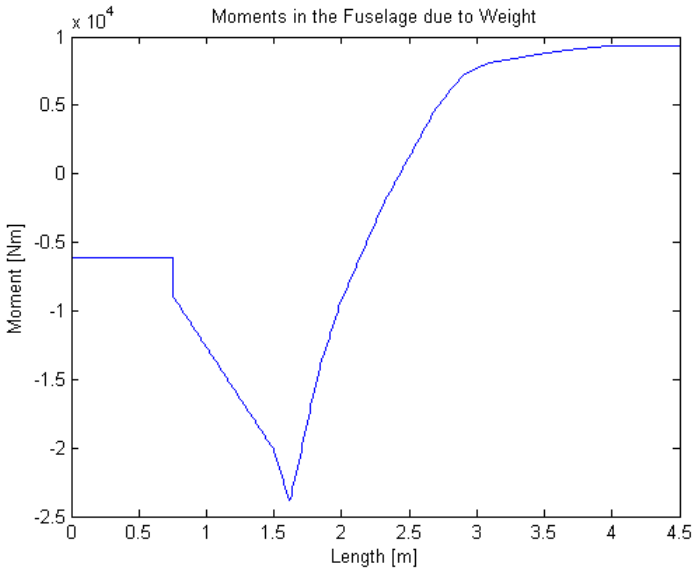

Figure 8.17: Moments in the fuselage due to weight

Load Case 1 - Cruise

The first load case that is found is during the cruise phase. This is the load case that will be the case during most of the mission. The main loads that act on the fuselage during this load case are the rotor lift, the thrust of the aft ducted fans, lift of the tail, the drag of the vehicle and the weight of the vehicle. A representation of these force can be seen in Figure 8.18.

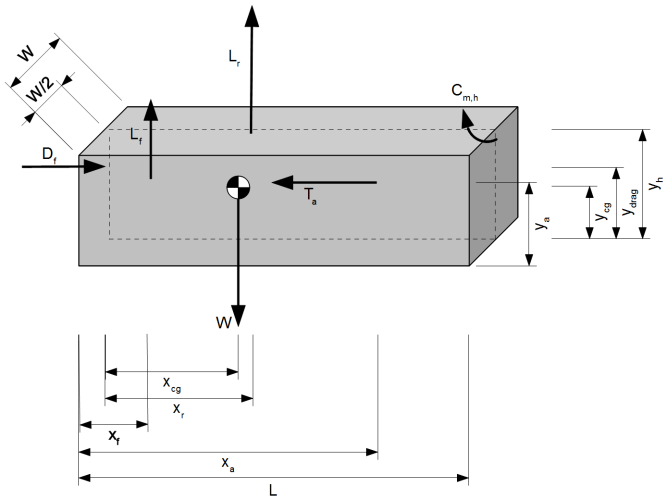

Figure 8.18: Forces for Load Case 1

The forces for load case 1 are determined using the orientation and speed during cruise. The weight is distributed as explained in Section 8.5.2. The rotor lift is estimated as the MTOW converted to force. The tail has a contribution during cruise and therefore the moment caused by the tail is present again at the clamping. The thrust of the ducted fans during cruise is as explained in Chapter 7. Finally, the drag during cruise is determined, which is done using the lift over drag ratio of 4.5. This drag is the total drag and the point where it acts is determined from the fact that the resultant moment at the clamp needs to become the tail moment in this case. The value for these forces can be found in Table 8.5.

Table 8.5: Load Case 1 Forces

Parameter	**Value**
Rotor lift	$1.915 \cdot 10^4$ [N]
Drag	$4 \cdot 10^4$ [N]
Thrust	$2 \cdot 10^3$ [N]
Tail lift	$1.000 \cdot 10^3$ [N]

Most of these forces act on the middle of the fuselage, but only the thrust acts on both sides of the fuselage. The critical forces for this load case are a combination of the bending and the compression forces due to the high moments in the fuselage and the drag of the vehicle. The moments can be seen in Figure 8.19. The tension is important in the cockpit part of the fuselage where the compression force is equal to the drag of the vehicle. The torsion forces in the fuselage for this load case are present, but are not critical.

Using all the loads on the fuselage as calculated using the same method as explained in earlier sections of this chapter, the stresses can be determined and can be seen in Figure 8.20.

The critical stress location for this load case is the bottom of the cockpit section of the fuselage, as can be seen in Figure 8.20. This is caused by the negative moment due to the weight of the crew and equipment in the cockpit.

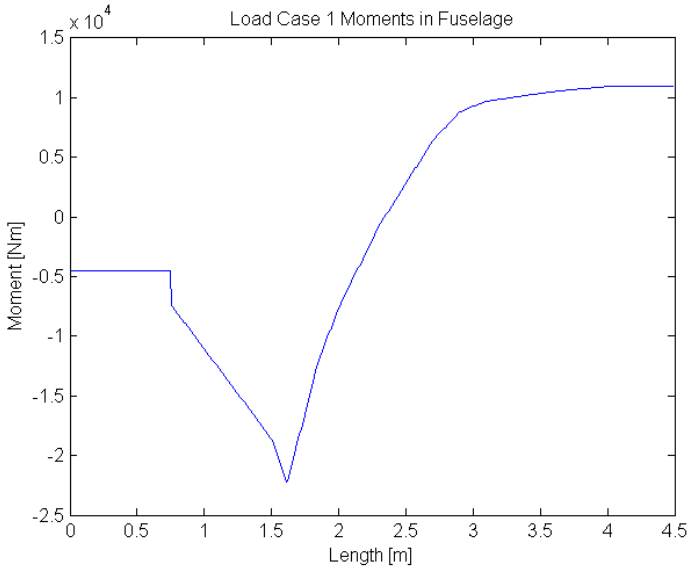

Figure 8.19: Moments Throughout the Fuselage for Load Case 1

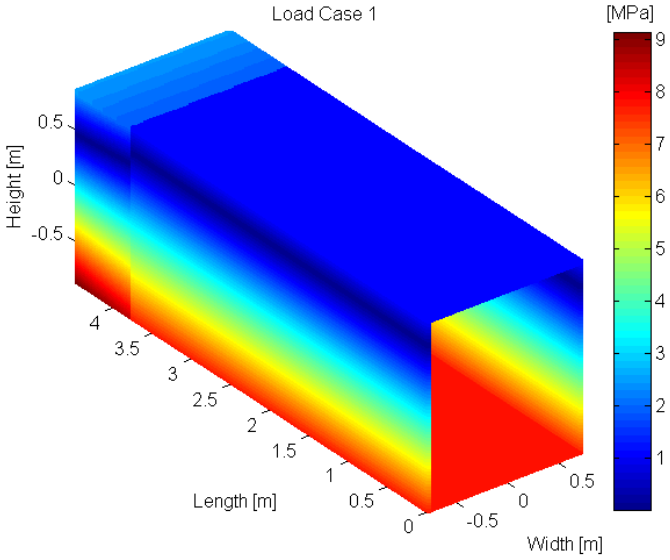

Figure 8.20: Load Case 1 Stresses

Load Case 2 - Transition

The second load case is transition, which happens every time the rotor is started or turned off. The transition phase of the mission consists again out of several phases, these phases are discussed in Section 7.1. These four different phases are converted to load cases. The first phase for the transition can be considered the same as for VTOL, which is load case 3 and is discussed later on. The other three phases have similar forces acting on the fuselage. The front ducted fan produces a constant vertical thrust during phase 2 and 3, however it is turned off during phase 4 and is therefore zero in the final phase of transition. The vertical thrust of the aft ducted fan is not constant. This is because the ducted fan is tilted throughout these phases, due to the transition to cruise. This is explained in Section 7.1, where the transition phase is explained in detail. The final angles of each phase are found to be critical and are therefore used to analyze the transition load case. These angles are 4.5 [deg], 26.5 [deg] and 68.5 [deg] for phase 2, 3 and 4 respectively. The rotor lift is also not constant during each phase, which is because the rotor is pre-rotated during the transition phases. How these lift forces are obtained can be seen in

Section 7.1. The values for the rotor lift and fan thrust can be found in Table 8.6. Finaly the drag is determined using the lift over drag ratio of 4.5 and the lift that is generated during each phase. The values for drag of each phase can also be seen in Table 8.6.

Table 8.6: Load Case 2 Forces

Parameter	**Value [N]**
Rotor lift phase 2	$2 \cdot 10^3$
Rotor lift phase 3	$6.5 \cdot 10^3$
Rotor lift phase 4	$1.915 \cdot 10^4$
Thrust Aft Ducted Fan	$5.597 \cdot 10^4$
Thrust Front Ducted Fan	$4.537 \cdot 10^4$
Drag phase 2	$2.123 \cdot 10^4$
Drag phase 3	$2.460 \cdot 10^4$
Drag phase 4	$2.148 \cdot 10^4$

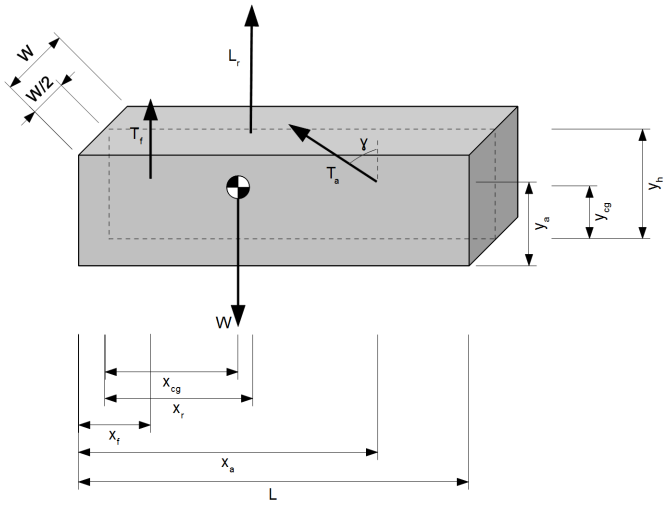

Figure 8.21: Forces for Load Case 2

The moments for each phase of the transition can be seen in Figure 8.22. For phase 2 and phase 3 the moments are the critical forces. However, for phase 4 the moments are not the only critical forces, since compression forces are also critical. The compression forces for this load case are critical in the cockpit part of the fuselage. The compression force in this part is equal to the drag force for phase 4.

The stresses that occur for this load case can be found in Figure 8.23. The critical locations of the stresses for phase 2 and 3 are similar, as can be seen in Figure 8.23. The critical location is at the bottom of the fuselage at the most aft part of the cabin. The critical location for phase 4 is different, this is due to the decrease in the moment due to the decrease of the lift of the front ducted fan. The critical location for phase 4 is the aft part of the cockpit section of the fuselage.

Load Case 3 - VTOL

During VTOL, three forces act on the fuselage: the vertical thrust of both the front and the aft ducted fans and the weight of the vehicle. A representation of these forces can be seen in Figure 8.24. The vertical drag is assumed to be zero during this load case and is therefore not taken into account. The vertical thrust of the front and the aft ducted fan are determined in Section 4.1. The weight during this load is as explained in 8.5.2.

The critical loads during this load case are the moments in the fuselage caused by the vertical forces placed on the fuselage. The moments in the fuselage can be seen in 8.25(a). Due to the symmetry of the

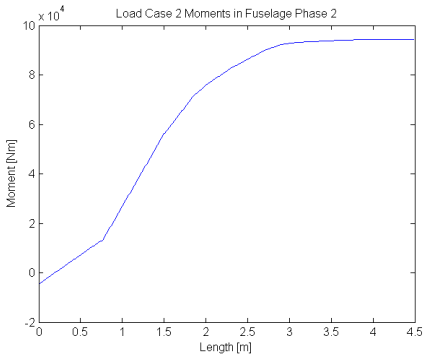

(a) Landing on Front Landing Gear

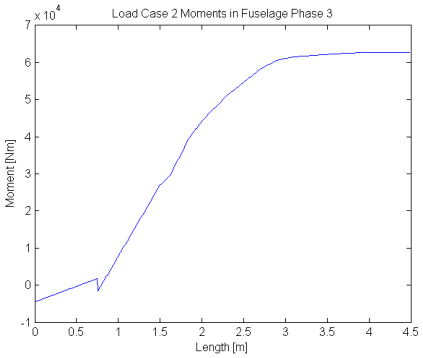

(b) Landing on Aft Landing Gear

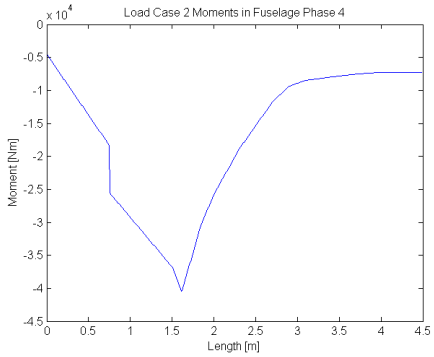

(c) Landing on All Landing Gear

Figure 8.22: Load Case 2 Moments Throughout the Fuselage for all phases

Table 8.7: Rotor Mount Dimensions

Parameter	**Value**
Aft Fan Vertical Thrust	$5.597 \cdot 10^4$ [N]
Front Fan Vertical Thrust	$4.538 \cdot 10^4$ [N]

forces in this load case, the torsion loads on the fuselage are low. The stresses caused by the torsion and bending loads on the fuselage for this load case can be found in Figure 8.25(b).

The critical stress location for this load case are at the most aft section of the fuselage. The top of the fuselage is in compression due to the sign of the moment and the bottom part is in tension. However, the stresses for this load case are not very high. This is because the forces are more distributed over the fuselage due to the four ducted fans. Therefore, this load case is not the critical load case for the eGyro.

Load Case 4 - Landing

The final load case is the landing load case. This is when the eGyro is just touching the ground. In this load case it is assumed that it is possible to land with one landing gear first, after which the others come into contact with the ground. Therefore the critical load case is when only one of the four landing gear wheels is on the ground. Because of this there are three different sub load cases within this load case, one for landing on front and aft landing gear each and one for landing on all wheels at the same time. In Figure 8.25 the forces for this load case are shown. As explained before the forces on the landing gear are not applied at the same time during each sub load case.

The load factor for this is different than for the other load cases, this due to the requirements that are necessary for emergency landing. The load factor that is used 4, as explained in Section 8.6. The safety factor that is used for structural designing is still equal to 1.5. The force on each landing gear is equal to the MTOW times the gravitational acceleration.

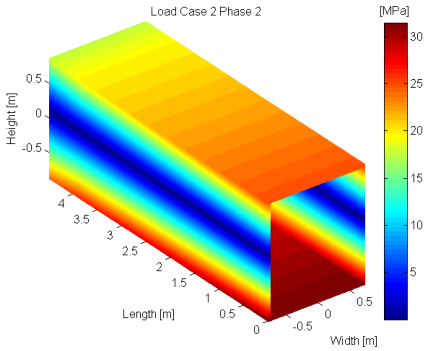

(a) Landing on Front Landing Gear

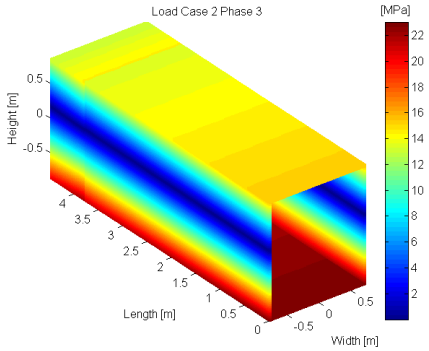

(b) Landing on Aft Landing Gear

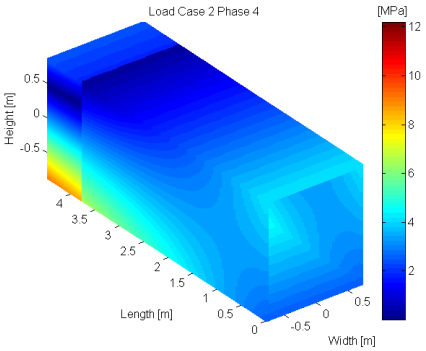

(c) Landing on All Landing Gear

Figure 8.23: Load Case 2 Stresses in the Fuselage for all phases

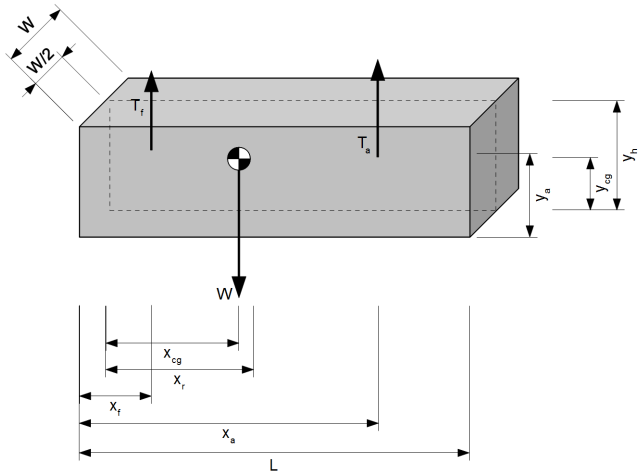

Figure 8.24: Forces for Load Case 3

The forces that are applied on the fuselage cause moments and torques on the fuselage. The critical loads are the moments in the fuselage. These moments are again calculated using the method explained in this chapter. The resulting moments in the fuselage for each sub load case can be found in Figure 8.26.

When all the loads on the fuselage are know the stresses can again be calculated, using the method explained before. These stresses can be seen in Figure 8.27. The stresses in Figure 8.27 are compression forces on the top of the fuselage and tension forces on the bottom of the fuselage. The critical location for all the different sub load cases is the same. The critical location for the tension case is the at the

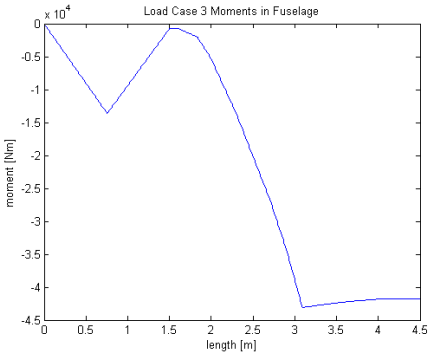

(a) Landing on Front Landing Gear

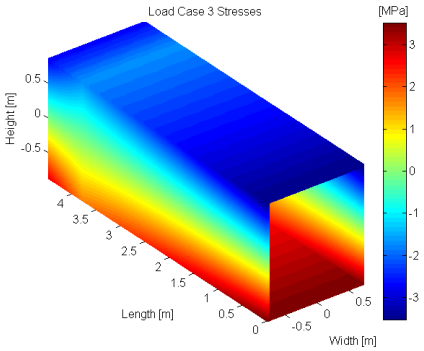

(b) Landing on Aft Landing Gear

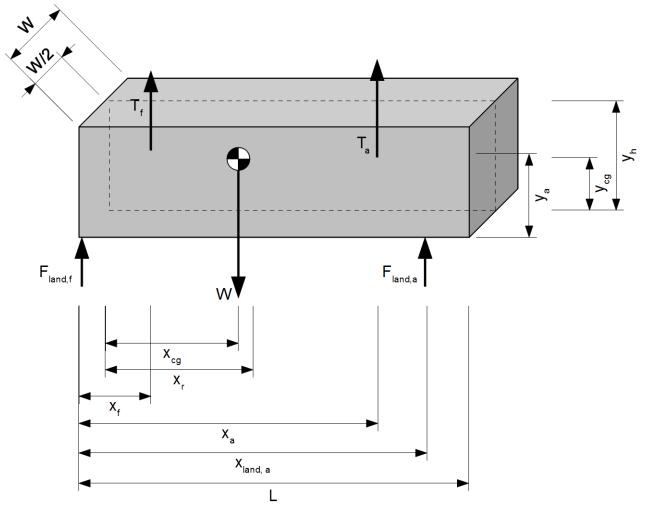

Figure 8.25: Forces for Load Case 4

bottom of the fuselage at the end of the fuselage. The critical location for the compression is also on the end of the fuselage, but then on the top of the fuselage.

Critical Load Case and Critical Stress Locations

From the analysis of all the different load cases a critical load case is determined. The critical load case is landing, because of the higher load factor and the high forces and moments that act on the fuselage. Therefore the critical stress point for landing needs to be well designed in the final fuselage design. The critical stress locations can be seen in Figure 8.27(a). The critical location for tension is the bottom of the fuselage where the cabin ends. For compression this is the top of the fuselage, were the tail beam is attached. These critical locations can then be used to design a detailed load carrying structure. A recommendation for an airframe is explained in the recommendations section.

8.6 Landing Gear

This section describes the design of the landing gear for the eGyro vehicle. The vehicle will use the landing gear both to land on the ground as well as driving on roads and other driveable surfaces.

8.6.1 Landing Gear Configuration

The vehicle has to be used for multiple purposes and it is established that a driving capability would greatly increase the operational capabilities of the vehicle and an increase in usability and ease of use

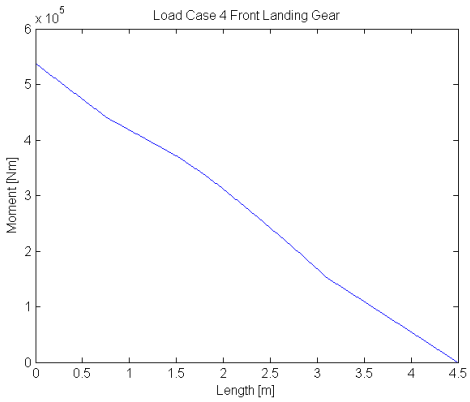

(a) Landing on Front Landing Gear

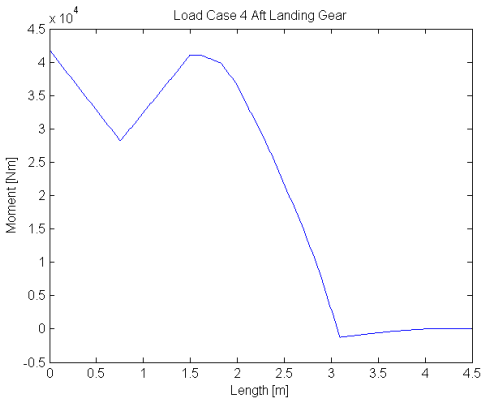

(b) Landing on Aft Landing Gear

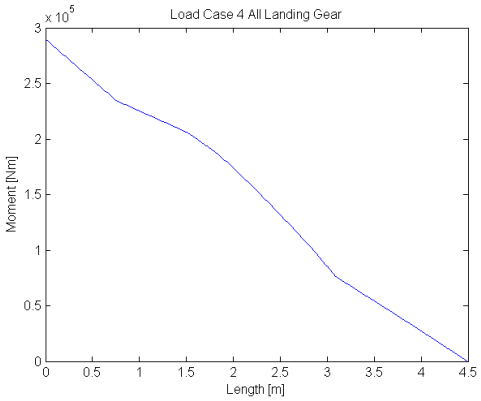

(c) Landing on All Landing Gear

Figure 8.26: Load Case 4 Moments Throughout the Fuselage

would be achieved. With this in mind, it could also be noted that different costumers and stakeholders require different landing gears. For example, for use in disaster stricken areas, such as depicted in the scenario sketched by the flying hospital group, a heavy duty landing gear with some degree of off-road or bad surface driving capability is required. To enable a versatile and an adaptable design, it is established that a modular system would be preferable, such that other landing gears could be applied to the vehicle with relative ease. For the preliminary configuration, a wheel configuration is chosen. Different landing gear configurations can also be attached to the eGyro. Four types of landing gears are identified.

Skids

Skids consist of a tube-like structure placed beneath the fuselage of a helicopter. Skids as landing gear are commonly applied for light to medium-sized helicopters. Advantages of skids are the light design and robust setup as well as relative low costs. The design incorporates no moving parts, which keeps maintenance at a minimum. Disadvantages of a skid configuration is the increased drag and reduced mobility. Skids cannot be retracted during cruise flight, such that extra drag is caused during cruise flight. The vehicle is not maneuverable on the ground, as skids are fixed and do not have a degree of freedom. Damping and absorption of a landing impact is achieved with the elasticity of the structure. In Figure 8.28 skids are displayed to give a general impression. The skids are an interesting option for costumers which do not require maneuverability on the ground. For design, current skids found on existing helicopters of the same weight class can be used.

Water Landing Configuration

The vehicle can also be equipped with floating type devices, to enable landing on water. To achieve this, a skid like construction can be implemented with floating devices attached. With the skid like

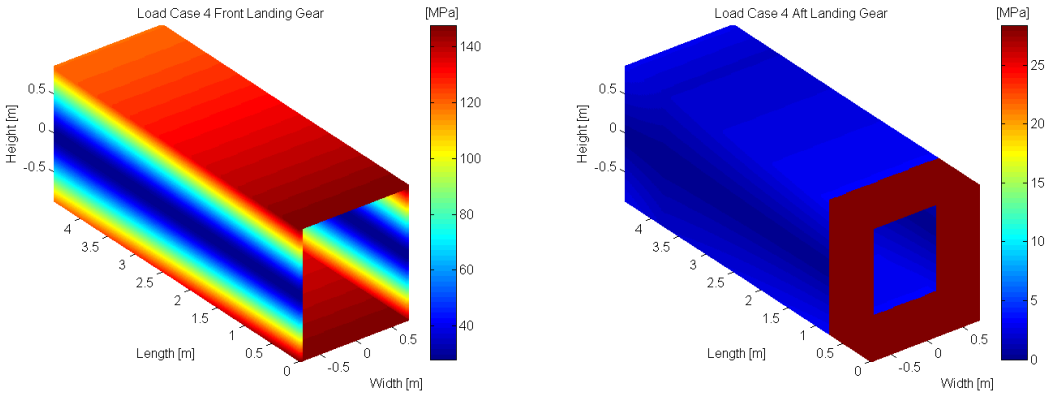

(a) Landing on Front Landing Gear

(b) Landing on Aft Landing Gear

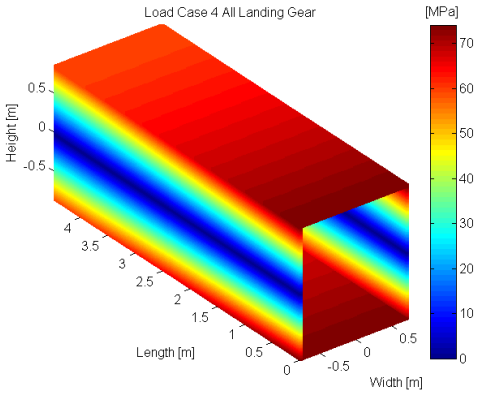

(c) Landing on All Landing Gear

Figure 8.27: Load Case 4 Stresses in the Fuselage

Figure 8.28: Example of helicopter skids [55]

construction, the vehicle will still be able to land on land surfaces. A sketch of this configuration can be found in Figure 8.29. Disadvantages of this design include more aerodynamic drag and a heavier landing gear.

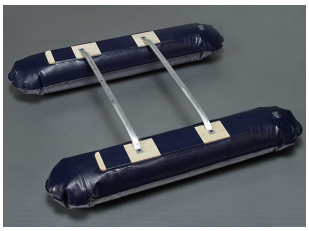

Figure 8.29: Example of helicopter float landing gear [56]

Standard Wheeled Configuration

The wheeled configuration consists of four wheels, of which two are located at the back of the fuselage. It is chosen that the wheels located at the back contain electric motors to enable the vehicle to drive. The front set of wheels are able to turn. Optionally, all four wheels can be able to turn for increased maneuverability in urban areas. However, this is not elaborated in this design stage. Since the vehicle needs to maneuver in urban areas, small obstacles (such as sidewalks/pavements) have to be overcome. This renders conventional wheel sizes for wheeled helicopters with comparable MTOW too small. For the wheel size a diameter of 12 inch is chosen, comparable to smaller city cars. The tires are sized according to helicopter standards. A sketch of the general wheeled configuration can be found in figure 8.30. In general, the advantage of using a wheeled configuration is the maneuverability on the ground. Disadvantages are more complexity and maintenance sensitivity and possibly a heavier weight for the landing gear when compared to skids. A driving capability is deemed important, as it provides a large advantage over current EMS VTOL vehicles, in combination with the smaller size of the vehicle. For the design, the wheeled configuration is regarded as the default configuration and will be investigated further in the conceptual design. The other configurations should be looked into with more detail when further development is performed.

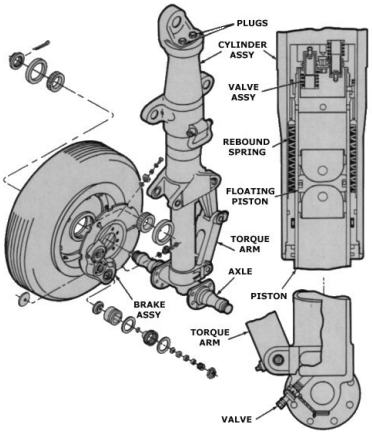

Figure 8.30: Example of a CH-47 Chinook helicopter wheeled landing gear [57]

Rugged Wheeled Configuration

The rugged wheeled configuration is based on the standard wheeled configuration. Adjustments are made to enable the vehicle to operate on rough and off-road ground conditions. Adjustments include four wheel drive, which is enabled by placing an electric motor inside each wheel. Also larger wheels and off-road tires are equipped. The main advantage, when compared to a standard wheeled configuration, is that the vehicle can operate in more off-road conditions. This in particular is a suitable landing gear for use in disaster stricken areas. Disadvantages are a heavier landing gear and more aerodynamic drag with respect to the standard wheeled configuration.

8.6.2 Required Power for Landing Gear

In order to find the driving capability of the eGyro is feasible, the required power should be calculated for driving. First of all, the rolling resistance of the vehicle needs to be determined. This rolling resistance depends on the friction coefficient and the weight of the vehicle as seen below in Equation (8.16).

$$F_{\text{roll}} = \mu \cdot m \cdot g_0 = 0.02 \cdot 1850 \cdot 9.81 = 362.97 \text{ [N]} \tag{8.16}$$

Note that the friction coefficient μ has been determined at 0.02. This value is an estimation, based on reference road vehicles [58]. Next, for the drag of the vehicle, Equation (8.17) is used:

$$F_{\text{air}} = 0.5 \cdot \rho \cdot A_{\text{frontal}} \cdot C_d \cdot V^2 = 0.5 \cdot 1.225 \cdot 6 \cdot 0.6 \cdot 69.4 = 153.125 \text{ [N]} \tag{8.17}$$

For above equation, the drag coefficient C_d is estimated at 0.6. This estimation is also based on reference automotive vehicles [59]. The frontal vehicle area A_{frontal} is determined to be equal to 6 [m^2] and the density equals the density at sea level. Also, the speed is obtained from the requirement that the vehicle should be able to drive with at least 30 $\left[\frac{\text{km}}{\text{h}}\right]$.

Continuous Driving, Acceleration and Hill Percentage

Now both the air and rolling resistance are determined, the required power for continuous driving can be calculated using Equation (8.18) as follows:

$$P_{\text{drive}} = (F_{\text{roll}} + F_{\text{air}}) \cdot V = (153.125 + 362.97) \cdot 8.33 = 4300.79 \text{ [W]} \tag{8.18}$$

Of course, the vehicle has to accelerate and climb certain hills in order to have a practical driving functionality. First of all, the required energy for the vehicle acceleration is calculated using the kinetic energy Equation (8.19).

$$\text{KE} = 0.5 \cdot m \cdot V^2 = 0.5 \cdot 1850 \cdot 69.44 = 64236.11 \text{ [J]} \tag{8.19}$$

In order to get the required power from this energy relation, an acceleration time for a velocity change from 0 to 30 $\left[\frac{\text{km}}{\text{h}}\right]$ has to be estimated. It is chosen that this acceleration time equals five seconds, which can be seen in Equation (8.20).

$$P_{\text{acceleration}} = \frac{64236.11}{5} = 12847.22\text{[W]} = 12.85 \text{ [kW]} \tag{8.20}$$

Next to acceleration, the vehicle has to be able to climb a hill. The hill percentage that needs to be encountered by the eGyro is taken to equal five percent, as seen in Equation (8.21). This hill percentage is just a requirement, which is set by the design team in advance.

$$V = 0.05 \cdot 8.33 = 0.42 \left[\frac{\text{m}}{\text{s}}\right] \tag{8.21}$$

The required power to overcome the hill equals, according to Equation (8.22):

$$P_{\text{hill}} = m \cdot g_0 \cdot V = 1850 \cdot 9.81 \cdot 0.42 = 7561.875 \left[\frac{\text{J}}{\text{s}}\right] = 7.56 \text{ [kW]} \tag{8.22}$$

However, the power mentioned above is just needed to overcome the hill percentage. Therefore, this P_{hill} needs to be added to the required power for continuous driving, see Equation (8.23):

$$P_{\text{totaldrive}} = 7.56 + 4.3 = 11.86 \text{ [kW]} \tag{8.23}$$

Power Optimization for Driving Capabilities

As can be seen from above equations, the maximal required power for the vehicle for the desired acceleration and hill percentage equals 12.85 [kW]. However, in order to optimize the vehicles' driving capabilities, the available power for the driving of the vehicle equals 20 [kW]. This available power is derived as the desired driving distance equals two kilometers. Hence, the required amount of [kWh] equals 1.33 [kWh]. This is actually a relatively low required amount of [kWh], since this can be charged by the generator in a relatively short period of time since the driving power is very low compared to the VTOL power. Now, rewriting the required power equations for 20 [kW] can be seen in Equations (8.24) and (8.25):

$$t_{\text{acc}} = \frac{64236.11}{20000} = 3.21 \text{ [s]} \tag{8.24}$$

$$\text{Hill Percentage} = \frac{(20 - 4.30079) \cdot 100)}{1850 \cdot 9.81 \cdot 8.33} = 10.38 \text{ \%} \tag{8.25}$$

This results in two motors in the rear landing gear, if the same motors are used as in the ducted fans. Since these are most feasible for this design and will result in 2 motors on each side, if the prototype is used for sizing and power/weight/cost-estimation.

8.6.3 Forces Acting on Landing Gear

In this section, the forces acting on the landing gear are discussed. The landing gear is sized according to the CS-27 regulations [6], which states that the vehicle needs to resist a fall from a height of 0.495 [m] and a design deceleration of 4g. Besides landing forces, driving forces should also be carried by the landing gear and the rest of the structure. For these loads the longitudinal forces will not be critical and assumed to be equal to the weight of the vehicle. An additional force will be applied for corners, where corners are assumed to be driven with a velocity of 15 $\left[\frac{\text{m}}{\text{s}}\right]$ at a radius of 3 [m]. Those values are estimated and based on a normal road, where the vehicle is assumed to be a point mass to come up with the forces acting on the total vehicle. These loads are multiplied with a safety factor of 1.5. The height of the landing gear depends on the configuration, regulations as stated before and ease of use of the vehicle. Trading off comfort, suspension height and usability the height of the landing gear will be designed to be 0.7 [m], which is based on component size and floor height of the vehicle. The assumption is made that the tires used are rigid and will not add any suspension on the front and aft landing gear.

Front Landing Gear

For the front landing gear, use has been made of a landing gear according to figure 8.31. Note that in this figure, the sizes are in [mm].

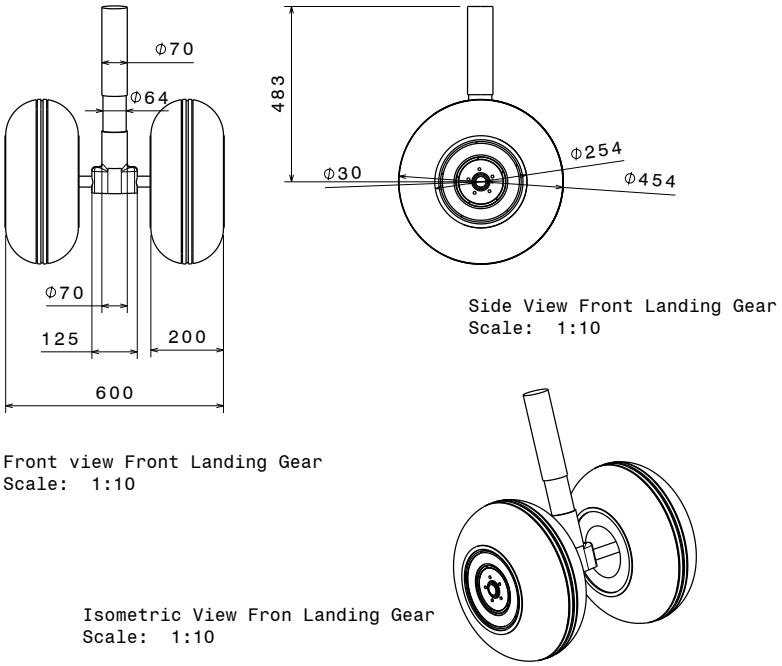

Figure 8.31: Front landing gear of the eGyro

Next, the vertical velocity is calculated using the energy relation in Equation (8.26).

$$m \cdot g_0 \cdot h = 0.5 \cdot m \cdot V^2 \tag{8.26}$$

When filling in the vehicle mass m, the gravitational acceleration g_0 and height h, the equation simplifies to Equation (8.27).

$$1850 \cdot 9.81 \cdot 0.495 = 0.5 \cdot 1850 \cdot V^2 \tag{8.27}$$

It turns out that above equation leads to a vertical velocity of 3.12 $\left[\frac{\text{m}}{\text{s}}\right]$, which is equal to approximately 11 $\left[\frac{\text{km}}{\text{h}}\right]$. Next, this velocity can be used to calculate the acceleration of the vehicle when the shock absorbers are used in the landing gear. It is assumed that the shock absorber has a length of 0.2 [m]. Hence, Equations (8.28) and (8.29) below can be used:

$$s_{\text{shock}} = 0.5 \cdot a_{\text{t}} \cdot t^2 \tag{8.28}$$

$$V = a_t \cdot t \tag{8.29}$$

When filling in these equations with the found velocity V and the estimated shock absorber length of 0.2 [m], the acceleration a_t equals -24.33 $\left[\frac{m}{s^2}\right]$. This required acceleration is actually a deceleration when the landing gear touches the ground and can be calculated to be 3.72g if a safety factor of 1.5 is applied. This value is near to the stated 4g from regulations, so the highest value (4g) will be used for the further design. Now the acceleration is known, use can be made of Newton's second law, as seen in Equation (8.30).

$$F = m \cdot a_t \tag{8.30}$$

Hence, when filling in the vehicle mass divided by four, since the landing gear consists of four wheels, and the found acceleration above, the vertical force acting on one landing gear segment equals 18148.5 [N]. However, for the calculations use is made of the total landing force on one strut: 72594 [N]. Using this value, the buckling formula for a simply supported beam (Equation 8.31) is used:

$$P_{crit} = \frac{n^2 \cdot \pi^2 \cdot E_{mod} \cdot I_{xx}}{{L_b}^2} \tag{8.31}$$

In Equation (8.31) n stands for the buckling mode, which is naturally 1. E_{mod} equals the Young's modulus, which equals 200 [GPa] for steel, L_b is the length of the beam, which equals 0.2 [m], as seen in Figure 8.31. Finally, I_{xx} equals the second moment of area, which needs to be calculated to determine the thickness of the landing gear tubes. By using 72594 [N] for P_{crit}, the second moment of area turns out to be $1.47 \cdot 10^{-9}[m^4]$. For a hollow cylinder, Equation (8.32) holds:

$$I_{\text{hollow cylinder}} = \frac{\pi \cdot (d_0^4 - d_i^4)}{64} \tag{8.32}$$

In Equation (8.32), d_0 and d_i stand for the outer diameter and the inner diameter of the hollow cylinder, respectively. Using a maximum compressive yield stress of steel of 350 [MPa], the area can be found according to Equation (8.34), which is derived from Equation (8.33)

$$\sigma_{yield} = \frac{P_{max}}{A} \tag{8.33}$$

$$350 \cdot 10^6 = \frac{72594}{A} \tag{8.34}$$

Hence, the area of the tube should equal $2.074 \cdot 10^{-4}$ [m^2]. Since it is known that this area equals the outer area minus the inner area and using an outer radius of 25 [mm], the inner radius turns out to be equal to $r = 0.02364$ [m]. Hence, the required thickness of the vertical tube equals $t = 1.357 \cdot 10^{-3}$ [m].

Now it has to be checked if the landing gear will not yield occur when driving. During designing, the landing gear should be able to carry two different loads which will be calculated below. First the weight should be carried, which will be calculated again using Equation (8.30), using 1g and the MTOW. Using these values and a safety factor of 1.5 a force of 6805.7 [N] per landing gear results from the calculations. Now the horizontal forces can be calculated during the earlier defined corners. In Equation (8.35) the radial acceleration will be calculated to be 5.79 $\left[\frac{m}{s^2}\right]$. Using this calculated acceleration in combination with the MTOW and again a safety factor of 1.5, Equation (8.30) results in a horizontal force of 4017 [N] per landing gear.

$$a_{radial} = \frac{V^2}{r} = \frac{4.17^2}{3} = 5.79 \left[\frac{m}{s^2}\right] \tag{8.35}$$

In the thick beam the normal stress can now be calculated. This consists of a normal stress, calculated using Equation (8.33) and an added normal stress from the horizontal force when taking a turn. This added normal stress will be calculated using Equation (8.5). Since the horizontal force is applied at the ground, the moment will be maximum at the highest point of the landing gear and will be 3213 [Nm] (4017 [N] $\cdot$ 0.8 [m]), assuming the lateral forces will be distributed evenly at all four wheels. The moment of inertia is calculated to be $4.6 \cdot 10^8$ [m^4] using Equation (8.32). Y is here the distance from the centroid, which will be maximum half the outer diameter in this case. This results in an stress higher than the yield stress of steel. Changing the outer diameter into 0.07 [m] with a thickness of 0.003 [m] was proven to be sufficient and will thus be the final dimensions, where the total height is now 0.71 [m]. This height should be similar to the landing gear height at the rear

Rear Landing Gear

The rear landing gear configuration can be seen in Figure 8.32. This landing gear configuration differs from the front configuration since it does not need a steering function. Hence, this landing gear configuration consists of one shock absorber and two struts to carry lateral loads better. It has to be noted that these wheels will be powered by an direct electric drive in the rim.

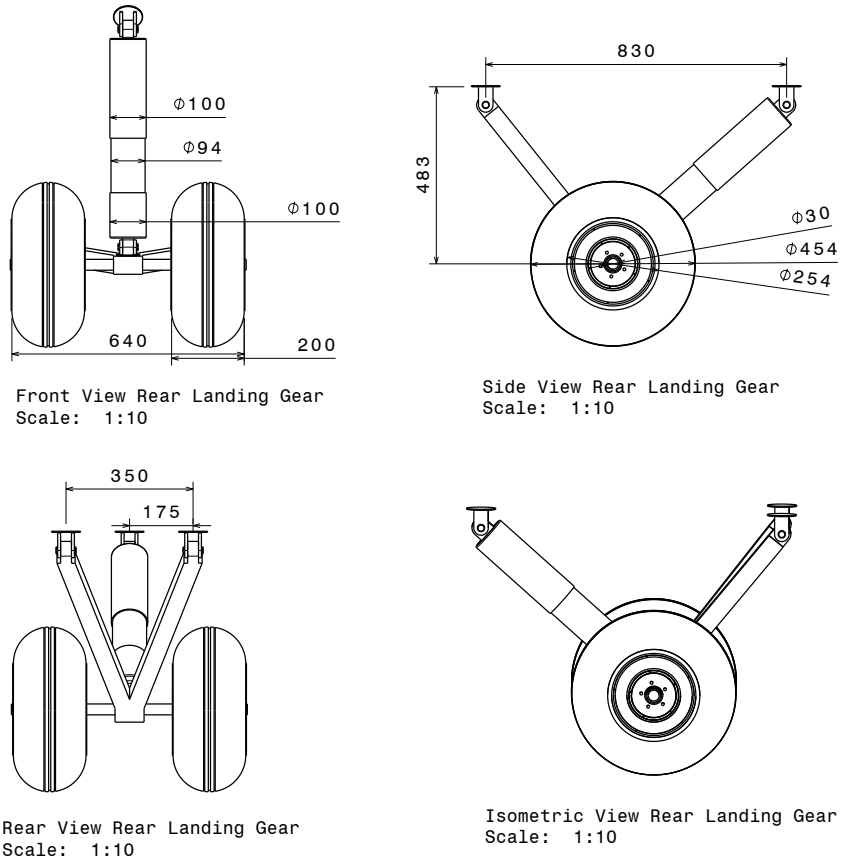

Figure 8.32: Rear landing gear configuration

For the rear landing gear also a shock breaker is used which will also have a displacement of 0.2 [m]. It has to be noted that since the shock breaker is not placed vertical here, the helicopter will not be perfectly horizontal if both landing gears are fully pressed. This will not be a problem since the landing gears are overdesigned for normal landings. The landing gear not retracted will have the same height as the front landing gear and will have a height of 0.54 [m], using the shock breaker to the full extend.

It has to be noted that the forces will be a bit higher using Equations (8.29) and (8.28) with a distance of 0.17 [m] (0.71–0.54 [m]). Using those formulas this results in a deceleration of 4.3g, including the safety factor of 1.5. At the front landing gear it was noted that the landing requirements are far less important than the loads occurring when driving. This is the case since lateral forces cause failure at lower loads. For this reason it is assumed landing will cause not problems in the rear landing gear since this is more robustly designed than the front landing gear. With the current knowledge within the design group, it is not possible to divide the loads over the components of the landing gear. Having three members carrying this load it must be definitely sufficient if the same material and thicknesses are used as in the landing gear at the front, as landing is not the critical condition.

9 Cost and Weight Analysis

The cost and weight analysis is shown in this chapter. To be able to perform a sufficient cost analysis, the weight of all sub-parts have to be known. Hence, first the weight analysis is explained followed by the component and total cost analysis.

9.1 Weight Analysis

During the concept phase of the project a weight and cost estimation is done for the concept. During the project a first iteration for the conceptual design is done, from this iteration a new weight and cost estimation is created. This estimation results from the design that is created during the initial conceptual design phase. The crew and payload weight is not changed during the conceptual design phase, due to the requirements. The equipment weights are based on reference data obtained from [60], which are based on the MTOW of the vehicle. This is the same for the components classified under "other". The landing gear is designed in more detail. The components classified under "power train" and "propulsion" are designed in detail in this report and are explained in Sections 4 and 4.2.5. The weight for the hub and the rotor blades are calculated in the structural design, which can be found earlier in this report. The final weights can be found in Table 9.1.

It has to be noted that the propulsion subsystems have a quite accurate weight estimation, the rotor and hub weight can be considered as accurate since a reliable structural analysis is performed on the rotor and the hub is sized tolerably well. Since the fuselage structural analysis is only conducted to point out stress concentrations, this is not sufficient to estimate an accurate weight. The current estimations are thus not very supported but seem valid, with respect to the weight of a created airframe. The contingency within the controls, instruments, furnishing & equipment and airco and anti-ice are assumed to be quite low, since they are off the shelf solutions which can be accurately based statistics. For the cost analysis, most components are valued with respect to weight, so the same accuracy can be taken into account. Since the weight at the end of this iteration does not change considerably, for the next iteration the weight and thus the design will not change significantly.

9.2 Cost Analysis

In this section, the overall production cost of the vehicle will be determined. In this cost analysis, first the component costs are calculated and secondly the total cost is computed by including the in-house assembly of the vehicle. The cost analysis in this section is based on statistical data and should therefore be seen as an initial estimate for the vehicle costs.

9.2.1 Component Costs

In order to penetrate the market of EMS vehicles, the designed vehicle should have a cost that is as low as possible and preferably lower than current vehicles. Using [60] and the different weights, as calculated in Section 9.1 the costs are determined. Using statistical formulas, the cost per component can be determined and hence the final cost per produced unit can be calculated. Note that the calculated values in [60] are in 1977 US Dollars. Hence, these values need to be converted to 2013 euros by using the inflation over these 36 years. The inflation of the US Dollar from 1977 until 2013 equals 395% and is converted to euros using the conversion rate of 0.7634575 euro per dollar (consulted on June 24, 2013). When producing more vehicles, the cost per unit will decrease due to mass production effects. The costs per component are depicted in Table 9.1.

The electric motors are estimated to cost €11,452 [19]. Since only the specifics of the prototype are known, these are used to calculate the cost for the amount which is required. If only the prototype is used, 25 motors are required in the front and 35 motors are required in the rear. Since for pre-rotation

two motors are needed and for driving four motors, this results in 126 motors per eGyro. The decrease in costs due to high volume production is based on [60], where the decrease in power plant costs are defined.

Since the generator costs are very hard to estimate, the costs are estimated to be €267,210. This is calculated using the same decrease in costs as for the power plant, based on reference [60], which results in a generator of €77,109 when 200 units are ordered. The battery costs are calculated on the cost density which is stated in Section 4 and are stated in Table 9.1.

When adding up all the component costs, the final vehicle cost will end up to be € 450,000, when assuming a production of 200 vehicles. When producing 200 vehicles, the in-house production equals € 226,000 for each vehicle, so total production cost will be € 676,000.

The fuel costs are not part of the unit costs, however they do influence the operational costs of the vehicle. The fuel costs are estimated by converting the fuel weight to fuel volume and the price of the fuel. Jet fuel type A is used to power the engine, this fuel weighs 0.8 $[\frac{kg}{L}]$ and the price of this fuel is 292.8 $[\frac{cts}{gal}]$ (consulted on June 24, 2013). The fuel costs that are found for each mission are found to be € 250, using the conversion factor to euros mentioned above. Figure 11.3 in the Diagrams Chapter shows an AND tree to identify all elements that contribute to the total development and production cost of the eGyro. In Table 9.1 an estimation for the assembly and component costs can be seen, where all components are elaborated on. Since this concept will result in a new compound vehicle it is not reliable to estimate research and development costs so here is not yet elaborated on.

For further information on weight and costs of the ducted fans, use can be made of the Mid-Term Report [4].

Table 9.1: Cost and Weight Overview

Component	**SubComponent**	**Weight [kg]**	**Cost [€] [60]**
Power train	Engine	132	55,000
	Generator [8]	71.3	77,000
	Motors Front [19]	31.7	134,000
	Motors Aft [19]	43.4	
	Batteries [7]	257.1	10,000
	Fuel	311.5	230
	Extra	10	-
Propulsion	Ducted Fan Front	30	22,000
	Ducted Fan Aft	40	
	Rotor	43.08	6,800
	Hub	29.98	
Fuselage	Fuselage	100	55,000
Equipment	Avionics	22.68	32,000
	Controls	7.2	38,000
	Instruments	8.17	
	Furnishing & Equipment	14	4,000
Crew and Payload	Crew	240	-
	Patient	100	-
	Medical Payload	225	-
Other	Landing Gear	95	5,500
	Airco & Anti-Ice	13	11,000
	Manufacturing variation	6.4	-
In houseAssembly			226,000
Total		1831.5	676,000

10 Development Characteristics

The development characteristics consist of several separate parts that will be discussed in this chapter. First, the verification and validation of the eGyro will be discussed. Secondly, the RAMS criteria are elaborated on, followed by the operations & logistics concept description. After that the risk assessment and the sustainable development strategy are explained.

10.1 Verification and validation

In this section all the programs used for the design process will be verified and validated. This is done to proof that the proposed design will meet the requirements.

10.1.1 Verification

An elaborate market analysis is performed to adjust the product towards primary costumer needs. From that and the defined requirements all necessary subsystems are further investigated. For instance, the driving capability of the vehicle is found to be a high priority costumer preference. The programs used for the design process are verified. In case of errors, debugging and analysis of the used theory is performed. The models are build up using separate blocks, which are checked independently. For instance, for the auto-rotation part, the block structure is given in 5.7. Also, in the transition script each phase is checked separately before running the script as a single unit. In the same manner, the entire model as one unit is tested in every script to eliminate possible transition errors within the models. Furthermore, the used theories are checked for their validity and limitations, which could lead to output inaccuracies.

10.1.2 Validation

Requirement validation

All the requirements stated in the requirements section are validated. First, it is checked whether they are verifiable. In most cases, the requirements are defined to be exact values. However, some of them are not suitable to be defined in numbers, like for instance hovering. In these cases, the clearest possible definition is given instead. Second, all requirements have to be achievable. This means that access is required to sufficient resources, such that challenging but realistic goals are set. For the eGyro, the resources are limited because it is an uncommon compound vehicle. On the other hand, many concepts with similar mission goals are already on the market. Therefore, the requirements can be compared to these existing vehicles. In addition, the requirements are build up on a logical basis. Finally, the requirements are made such that they are integral and definitive. Hence they are clearly understandable and provide all the information needed.

Each requirement has to be verified with a real life test. For the endurance for example, it should be tested if the vehicle is really able to fly for two hours uninterrupted. If this is not the case, adjustments have to be made and in the worst case, the complete design iteration has to be started over again. For the cruise speed the same holds. A real life test has to be performed to prove that the vehicle can reach its required flight velocity. Some subsystems can be tested separately. For instance the thrust that the ducted fans have to deliver to achieve the various speeds and required stability.

Model validation

Another important validation segment defines the validation of the model. Before starting the design process, extensive research has been performed to get an overview of possible existing solutions. Hence, experience from other research groups has been integrated in the design strategy. This is considered to be a crucial step, to make sure that the new integrated technologies are going to be feasible in the end. All created models have been checked extensively for proper functioning. Various inputs have been

used in order to check realistic output consistency. The output values are compared with existing values whenever possible.

Product Validation

At this stage, no product validation has been done yet. Except for comparing results achieved during the design phase with results of similar concepts. The main thing that has to be tested is the transition phase. That is due to the fact that the transition phase is a yet uncommon maneuver and could lead to catastrophic consequences in case of unpredictable vehicle behavior. In particular this involves the rotating mechanism of the aft located ducted fans. A way to check the functioning of this mechanism could involve a full scale model test where the vehicle is attached to ropes. In this way, unwanted movements can be more easily controlled, while enabling full degree of freedom test with realistic thrust setting. Next to that, a simulation program has to be made. Such that the vehicle can be flown under safe conditions without compromising on stability and pilot handling tests. Also, a simulator will make it possible to test scenarios that would be too dangerous to execute for the first time in real life, such as the transition phase. Another critical test to be performed is the driving capability. It should be confirmed that the vehicle with its dimensions and driving components is capable of maneuvering on regular streets. For the drag and auto-rotation characteristics wind tunnel tests are essential, in order to confirm the current calculated values. For the operational suitability, it is advisable to check the vehicle in terms of practical handling characteristics. This involves the equipment set up and accessibility of important components. To validate the structures computation, destructive testing of critical components like the rotor has to be performed.

10.2 Reliability, Availability, Maintainability and Safety

This section describes the so called RAMS characteristics of the eGyro. Every aspect of the RAMS will be discussed briefly.

10.2.1 Reliability

Since the vehicle needs to stand by for emergencies 24 hours a day and lives are at stake, the vehicle reliability is one of the major aspects which needs to be taken into account. Structural components are designed using the fail-safe design principle. Hence, whenever a component fails, the eGyro is able to finalize the mission and return safely to the base. For example, the ducted fans and the auto-gyro rotor are designed using this principle, since these are the most critical components of the vehicle. During missions, higher risks are taken compared to normal civilian flights, which results in a vehicle where high reliability is required to ensure safety, which is another RAMS characteristic. Therefore, the vehicle is designed to be very reliable in terms of the VTOL performance, since this is the mission part which is the most critical in terms of safety.

10.2.2 Availability

In contrast to general aviation aircraft, EMS vehicles have to be available 24 hours a day, seven days a week. This means that replacement and refueling have to take as short as possible, to be able to take off in case of an emergency alert. Another major part which influences the availability is the maintenance, which will be discussed below. Designing an aircraft which needs few maintenance is desirable. Currently, the maintenance for the EC135 helicopter equals a short maintenance of four hours every 100 flight hours. The simple design and mechanics of the eGyro reduce the maintenance and therefore increase the availability of the vehicle. Since the fail-safe design is used for certain components, less maintenance is needed and the maintenance schedule can be modified to reduce the amount of maintenance operations. The turn-around-time is also of major importance to the availability. This is the time from landing back at the base up until the moment the vehicle is able to fly a new mission. It consists of refueling time, refilling time of the medication and equipment on board and possibly the exchange of crew. In total this will take less than five minutes.

10.2.3 Maintainability

For fast maintenance, parts which need to be regularly exchanged should be easily accessible. This results in several access locations for checking integrity and correct operation of systems and, if necessary, repairing or replacing systems. It is important that maintenance is scheduled in advance, since unforeseen maintenance might result in life threatening situations if operations have to be canceled. Excluding unforeseen maintenance completely is not possible, such that range and operation areas have to be adapted for a malfunctioning vehicle. For the eGyro, explicitly, the amount of parts that have a large failing chance is kept as low as possible. Therefore, the maintainability need is decreased in comparison to the current EMS vehicles.

10.2.4 Safety

Safety is crucial, since higher risks are taken when lives are at stake. These risks are finally evaluated by the pilot. This means that the pilot has to fully trust the aircraft and is able to evaluate the risk thoroughly. To be able to do this, the aircraft has to be extremely reliable. The safety of the eGyro is enlarged by the use of an auto-gyro. When, for example, an engine fails during cruise flight, the vehicle is still able to land on auto-rotation. This type of safety is elaborated more in Section 4.4. An auto-gyro is also easy controllable and stable, making pilot errors as well as wind gusts or bad weather less critical when flying the eGyro.

10.3 Operations & Logistic Concept Description

The operations and logistics of the eGyro can be represented in a flow block diagram that illustrates the use and support of the system. The diagram for the eGyro that includes the maintenance and ground support can be seen in Figure 10.1.

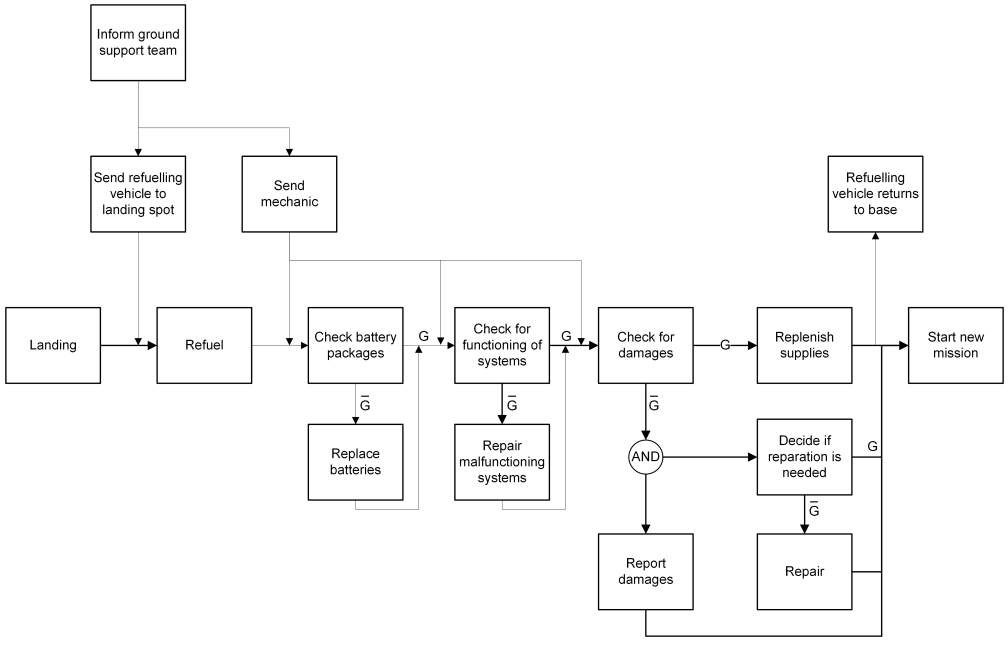

Figure 10.1: Operations & logistics flow diagram

The arrows show the flow of each operation for the maintenance and support of the vehicle. The operations that are involved with checks are accompanied by an outcome, which can be either sufficient G or that a flaw is detected $\bar{G}$. In the case of a defect the system has to be replaced or repaired. The checking and reparations are done by a mechanic.

10.4 Risk Analysis

In this chapter, the risks that have to be considered during the design are outlined, since with a different propulsion system a lot of risks changed with respect to earlier design phases. The risks incorporated with the power train are earlier stated in Section 4.4. Other risks will be stated below to complete the risks map, which can be found in Figure 10.2.

8. Electric Power Failure

The ducted fan will be operated using a fly-by-wire configuration. In case of electric power failure for flight systems this will cause problems. For this reason the rotor will be mechanically controlled to be able to descend safely. The landing space required in this case is a bit bigger, since the rotor does rotate until the vehicle has landed.

9. Man-Machine Interface

For the eGyro, the control of the vehicle is very important due to the ducted fan configuration. When wrong information is given to pilot about the flight conditions, the vehicle controlability can be lost. Furthermore, for the auto-gyro, the man-machine interface is not causing severe problems since the auto-gyro is easy to control and will be mechanical controlled.

10. Structural Failure During Flight

The chance of structural failure during flight will not be very large. The highest problems for structural failure will be the ducted fan and rotor structure. These will be designed safe-life to decrease risks.

11. Structural Failure During Take-off and Landing

During take-off and landing, the structural failure of ducted fans will be very catastrophic since the vehicle is not able to produce lift and be stable. Hence, it is very important that the possibility of structural failure is kept low since the severity of the failure is high. These parts will be designed safe-life to ensure the probability is very low.

12. Problems Due to Spectators

The eGyro will operate in crowded and highly populated areas. On these locations, accidents will draw a lot of attention and will attract people. Since the fans are nested in a duct and the rotor is not rotating when taking off at the crash site, this decreases the danger induced by spectators. Although this risk was stated to cause serious consequences, it is now downgraded to "low".

13. Problems Due to Human Failure

Problems due to human failure are pretty rare during the operation of EMS vehicles. The pilots are very well trained and fly the vehicle often, but do conduct dangerous missions. Human failures cannot be excluded and therefore there will always be a small chance of human failure. Depending on the type of human failure, the severity of the accident is varying.

14. Increased Payload Weight

The chance on increasing the payload weight is moderate since the patient is estimated to weigh 100 [kg]. It is possible that extra equipment is needed for specific missions in combination with the Flying Hospitals project [2]. At the western market the equipment is fixed, such that payload weight will not increase often.

15. Increased Payload Size

The payload size and weight are changing simultaneously and the risk will therefore be evaluated identical.

16. Failing Pitch Adjustment of the Aft Ducted Fans

Failing pitch adjustment in the transition phase means that the mission will be aborted and landing will be started using the rotor.

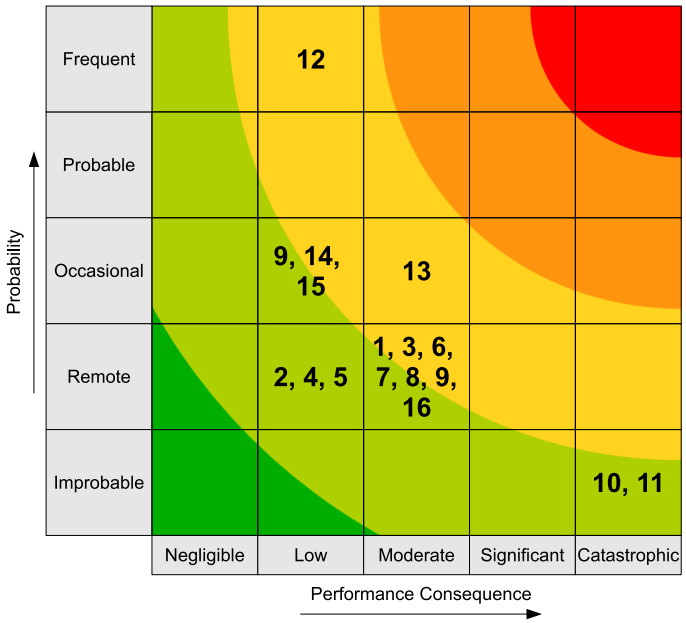

Figure 10.2: Risk map eGyro

10.5 Sustainable Development Strategy

For the eGyro, as an air transportation vehicle of the future, sustainability is an important aspect. Noise emissions, air pollution and a sustainable material selection are all aspects that are considered during the design of the eGyro. The eGyro is designed as a "green" vehicle, using a sustainable development strategy as described below.

The noise emission and the air pollution of the eGyro are reduced due to its hybrid design. This hybrid design reduces the noise emission by means of the low noise emission of electric motors. Next to the electric motors also the ducted fans produce less noise compared to other propulsion methods that can be used for VTOL operations. Thanks to the electric motors and ducted fans the eGyro only produces 80.6 [dB] during VTOL operations and 78.3 [dB] during cruise, as explained in Section 7.5 on the performance of the eGyro.

Furthermore, the air pollution emitted by the eGyro is also reduced due to the hybrid design and the ducted fans. The hybrid design of the vehicle causes the vehicle to consume less fuel compared to a vehicle with other propulsion systems. Next to this, due to the high efficiency of ducted fans, compared to other propulsion methods that are used for VTOL operations, the air pollution is reduced even further. Further details on the pollution can be seen in Section 7.6.

Finally, the materials that are used for the eGyro can be re-used for other purposes. The batteries need to be of high quality and when the batteries are no longer considered efficient for eGyro purposes, they can still be used for other purposes that require less efficient energy storage. Furthermore, the materials that are used can be re-used as well. The carbon fiber that is used in the eGyro is a high quality carbon fiber. When parts need to be replaced, the old parts made out of carbon fiber can be shredded and the fibers are still strong enough to be re-used for other industries. For example, these fibers can be used for other engineering purposes where the loads are lower or even for low weight production of music or sports equipment. Another component that can be re-used is the metal that is used for the engines, which can simply be remelted and used again for other metal products. Most of the materials that are used for the eGyro can thus be re-used in similar ways in other industries.

11 Diagrams

Several diagrams are created to show the flow of a system or the breakdown of a structure of the eGyro, which are discussed in this chapter. The first one is the Functional Flow Diagram, followed by the Functional Breakdown Diagram and the Cost Breakdown Diagram. Finally, the software and hardware diagrams are discussed.

11.1 Functional Flow Diagram

In comparison to the Baseline Report [3] the FFD is changed. As stated in the Baseline Report [3], this diagram 11.1 represents the functions that are carried out during the mission. Different levels indicate the importance of the functions and all lower level functions are dependent on the ones above them. Driving is now part of the approach phase and is the last part. Although it is listed in the FFD, it is not always part of the mission since the requirement to drive depends on the accident site. In case the accident site is too small to directly land on, it is necessary to land on a larger area and drive to the site of the accident. Also, the driving is now a part of the first aid medical assistance system as well, but only in case of a too small accident site. In that case the last part of the first aid medical assistance function consists of driving back from the accident site to the landing area.

11.1.1 Level 1: Pre-operational Inspection

Analyzing the functional flow diagram the first level function is the pre-operational inspection. This is crucial since the vehicle is not allowed to depart if it has not been checked for safety. When inspecting the vehicle before take-off the structural integrity should be checked first, since the structure is a fundamental part of the vehicle. If there are deficiencies in the structure these should be repaired immediately before continuing the inspection. The next steps are starting the systems, performing some pre-flight checks and checking the medical equipment. If equipment is missing or systems are not working these should be filled or fixed immediately.

11.1.2 Level 2: Departure

The next level in the functional decomposition consists of the departure. The associated functions are preparing the systems for the flight, turning the engines on and taking off.

11.1.3 Level 3: Cruise

This is followed by the cruise phase of the flight. The first functions in cruise flight are the actual flight, the communication with air traffic control and navigation. These functions are related to each other by an AND symbol since they are dependent on each other, and can only be carried out together. The sub-functions of flying consist of the power supply to the subsystems, the processing of the control inputs and an interaction of stability maintenance, providing thrust and providing lift. The stability maintenance is also related to the navigation, which gives indications for the orientation of the vehicle.

11.1.4 Level 4: Approach

The next level in the breakdown is the approach, starting with the search for a proper landing area. The next functions are the deployment of the landing gear and the notification of the crowd by an alarm. These functions are related by an AND symbol since they have to be carried out together for safety reasons. After this, the actual landing can take place. Depending on the type and size of the ground surface of the accident site the vehicle may land on an area nearby the accident site and then drive to the location of the accident. Therefore this is the next function and is optional.

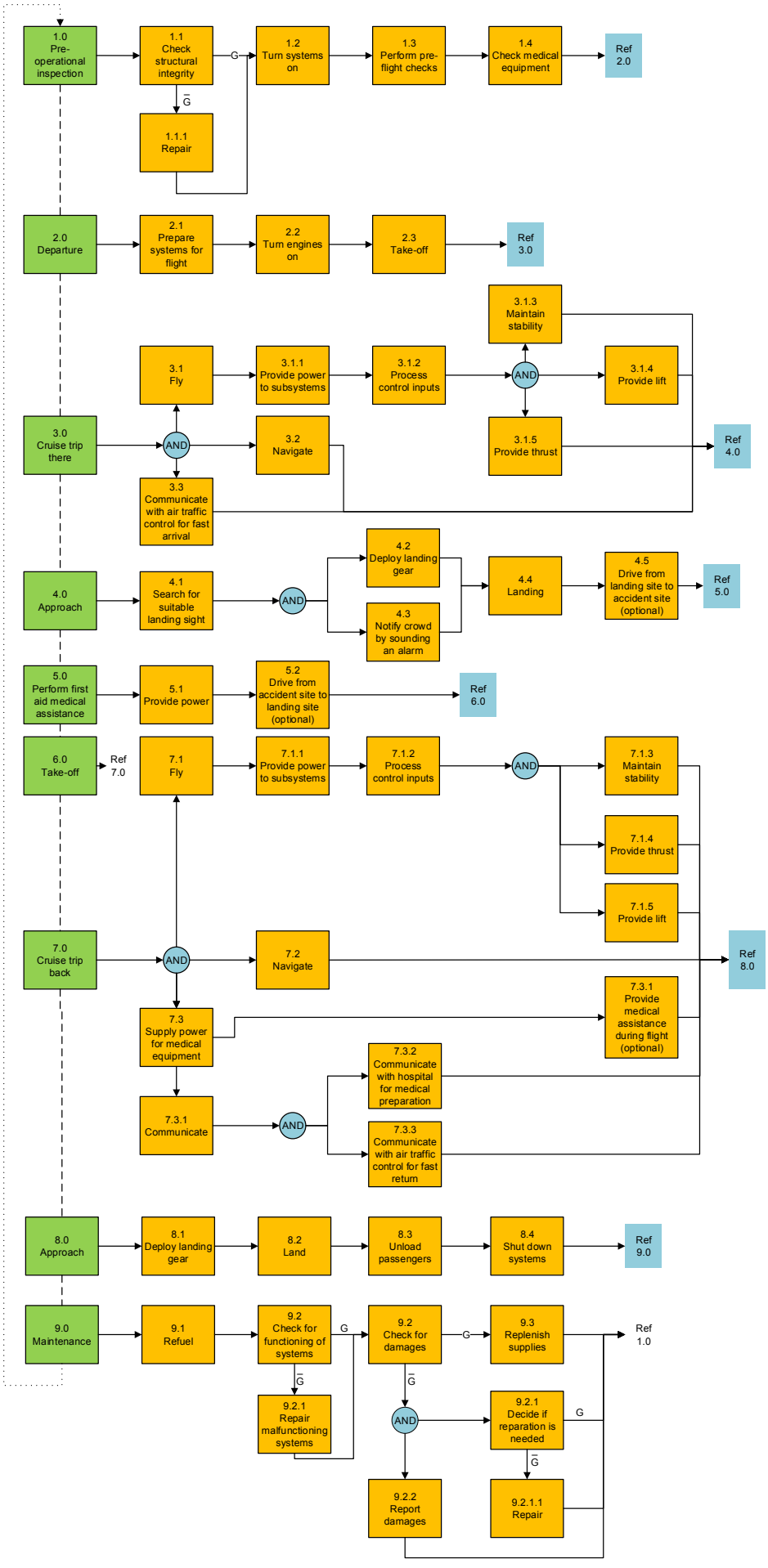

Figure 11.1: Functional Flow Diagram

11.1.5 Level 5: First Aid Medical Assistance

Continuing the functional breakdown levels, the next level is the medical aid. Power may be needed for equipment, used for medical help, and if the aircraft is not able to take-off on the accident site it has to drive back to an area in which it can take-off properly. Therefore this is the next optional function.

11.1.6 Level 6: Take-Off

After medical help, take-off takes place, consisting of three functions, similar to those in cruise: flying, power supply to subsystems and control input processing, which is in its turn also interrelated to stability maintenance and thrust and lift supply, similar to the cruise phase.

11.1.7 Level 7: Cruise 2

The next breakdown level is the second cruise phase, the one back to the base. The three interrelated functions here are the flying, navigation and power supply for the medical equipment. Communication in different forms is the next function here.

11.1.8 Level 8: Approach 2

The eighth and second last breakdown level is the second approach, this time the approach of the base. Similar as in the first approach, the deployment of the landing gear is needed first, this time without the search for a landing area. Afterwards, the vehicle can land, unload the passengers and shut the systems down.

11.1.9 Level 9: Maintenance

The last level is the maintenance. This consists of refueling the vehicle, system checks and possibly system repairs, and damage checks, possibly together with repairs and damage reports.

11.2 Functional Breakdown Diagram

The Functional Breakdown Diagram (FBD) in figure 11.2 shows the most important tasks that are performed during the mission in a breakdown tree. These tasks consist of the functions that satisfy the stakeholder, as presented in the FFD. The FBD shows all the functions of the FFD in a hierarchic way. This is done by dividing the functions in groups, which can be used for the design of the different subsystems of the vehicle. The functions are decomposed in such a way that the original function can be reconstructed with the sub-functions.

Performing the mission is of course the most important task of the vehicle. The mission is decomposed into flight operations, driving operations and providing medical services. Each of these functions is divided into sub-functions. For the flight operations, for example, these sub-functions are structural support, power, controllability and performance. If possible, these sub-functions are subdivided into even smaller functions. Those are shown in the yellow boxes. Although the yellow boxes are listed above each other, they are all on the same hierarchic level. The diagram is an updated version of the one in the Baseline Report [3]. Since driving is now a primary requirement, it is also included as a separate function in the FBD.

11.3 Cost Breakdown Diagram

In Figure 11.3 the Cost Breakdown Diagram is shown. Since this shows the costs for the developers and not for the user, the production costs calculated and stated in the table below can be consulted.

11.4 H/W and S/W diagram

In this chapter the hardware and software diagrams will be discussed. These diagrams are made to illustrate the relations between the different components of the eGyro. Overall they are meant to improve the understanding of the system.

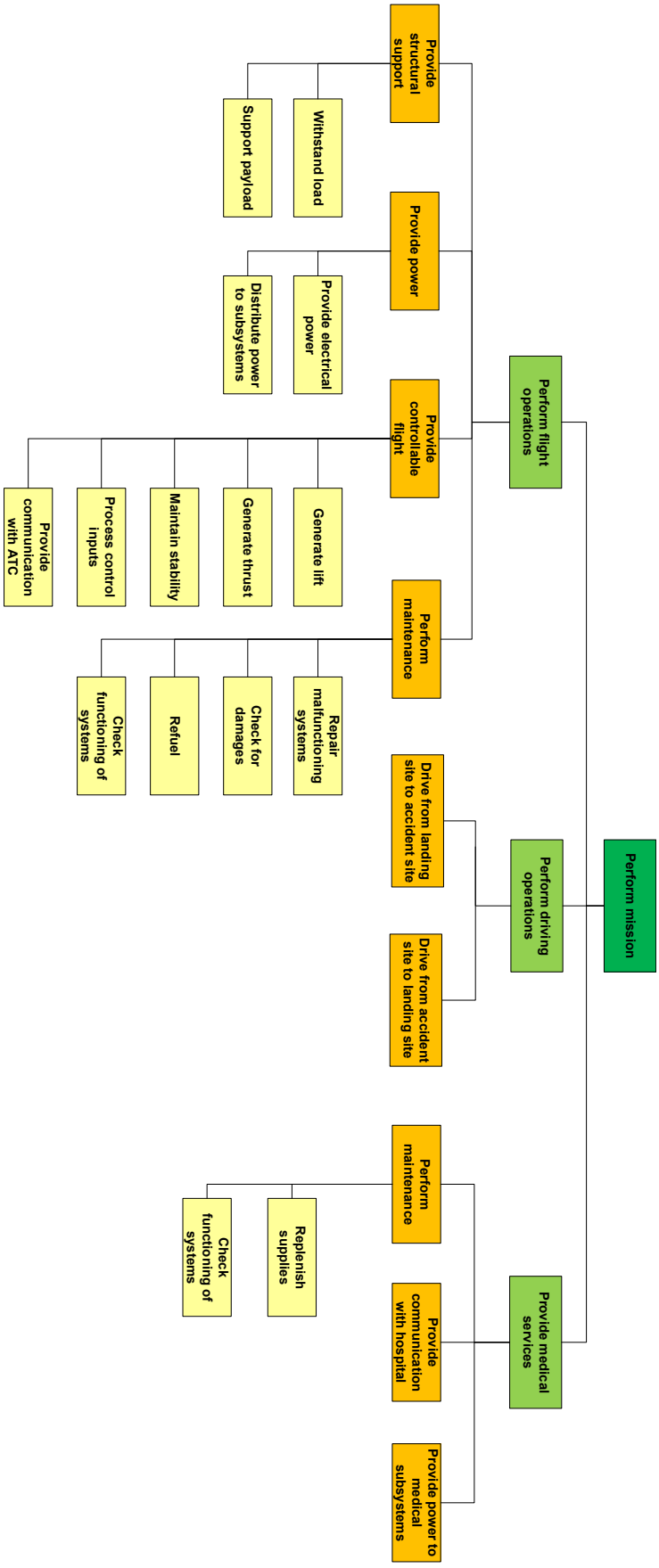

Figure 11.2: Functional breakdown diagram of the eGyro

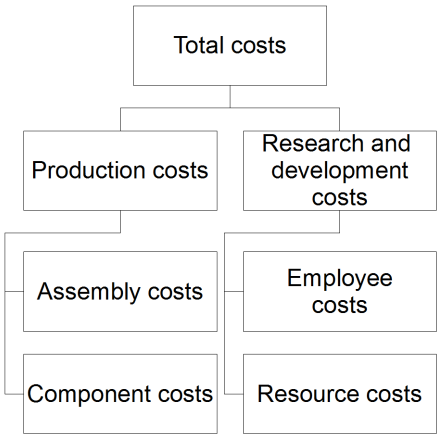

Figure 11.3: Cost Breakdown Diagram

11.4.1 Hardware diagram

The hardware diagram given in Figure 11.4.1 shows all the main hardware components and their relations. In the hardware diagram the airframe is centered, because it is the component that holds all systems together. From there, different sub-components, like the landing gear, are listed. The landing gear is again subdivided into struts, wheels and an electric motor.

An important component is the flight control system. It has a control input provided by the sticks which are controlled by the pilot. Two sticks are present in the cockpit, one mechanical stick for the hub control during transition and cruise, and one fly-by-wire stick for the vehicle control during VTOL operations and the transition phase. During VTOL, the control system checks the pilot inputs and the vehicle attitude and transfers this data to an appropriate rotation of the aft ducted fans, as well as a proper power setting for each ducted fan. This is done by the computer to keep the vehicle stable without much pilot effort. The stick for hub control is mechanical and can operate without any electric power available. This is chosen for safety reasons. However, the flight control systems give feedback to the pilot via this stick during the transition phase, to guide the pilot and make sure that no awkward movements are made. The tail is also a control device controlled by the flight control system. In the two vertical tails a rudder is positioned. The horizontal tail can be trimmed as a whole. These movements are all done by the flight control system, reducing pilot effort required.

The electric motor which drives the ducted fans is powered by the batteries or directly via the generator. The generator also charges the batteries. The batteries can also be charged from another source when the vehicle is stationary. The generator is connected to the engine to be able to generate the required electrical energy during cruise. The airframe provides a structure for the medical equipment. The on-board computers get their power from the battery and receive or send data from the GPS-receiver and communication antenna.

11.4.2 Software diagram

The software diagram of the eGyro is shown in Figure 11.4.2. The software of the aircraft consists of all computer based programs that control the motions and stability of the aircraft. The main part is the fly-by-wire interface that yields outputs for the flight control. The trim, rotor movement and ducted fan operations are all outputs of the fly-by-wire interface. The response of the vehicle to these control outputs is the feedback to the fly-by-wire interface that has to provide signals for steady flight conditions and maneuvers. The fly-by-wire interface interacts with the position tracker interface as well. This position tracker interface is receiving signals from GPS-software that navigates the vehicle during flight. Furthermore the fly-by-wire interface receives control inputs from the pilot and transfers these to appropriate vehicle responses.

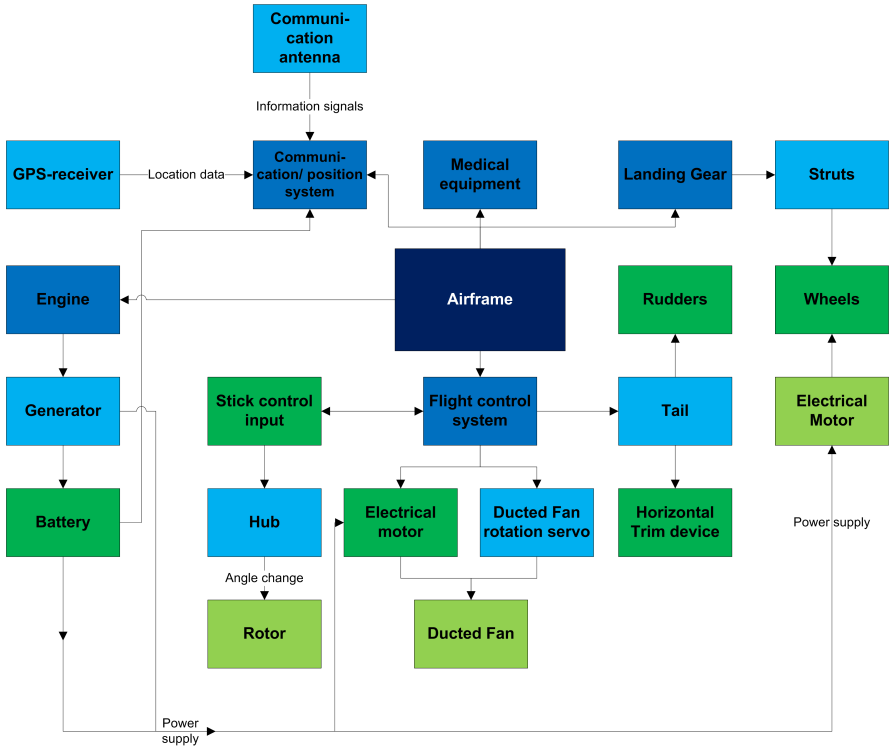

Figure 11.4: Hardware diagram showing the relations among the subsystems of the eGyro

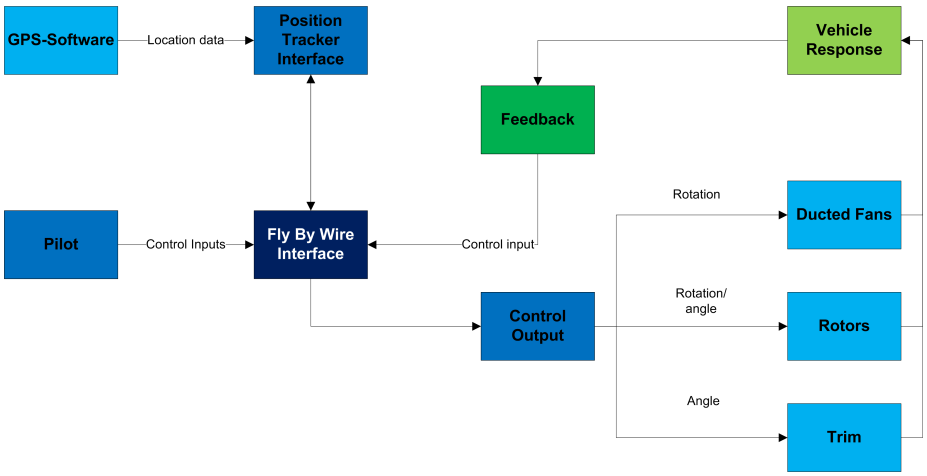

Figure 11.5: Software diagram of the eGyro

12 Recommendations

The recommendations that are made during this project phase for further development of the eGyro are discussed in this chapter. First, general and specific design part improvements are suggested. Finally, the project design & development logic is presented.

12.1 Suggestions for Improvements

In this section, suggestions for improvements of the eGyro for a next iteration will be stated. Firstly, general improvements and comments for the eGyro are stated. Secondly, every design discipline will state the improvements that are possible for the design part that these design teams are responsible for.

12.1.1 General Improvements

In this subsection, general improvements for the eGyro are stated. To improve the vehicle it should be investigated if it is beneficial to also turn the front ducted fans 90 degrees during cruise. It is now assumed that this would decrease the drag during cruise. On top of that, the aft ducted fans will need to produce less power, since also the front ones are providing forward thrust. This option has not been investigated thoroughly due to the fact that this would change the aerodynamics, the performance and the propulsion calculations. This would not have been possible in the given time limit, since the front and aft ducted fans influence each other considerably. In the beginning of the design process a lift over drag ratio of 4.5 is assumed. However the final lift over drag ratio obtained from the aerodynamics calculations is slightly lower. This means that the design iteration would actually have to be done again with the new lift over drag ratio implemented. This is a post DSE process, since this process has to be repeated until the input and output of the design iteration correspond within acceptable limits. Finally, the hub could have been made higher such that the tail can be mounted higher. This is depended on the clearance needed for the rotor, which is a result of the minimum airspeed. The higher mounting of the tail would increase the space in the cabin.

12.1.2 Specific Design Part Improvements

In this subsection, specific design part improvements for the eGyro are stated. In the subsections below, every design team will address the improvements that are possible for the design parts where they are responsible for.

Aerodynamic Improvements

The aerodynamic properties of the rotor have been calculated with a program that deals with auto-rotative conditions. Due to a lack of time some assumptions have been made, e.g. for the blade angle of attack and the drag estimation. If more time would have been available the drag coefficients of the different parts of the vehicle could have been estimated more accurately. This would require a more detailed design of the different vehicle parts. In this way more realistic drag estimation can be made with more extensive knowledge on materials, shapes and wind tunnel tests. Furthermore the angle of attack could have been obtained by iterative procedures instead of by statistical equations. Moreover the vehicle's fuselage and rotor could have been optimized in more detail for aerodynamic purposes such as drag reduction. In terms of the way of working, a more structured plan can be made before starting the calculations. This plan then outlines clearly which rotor characteristics have to be calculated and how they are related to other parameters in other disciplines, such as structures and control and stability.

Power Train Improvements

The powertrain is currently designed with the assumptions for future development of components. The feasibility of the component specifications are checked, but sizing might be designed more accurately. As

said before, the charging and discharging capabilities of the battery package are depended on the circuit lay-out and should be checked in the detailed design. It has to be noted that the incorporated engine, capable of delivering kinetic energy is not very efficient and silent since it is a turboshaft engine. For this power consumption piston engines and wankle engines are currently not sufficient, but with further development might result in a different engine selection to perform better at noise emission, efficiency en reliability. In this phase of the design it is impossible to construct the circuit and control system which controls the power to the motors, this should be designed very accurately and reliable in the detailed design.

Stability Improvements

For the stability a model is made. The model used to check the stability, performs as desired, but is only a three degrees of freedom model. To be able to check the stability more extensively, a six degrees of freedom model has to be made. This can be done in the next design phase. Then the model will be more accurate since the design of the vehicle will be more detailed and there a three degrees of freedom added. Using this analysis the vertical tailplane can be sized and designed. Also, only the stability at cruise speed is checked, for next design iterations all relevant speeds have to be checked.

Structural Improvements

The structural analysis as it is done during the conceptual design can only be used as a preliminary analysis. For the detailed design phase, an airframe has to be analyzed using finite element computations. A possible airframe is shown in Figure 12.1. In the airframe there is accounted for locations of doors, windows, ducted fans and the rotor mount.

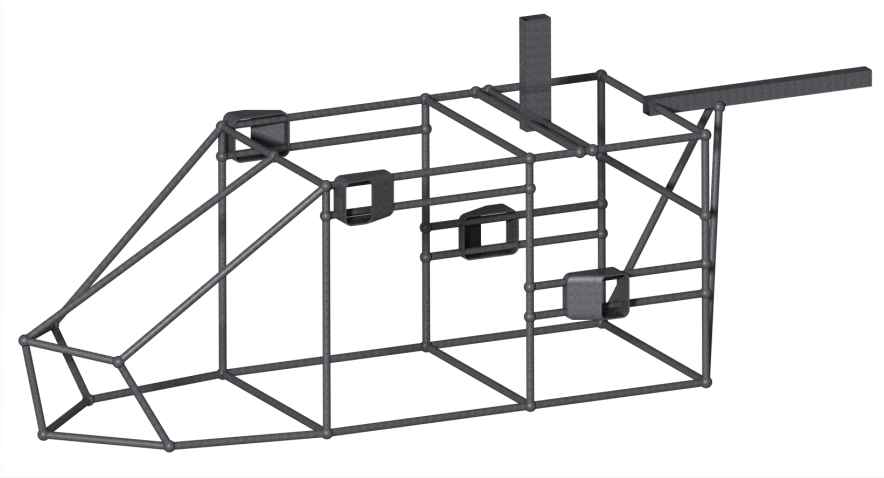

Figure 12.1: Suggested fuselage airframe

The rotor box analysis should be performed including dynamic effects and vibration calculations. The same holds for the rotor mount. The rotor hub should be analyzed using CFD computations, to determine accurate values for the loads on the hub. Weight reduction can be achieved by optimizing the hub design using that method. Also elaborate fatigue computations have to be done in the future. Improvements for the landing gear will mainly concentrate on the shape of the landing gear. Due to limited time frame that is available for the conceptual design, the shape of the landing is chosen based on the complexity. However, if more time is present, a more effective and ergonomic design of the landing gear can be used. The main advantage of using a more effective design will yield a lower weight of the landing gear and it might be possible that the landing gear can withstand higher loads. Next to this, when more time is available, the ground clearance of the vehicle can be minimized in order to improve the accessibility of the eGyro.

Performance Improvements

Preliminary noise calculations have been done to arrive at EPNLs. These numbers can be computed more accurate if there are some more detailed ducted fan noise calculation methods. Furthermore there can be looked more extensively into different propeller profiles concerning noise reduction. A noise contour could be made for some take-off profiles, when some directive analysis have been done. The emission numbers are now mostly based on power settings. Especially the emission numbers during the VTOL phase are at this point quite rough. Furthermore the CO_2 emissions should be added.

After some more extensive aerodynamic calculation it would be possible to create a more accurate height-velocity diagram and a load envelope.

Several improvements can be made during the next design phase. First of all, the calculations can be made more accurate, including possible wind gust scenarios and avoidance maneuvers. Making a more complex optimization code could also further improve the transition phase time and save some time for the different stages. Furthermore the design should be able to respond faster in emergency situations. Therefore the max cruise speed has to be increased above 200 $\left[\frac{\text{km}}{\text{h}}\right]$. The first way to achieve this is to reduce the parasitic drag, by improving the aerodynamic shape. Also a retractable landing gear should be investigated for the next phase. Another option would be to make the rear fans slightly more powerful, such that they can provide more thrust during cruise. Finally, looking a little more into different propeller designs or fan shapes, to further increase the efficiency is recommenced for the upcoming phase. A higher cruise speed would be very advantageous long range missions.

12.2 Project Design & Development Logic

The project design and development logic is a block diagram that shows the steps in the design process that are taken after the DSE is finished. It is an overview of design milestones from the conceptual design to the point the eGyro is fully operational. Figure 12.2 shows the project design and development logic.

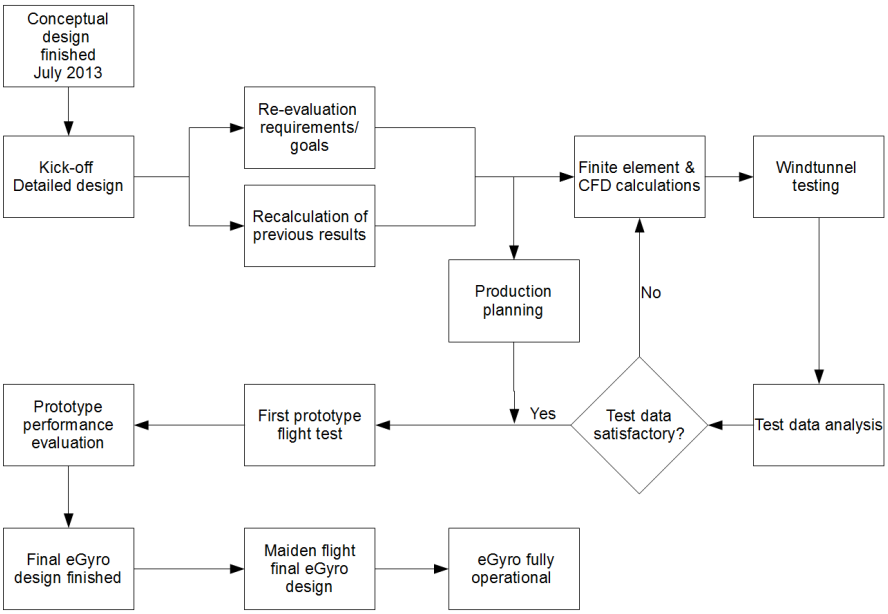

Figure 12.2: The project design and development logic. The diagram shows the milestones of the total eGyro design up to its operational use

13 Final Review of the eGyro

In this chapter, the initial requirements are re-stated and it will be checked whether these requirements are met or not, using a requirements compliance matrix. The feasibility analysis will give a short description of the outcomes of the requirements compliance matrix. Finally, a sensitivity analysis will be performed in order to check whether the eGyro will have a reasonable chance of being produced.

13.1 Requirements Compliance Matrix

In this section, the requirements compliance matrices are given for both the constraints as well as for the requirements, as stated in Chapter 2.

In Table 13.1 the primary and secondary constraints, as stated in Chapter 2, are listed. In Table 13.2 the primary and secondary requirements, as stated in Chapter 2, are listed. A further explanation on these tables is given in the feasibility analysis below. Note that certain values in the tables are not very strict, but are just described in a vague matter. Therefore, it might be hard to check whether all requirements are met.

Table 13.1: Requirements compliance matrix for the primary and secondary constraints

Requirement	**Initial Value**	**Final Value**	**Check**
EMS-CONS-P1: Speed	200 $\left[\frac{\text{km}}{\text{h}}\right]$	200 $\left[\frac{\text{km}}{\text{h}}\right]$	
EMS-CONS-P2: Range	250 [km]	442 [km]	
EMS-CONS-P3: Cost	As low as possible	€676,000	
EMS-CONS-P4: Number of passengers	4	4	
EMS-CONS-P5: Landing area	12 × 12 [m]	12 × 12 [m]	
EMS-CONS-P6: Response time	$\leq$ 30[min]	36 [min]	
EMS-CONS-P7: Sustainability	Low emission rates	Full hybrid flying	
EMS-CONS-P8: Endurance	2 [h]	2.26 [h]	
EMS-CONS-P9: Noise emission	80 [dB] at 300 [m]	78.3 [dB] at 300 [m]	
EMS-CONS-P10: Certification	Comply to FAA regulations	No complete check performed	
EMS-CONS-P11: Night operations	Operate at any time of the day	Operate at any time of the day	
EMS-CONS-P12: Wind speed	20.7 $\left[\frac{\text{m}}{\text{s}}\right]$ (daytime), 13.8 $\left[\frac{\text{m}}{\text{s}}\right]$ (nighttime)	Needs further investigation	
EMS-CONS-P13: Fog, rain and snow	Sight 100 [m] (daytime), 150 [m] (nighttime)	Achieved	
EMS-CONS-S1: MTOW	$\leq$ 3175 [kg]	1850 [kg]	
EMS-CONS-S2: Cabin area	$\geq$ 1.5× 2.5 [m]	1.5 × 2.7 [m]	
EMS-CONS-S3: Vehicle dimensions	$\leq$ 6× 6 [m]	6 × 6.1 [m]	
EMS-CONS-S4: Turn-around time	$\leq$ 5[min]	$\leq$ 5[min]	
EMS-CONS-S5: Type of landing area	Asphalt, sand and grass	Able to land on rough terrain	
EMS-CONS-S6: Team	10 persons	10 persons	
EMS-CONS-S7: Time	11 weeks	11 weeks	

Table 13.2: Requirements compliance matrix for the primary and secondary requirements

Requirement	**Initial Value**	**Final Value**	**Check**
EMS-TECH-P1: Maneuverability	Easily maneuverable in highly urbanized areas	Driving capability and stable VTOL operation	
EMS-TECH-P2: Accessibility	Easily accessible	Same ground clearance as current EMS vehicle and easy accessible parts	
EMS-TECH-P3: Stability/control handling	Easily controllable and stable	Stable vehicle and easy autogyro control	
EMS-TECH-P4: Communication	According to the FAA CS-27 book 1 part F [6] regulations and Dutch EMS (C2000)	No specific investigation done	
EMS-TECH-P5: Power	Sufficient power for all on board equipment	Sufficient power for all on board equipment	
EMS-TECH-P6: Drive	Drive for at least 1 [km] on all types of roads, from asphalt to dirt roads	Able to drive for at least 3 [km] on all types of roads, from asphalt to dirt roads and hills up to 10 %	
EMS-TECH-S1: Hovering	Able to hover	Able to hover	

13.2 Feasibility Analysis

In Table 13.1 with constraints it can be seen that almost every constraint is met during the design of the vehicle. However, for certain constraints, it is not possible to do an extensive research. The eGyro can not be fully checked for the FAA regulations since for certain components there are no existing regulations. However, the landing gear, for example, is checked for the FAA regulations and would probably pass the license test. Next to the FAA regulations, it is also not possible to completely check whether the eGyro can withstand the requested gust speeds or not. During the design, it is proved that the eGyro can withstand certain load factors, but this does not prove the full gust resistance of the vehicle. Also, the response time requirement is not met completely. In order to reach the outer borders of the operational area, a response time of 36 [min] is necessary. Hence, this response time is 6 [min] higher compared to current EMS vehicles. Finally, it has to be noted that the eGyro length is 0.1 [m] larger then it initially has been stated in the requirements. However, this small deviation has such a small impact, that it almost can be neglected.

Concerning the primary and secondary requirements, a lot of requirements are described in a vague matter. The maneuverability can be marked as a check since an auto-gyro is easily controllable and the driving capability of the vehicle has been subjected to an extensive research. The same holds for the power. It has been proved in Chapter 4 that the designed engines and generator will deliver the necessary power to operate all on board equipment. The communication has not been checked at all during the report, since there was not enough time available for this requirement during the project. However, the installation of such a communication system should not be a big deal during further research. In terms of accessibility, the vehicle performs well. The accessibility of the ducted fans and the landing gear is very easy since these parts are located on the outside of the vehicle and there exists enough clearance for them. The only part that might be hard to access is the engine of the eGyro. However, the engine in the current EMS vehicles is placed in the same matter and therefore the eGyro design is not more complicated.

Concluding from the constraint Table 13.1 and the requirements Table 13.2, it has to be noted that the eGyro is a very feasible concept. The eGyro meets almost every requirement or constraint and therefore the design satisfies the customer wishes and the project goals.

13.3 Sensitivity Analysis

This subsection describes the sensitivity analysis of the eGyro. In other words: the chance whether the eGyro could be produced in reality or not.

Considering the materials used in the eGyro and the techniques used for the eGyro, the concept is actually very feasible. The used materials are already produced and used in the aerospace engineering world at this moment. Next to this, the engineering techniques that are used are not very new. Therefore, there is no need for a very extensive research on the used engineering techniques. Hence, concerning production the vehicle seems to be very feasible to produce.

Next to the production side of the eGyro, the sensitivity analysis has to be performed for the market side of the eGyro. As mentioned in Section 2.6, the eGyro can be modified for many purposes. The wide range of possibilities ensures thus a very feasible concept. The market parties that might be interested are of such extent that also fund raising would not be a very large problem. The reasonable goal of production in 2024 is reachable and only five years of research is needed from now before starting with production facilities, as stated in Section 2.2.

Concluding the sensitivity analysis: the eGyro is a very feasible concept and would definitely make it to the market if further research will be done and a production facility is established.

14 Conclusion

In case of a medical emergency, it is desirable to have a fast medical emergency response system. To accommodate for this desire, an EMS system is currently in use. Nowadays several vehicles are used for medical support in the Netherlands, such as cars and emergency helicopters for MMT. However, there is need for a new vehicle, which will improve the services provided by the current vehicles. This design process results in a VTOL vehicle, with an improved landing area and a lower environmental impact.

For this design a vehicle for three crew members and an optional patient is required. The vehicle should be able to fly for two hours at a minimum velocity of 150 $\left[\frac{\text{km}}{\text{h}}\right]$.

The compound eGyro design, with a MTOW of 1850 [kg], is equipped with 4 ducted fans using electric motors, powered by batteries to lower noise and pollution levels during the initial phase of flight. The 4 ducted fans reduce the landing area to a size of 12×12 [m]. This is a 77 % decrease of landing area with respect to current EMS vehicles. The hybrid electric propulsion system is chosen to decrease the environmental impact.

During cruise the vehicle operates like an auto-gyro with a 4 bladed teetering rotor of 8.48 [m] diameter. The cruise speed is 200 $\left[\frac{\text{km}}{\text{h}}\right]$. The aft ducted fans are tilted 90 [deg] to produce the cruise thrust. The front two ducted fans are turned off while cruising. Power during cruise is provided by a hybrid electric powertrain, using a turboshaft engine in combination with a generator. The total configuration results in a noise decrease of 60 % compared to current EMS vehicles and complies with the given key requirements. The final endurance is calculated to be 2 hours and 15 minutes.

The next step of the design would be an extensive and even more detailed analysis of all subsystems of the eGyro. This would include extensive wind tunnel tests, finite element structural analyses and CFD computations on the vehicle. Also a more detailed control and stability analysis should be done, as currently only the cruise flight is analyzed. In conclusion, the vehicle requires a flight control system to be able to fly. The eGyro is aimed to be fully operational in 2024.

References

[1] Eurocopter, "Eurocopter EC135 technical data." http://www.eurocopter.com/site/docs_wsw/RUB_498/135-09-101-01-E.pdf, 2009.

[2] B. Appeldoorn, A. de Bode, J. Delsen, Y. Haartsen, S. Idoum, B. Meijer, T. Sanders, B. Singh, A. Vanweksenaere, and B. Wilken, "AE3200 Design Synthesis 2012-2013 Final Report," tech. rep., TU Delft, faculty of Aerospace Engineering, June 2013.

[3] R. Bergers, F. Dewitte, V. Harinarain, D. Höppener, B. van Kortenhof, R. Moerland, K. Mooi, T. van Ostaijen, C. Ullrich, and A. Urlings, "AE3200 Design Synthesis 2012-2013 Baseline Report," tech. rep., TU Delft, faculty of Aerospace Engineering, Apr. 2013.

[4] R. Bergers, F. Dewitte, V. Harinarain, D. Höppener, B. van Kortenhof, R. Moerland, K. Mooi, T. van Ostaijen, C. Ullrich, and A. Urlings, "AE3200 Design Synthesis 2012-2013 Mid-Term Report," tech. rep., TU Delft, faculty of Aerospace Engineering, Apr. 2013.

[5] H. Giesbers and G. Kommer, "Winding up the windmill." http://www.zorgatlas.nl/zorg/ziekenhuiszorg/traumazorg/bereikbaarheid-24-7-mmt-zorg-vier-helikopters-2011/, June 2012.

[6] European Aviation Safety Agency, *Certification Specifications for Small Rotorcraft CS-27*. â, Nov. 2008.

[7] Envia Systems, "Envia systems." http://www.http://enviasystems.com/, June 2013.

[8] R.A. Hawsey et al, "High power density generator concepts for aerospace electric power," tech. rep., Oak Ridge National Laboratory, Applied Technology Division, 1989.

[9] PAL-V Europe NV, "PAL-V One." http://pal-v.com/, 2013.

[10] Damen Shipyards, "Damen Shipyards." http://www.damen.com, June 2013.

[11] Dutch Red Cross, "Dutch red cross." http://www.rodekruis.nl, June 2013.

[12] G. Wright Jr., *Ducted fan design, Vol. 1*. Mass Flow, 2001.

[13] MathWorks, "MATLAB," 2013.

[14] M. Pavel, "Guidelines for a first dimensioning of helicopter rotor." 2009.

[15] EASA, "EASA TYPE-CERTIFICATE DATA SHEET Turbomeca Arriel 2 series engines." http://www.easa.europa.eu/certification/type-certificates/docs/engines/EASA-TCDS-E.001_Turbomeca_ARRIEL_2_Series_engines-07-17122012.pdf, Dec. 2012.

[16] Panasonic, "Panasonic NCR18650 Batteries." http://industrial.panasonic.com/www-cgi/jvcr13pz.cgi?E+BA+3+ACA4001+NCR18650+7+WW, June 2013.

[17] Nuon Solar Team, "Nuon Solar Team." http:///www.nuonsolarteam.nl/, June 2013.

[18] Index Mundi, "Jet fuel daily price." http://www.indexmundi.com/commodities/?commodity=jet-fuel&months=360. visited on June 7, 2013.

[19] Mike Ricci, "Uav electric propulsion." http://www.launchpnt.com/portfolio/aerospace/uav-electric-propulsion/, Apr. 2011.

[20] R. Prouty, *Helicopter Performance, Stability, and Control*. Robert E. Krieger Publishing Company, 1990.

[21] M. Pavel, "Guidelines for a first dimensioning of helicopter rotor," tech. rep., TU Delft, 2009.

[22] Federal Aviation Administration, "Code of federal regulations." http://rgl.faa.gov/Regulatory_and_Guidance_Library%5CrgFAR.nsf/0/AEAD1A7505EF922F852565F6006C1678?OpenDocument, 1990.

[23] H. Joore, "Autogyro design rules," tech. rep., TU Delft, 2012.

[24] L.S. Stivers Jr. and Fred J. Rice Jr., "Aerodynamic characteristics of four NACA airfoil sections designed for helicopter rotor blades," tech. rep., NACA, July 1946.

[25] Airfoil Tools, "NACA 8-H-12 AIRFOIL (n8h12-il)." http://airfoiltools.com/airfoil/details?airfoil=n8h12-il, 2013.

[26] A. Brindejonc, "Design and testing of an autorotative payload delivery system: the autobody," Master's thesis, University of Maryland, 2005.

[27] B. van Schie, "Autorotation of modern helicopters," tech. rep., TU Delft, 2007.

[28] J. Seddon and S. Newman, *Basic Helicopter Aerodynamics*. Wiley, 3rd ed., 2001.

[29] T. van Holten and J. Melkert, "Helicopter performance, stability and control," tech. rep., TU Delft, 2002.

[30] M. Pavel, "Forward flight," tech. rep., TU Delft, 2012.

[31] J. Leishman, *Principles of helicopter Aerodynamics*. Cambridge University Press, 2002.

[32] H. Joore, "Autogyro design rules," tech. rep., Delft University of Technology, June 2012.

[33] J. Mulder, W. van Staveren, J. van der Vaart, E. de Weerdt, A. in 't Veld, and E. Mooij, "AE3202 flight dynamics lecture notes." Internal publication TU Delft, 2013.

[34] G. Padfield, *Helicopter Flight Dynamics*. Blackwell Publishing, 2007.

[35] A. Deperrois, "XFLR 5." IT software, Mar. 2013.

[36] J. Roskam, *Airplane Design Part II: Preliminary Configuration Design and Integration of the Propulsion System*. DARcorporation, 1997.

[37] M. Pavel, "Stability of rotorcraft, lecture ae 4313." 2012.

[38] B. M. M. P. Th. van Holten, J.A. Melkert, "AE4213 helicopter performance, stability and control lecture notes." Internal publication TU Delft, 2002.

[39] F.B. Gustafson and Almer D. Crim, "Flight measurements and analysis of helicopter normal load factors in maneuvers," tech. rep., NACA, Jan. 1953.

[40] J. Wheatley, "Wing pressure distribution and rotor-blade motion of an autogiro as determined in flight," tech. rep., NACA, 1933.

[41] J. Marte and D. Kurtz, "A review of aerodynamic noise from propellers, rotor, and lift fans," tech. rep., NASA, Jan. 1970.

[42] G. S. Hreinsson, "Aircraft noise," tech. rep., Department of Aerospace and Ocean Engineering Virginia Polytechnic Institute and State University, Dec. 1993.

[43] E. Boeker, E. Dinges, B. He, G. Fleming, C. Roof, P. Gerbi, A. Rapoza, and J. Hemann, "Integrated noise model (inm) version 7.0 technical manual," tech. rep., FAA Office of Environment and Energy, Jan. 2008.

[44] EASA, "Type-certificate data sheet for noise," tech. rep., EASA, Dec. 2011.

[45] T. Rindlisbacher, "Guidance on the determination of helicopter emissions," tech. rep., Federal Department of the Environment, Transport, Energy and Communications, Mar. 2009.

[46] T. Megson, *Aircraft Structures for Engineering Students*. Elsevier Ltd., 2007.

[47] Toray Carbon Fibers America Inc., "Toray CA T700S data sheet." http://www.toraycfa.com/pdfs/T700SDataSheet.pdf.

[48] "AA7072." http://www.efunda.com/glossary/materials/alloys/materials--alloys--aluminum_alloy--wrought--aa_7072.cfm.

[49] Performance Composites Ltd., "Mechanical properties of carbon fibre composite materials, fibre / epoxy resin (120 degrees celcius cure)." http://www.performance-composites.com/carbonfibre/mechanicalproperties_2.asp.

[50] Composite Material Blog, "Boron fiber - superior to carbon." http://www.compositesblog.com/2009/10/boron-fiber-better-carbon.html, Oct. 2009.

[51] http://pds25.egloos.com/pds/201212/26/60/f0205060_50dafb677b0a6.jpg.

[52] Rotortec.com, "Cloud Dancer II - eine neue Generation." http://www.rotortec.com/cloud%20dancer%202.htm.

[53] http://farm9.staticflickr.com/8533/8695644812_2cc4944ff0_b.jpg.

[54] P. Cunat, "Stainless steel properties for automotive applications." http://www.euro-inox.org/pdf/auto/StructuralAutomotiveApp_EN.pdf, 2000.

[55] Sportsmoto, "Helicopter skid configuration." http://www.sportsmoto.co.uk/acatalog/HDX500-95-meyal-skids.jpg, June 2013.

[56] Hobbyking, "Helicopter floats configuration." http://www.hobbyking.com/hobbyking/store/catalog/23480P1.jpg, June 2013.

[57] Chinook Helicopters, "Chinook landing gear." http://www.chinook-helicopter.com/standards/images/forgear1.jpg, June 2013.

[58] Engineering Toolbox, "Rolling resistance and friction." http://www.engineeringtoolbox.com/rolling-friction-resistance-d_1303.html, June 2013.

[59] EcoModder, "Vehicle coefficient of drag list." http://ecomodder.com/wiki/index.php/Vehicle_Coefficient_of_Drag_List, June 2013.

[60] M. Beltramo, "Parametric study of helicopter aircraft systems costs and weights," tech. rep., NASA NTIS: 8017, Jan. 1980.